
Masters Theses

Student Theses and Dissertations

Fall 2014

Influence of erosional unloading on the state of stress for low amplitude single-layer buckle folds - implications for tensile fracture occurrence

Mengke Li

Follow this and additional works at: https://scholarsmine.mst.edu/masters_theses



Part of the [Petroleum Engineering Commons](#)

Department:

Recommended Citation

Li, Mengke, "Influence of erosional unloading on the state of stress for low amplitude single-layer buckle folds - implications for tensile fracture occurrence" (2014). *Masters Theses*. 7332.

https://scholarsmine.mst.edu/masters_theses/7332

This thesis is brought to you by Scholars' Mine, a service of the Missouri S&T Library and Learning Resources. This work is protected by U. S. Copyright Law. Unauthorized use including reproduction for redistribution requires the permission of the copyright holder. For more information, please contact scholarsmine@mst.edu.

INFLUENCE OF EROSIONAL UNLOADING ON THE STATE OF STRESS FOR
LOW AMPLITUDE SINGLE-LAYER BUCKLE FOLDS - IMPLICATIONS FOR
TENSILE FRACTURE OCCURENCE

by

MENGKE LI

A THESIS

Presented to the Graduate Faculty of the
MISSOURI UNIVERSITY OF SCIENCE AND TECHNOLOGY

In Partial Fulfillment of the Requirements for the Degree

MASTER OF SCIENCE IN PETROLEUM ENGINEERING

2014

Approved by

Dr. Andreas Eckert, Advisor
Dr. Alan Chapman
Dr. John Hogan

© 2014

MENGKE LI

All Rights Reserved

ABSTRACT

The existence of fractures associated to buckle folds is related to the strain distribution of the fold. The erosional unloading process can amplify the remnant strain in the folded layer. Two-dimensional plane strain Finite Element Analysis (FEA) is used to investigate the influence of the erosional unloading step on both the evolution of the state of stress and the associated failure patterns in low amplitude buckle folds. Sensitivity analyses on different input parameters, including viscosity, shortening ratio, and overburden pressure, are performed. Based on the simulation results, tensile stress can be initiated both in the crest and in the limb of low amplitude buckle folds in high permeability models during the elastic erosional unloading process. Tensile failure can be initiated perpendicular to the bedding in the top of the fold crest. The type of fracture in the limb depends on the strength of the rock. Tensile failure is initiated in the fold limb more likely for strong rocks while shear failure is initiated more likely for weak rocks. The orientation of both the stresses and the subsequent fractures in low amplitude folds is not affected by the erosional unloading process. In summary, the initiation of both the tensile stress and the subsequent fractures depends on rock properties and strain history.

ACKNOWLEDGMENTS

I would like to express my deepest gratitude to my advisor Dr. Andreas Eckert for the great deal of patience and instruction he had for me during the past two years. His academic guidance and editorial corrections have been crucial to the completion of this thesis. He always treated me with an open mind and he is not only an academic mentor but also a friend in life.

I am grateful to the valuable suggestions and feedback from the committee members Dr. Hogan and Dr. Chapman. Their help and comments have been important for me to complete this thesis. I would like to thank Xiaolong Liu for his help and suggestion on this thesis. I also want to thank those lovely friends in geomechanics research group, who have always been so helpful and adorable that they made each day of working together an unforgettable memory. I also would like to give my thanks to the writing technical editor, Elizabeth M. Roberson, and the format check editor, Amy L. McMillen.

Finally, my great appreciation goes to my parents, who always love me, believe me, and give me whatever they have under no conditions. Without their support, I would not be able to achieve what I have accomplished so far. I will always appreciate their unconditional love and support.

TABLE OF CONTENTS

	Page
ABSTRACT.....	iii
ACKNOWLEDGMENTS	iv
LIST OF ILLUSTRATIONS.....	viii
LIST OF TABLES.....	xi
NOMENCLATURE	xii
SECTION	
1. INTRODUCTION.....	1
1.1. OVERVIEW.....	1
1.2. LITERATURE REVIEW	1
1.2.1. Buckle Folds Theory.....	2
1.2.2. Rheology.....	4
1.2.3. Fractures Related to Folds.....	6
1.2.3.1 General considerations.....	6
1.2.3.2 Extension fractures.....	8
1.2.4. Influence of Erosion/ Exhumation on Stress and Fractures.....	9
1.3. RESEARCH OBJECTIVES.....	10
2. BASIC THEORY.....	12
2.1. ROCK MECHANICS.....	12
2.1.1. Traction Vector and Stress Tensor.....	12
2.1.2. Principal Stress.....	14
2.1.3. Rock Failure.....	14
2.1.3.1 Tensile failure.....	15
2.1.3.2 Shear failure.....	16
2.1.3.3 Coulomb criterion for shear failures.....	17
2.1.3.4 Coulomb Griffith-Coulomb failure criterion.....	19
2.2. FOLDING THEORY.....	20
2.2.1. Distribution of Stresses in Buckle Folds.....	20
3. MODELING METHOD.....	23

3.1. FINITE ELEMENT METHOD IN ABAQUS™	23
3.1.1. Finite Element Analysis.	23
3.1.2. Equations System to be Solved by ABAQUS.....	24
3.1.3. Using ABAQUS™ to Model Folding.....	26
3.2. MATERIAL PROPERTIES	26
3.3. MODEL GEOMETRY AND BOUNDARY CONDITIONS	29
3.4. SIMULATION PROCESS	30
3.4.1. Pre-stressing.	30
3.4.2. Buckling.	31
3.4.3. Erosional Unloading.....	31
4. RESULTS.....	33
4.1. INTRODUCTION	33
4.1.1. Evolution of Stress during Buckling.	34
4.2. RHEOLOGY INFLUENCE ON EROSION	36
4.2.1. Minimum Effective Stress Evolution.	36
4.2.2. Principal Stress Evolution for Visco-elastic Erosion Rheology.....	39
4.3. INFLUENCE OF EROSION RATE	42
4.4. INFLUENCE OF SHORTENING ON THE STATE OF STRESS DURING ELASTIC EROSION	44
4.4.1. Influence on the Stress Reduction Rate.....	44
4.4.2. Influence on the Orientation of the Tensile Stress in Erosion Process. .	47
4.5. DIFFERENT OVERBURDEN FOR BASIC MODELS.....	49
4.5.1. Influence of Overburden Thickness.	49
4.5.2. Tensile Stress on the Crest during Erosion.	52
4.5.3. Tensile Stress on the Fold Limb during Erosion.....	55
4.6. MINIMUM FOLD AMPLITUDE FOR TENSILE STRESS BEING INITIATED	59
4.6.1. Introduction.	59
4.6.2. Procedure to Obtain the Minimum Amplitude.....	60
4.6.3. Evolution of σ_3' Orientation.....	63
4.6.4. Evolution of Stress Magnitude and Tensile Failure Initiation.	66
5. DISCUSSION	69

5.1. RHEOLOGY	69
5.2. OVERBURDEN INFLUENCE.....	69
5.3. TENSILE FAILURE INITIATION FOR LOW AMPLITUDE FOLDS.....	70
5.4. VISCOSITY CONSIDERATION	79
5.5. LIMITATIONS.....	80
6. SUMMARY	81
6.1. CONCLUSION.....	81
6.2 OUTLOOK	82
APPENDICES	
A. STRESS EVOLUTION AT THE FOLD CREST DURING 30% SHORTENING.....	84
B. STRESS EVOLUTION AT THE FOLD CREST DURING 30% SHORTENING.....	87
BIBLIOGRAPHY.....	90
VITA.....	95

LIST OF ILLUSTRATIONS

Figure	Page
1.1. The normal stress in the thin-plate analysis.....	4
1.2. Rheology combinations created with both existing and proposed solutions	5
1.3. Minor fracture trends.	7
1.4. Stearns' (1968) model of multiple fractures forming symmetrically to the fold axis..	7
2.1. The stress component acting on a cube surface in three dimensions coordinate.....	13
2.2. Mohr diagram shows the tensile failure criterion.	15
2.3. Physical space of simple tensile failure case.	16
2.4. Simple sketch of shear failure.....	17
2.5. Mohr-Coulomb criterion diagram for shear failure..	18
2.6. The conjugate directions of shear failure.....	18
2.7. The combined Griffith-Coulomb failure criterion diagram.	19
2.8. The effect of shortening ratio on the orientation of maximum principal stress.....	20
2.9. The fold limb's stress evolution during buckling.	21
2.10. The fold crest's stress evolution during buckling.....	21
3.1. Sketch of discretization in FE method.	23
3.2. Model sketch and boundary conditions of the numerical models used.	29
3.3. Gravitational pre-stressing model sketch.....	30
3.4. Buckling model sketch.....	31
3.5. Model sketches for erosional unloading process..	32
4.1. Stress evolution on the top of the fold crest with 1000m overburden thickness throughout 30% shortening process.....	34
4.2. Stress evolution on the fold limb with overburden thickness 1000m throughout 30% shortening.	35
4.3. Stress orientation in the fold limb.....	35
4.4. The evolution of σ_3' on fold crest top throughout the entire process, including buckling and viscoelastic erosion..	37
4.5. The evolution of σ_3' on fold crest limb throughout the entire process, including buckling and viscoelastic erosion.	39
4.6. Fold crest effective principal stress evolution throughout 30% shortening and viscoelastic erosion.....	41

4.7. Fold limb effective principal stress evolution throughout 30% shortening and viscoelastic erosion.....	41
4.8. Stress evolutions of crest during erosional unloading process under different erosion rates.....	43
4.9. Stress evolutions of limb during erosional unloading process under different erosion rates.....	44
4.10. Reduction rates of the fold crest's horizontal stress and vertical stress for different amount of shortening models (1000m overburden thickness) during elastic erosion process.	45
4.11. Reduction rates of the fold limb's minimum effective stress and maximum effective stress for different amount of shortening models (1000m overburden thickness) during elastic erosion process.	46
4.12. The orientation of σ_3' at the time when tensile stress is initiated for 1000m overburden models.....	48
4.13. The orientation of σ_3' at the time when tensile stress is initiated for 3000m overburden models.....	49
4.14. Stress development of the fold crest during erosion under different initial overburden thickness.	51
4.15. Stress development of the fold limb during erosional unloading process under different initial overburden thickness.	52
4.16. The evolution of the fold crest's minimum effective stress throughout both 30% buckling and the following erosion process.	53
4.17. Mohr circles of state of stress for tensile stress on the top of the fold crest for each overburden thickness.....	54
4.18. Evolution of σ_3' for larger overburden depth (>1000m) till the tensile stress is initiated during erosion process.	55
4.19. The evolution of the fold limb's minimum effective stress throughout both 30% buckling and the following erosion process.	56
4.20. Mohr circles of state of stress for fractures on the middle of fold limb for each overburden thickness.....	58
4.21. The contour plots for the spatial distribution and orientation of σ_3'	59
4.22. The fold amplitude evolution during buckling process for each overburden thickness.....	60
4.23. The evolution of minimum effective stress on the fold crest for different overburden thickness.	61
4.24. The σ_3' evolution of trial amount of shortening and the target amount of shortening for each overburden thickness model.	62
4.25. The orientation of σ_3' for 500m initial overburden thickness	64

4.26. The orientation of σ_3' for 1000m initial overburden thickness	64
4.27. The orientation of σ_3' for 2000m initial overburden thickness	65
4.28. The orientation of σ_3' for 3000m initial overburden thickness	65
4.29. The minimum amplitude for tensile failure being initiated at the end of erosion process for each overburden thickness in this research.	66
4.30. The final fold amplitude and wavelength for each overburden thickness models...	66
4.31. Evolution of the σ_3' in the fold crest throughout the entire buckling and erosional unloading process.....	67
4.32. The fold limb's stress evolution throughout the whole buckling and erosion process.	68
5.1. The evolution of the fold crest's σ_3' throughout the entire process including both buckling process and the erosional unloading process.	79

LIST OF TABLES

Table	Page
3.1. Basic model's material properties of both the folding layer and the matrix.....	28
3.2 Overburden and shortening combinations for basic models.....	29
4.1 The final overburden thickness at the end of buckling corresponding to each initial overburden thickness after 30% shortening.....	50
4.2. The eroded overburden thickness and ratio for each initial overburden when tensile stress is initiated.....	55
4.3 The eroded overburden thickness and ratio for each initial overburden when tensile failure is initiated	57
4.4. The minimum amount of shortening for tensile stress being initiated	63
5.1. Fractures for Strong rocks.....	73
5.2. Fractures for weak rocks.....	77
6.1. The minimum amount of shortening and minimum fold amplitude.....	82

NOMENCLATURE

Symbol	Description
σ_3	Minimum Principal Stress
σ_1	Maximum Principal Stress
ρ_b	Bulk Density
ρ_d	Dry Density
M_t	Total Mass
V_t	Total Volume
ρ_w	Water Density
ϕ	Porosity
d	Depth
e	Void Ratio
G_s	Specific Gravity
σ	Stress
ε	Strain
E	Young's Modulus
ν	Possion's Ratio
$\dot{\varepsilon}$	Strain Rate
μ	Viscosity
G	Shear Modulus
K	Bulk Modulus
F	Force Vector
T	Traction Vector
P_p	Pore Pressure
σ	Stress Tensor
α	Effective Stress Coefficient
T_0	Tensile Strength
σ_3'	Effective Minimum Principle Stress
σ_n	Normal Stress
τ	Critical Share Stress

S_0	Cohesion
ψ	Angle of Internal Friction
λ_d	Dominant Wavelength
R	Competence Contrast
h	Layer Thickness
μ_L	Layer Viscosity
μ_M	Matrix Viscosity
S_x	Horizontal Stretch
A	Amplitude
P_L	Axial Load
w	Deflection
η	Coefficient of Viscosity
P	Static Pressure
K_e	Element Stiffness Matrix
f_e	Element Loading
q_e	Internal Force

1. INTRODUCTION

1.1. OVERVIEW

Folds are formed when the initial planar bedding deforms into a wave-like curving structure. Folding occurs common, on all scales, during rock deformation. It ranges from 10's to 100s of kms bends in orogenic belts to micro size folds visible only under a microscope (Twiss and Moores, 2006). These folds are, however, periodic, and all illustrate ductile deformation. Single layer folds are generated by a mechanical instability. The results of single layer studies can also be applied to other complex geologically-related mechanical instabilities (e.g. salt diapirism, crustal folding and lithospheric folding).

Understanding how folds form is important because folded sedimentary strata represent common structural traps for hydrocarbon accumulation. Folds can act both as reservoir rocks and cap rocks. A most famous example of anticlinal traps formed by folds is the Zagro fold-and-thrust belt in Iraq and Iran. It holds more than 5% of the world's petroleum reserves (Reif et al., 2011). A number of structural traps are also located across the United States, including the Salt Creek field in the Powder River basin of Wyoming, the Santa Fe Springs field near Los Angeles, and the Wilmington field of Long Beach in California.

Fractures play an important role in potential reservoirs. These fractures affect a reservoir's permeability and fluid flow pathway. New fractures, as well as the reopening of pre-existing fractures, are often initiated at any stage of folding. Therefore, both folding deformation kinematics and related fracture developments have been studied in great detail. Many of such studies focus on the prediction of distribution, type, and orientation of the fractures, particularly.

1.2. LITERATURE REVIEW

Hall's (1815) first mention of the word "folds" in his study leads to several early studies related to fold mechanics, terminology, and geometry. From the second half of the 20th century, the rheology, strain, and deformation history of buckle folds have been studied extensively by scientists (e.g., Biot, 1961; Ramberg, 1960). Field observations,

mathematical analyses, and finite element analyses are each commonly used to better understand the folding process.

1.2.1. Buckle Folds Theory. The dominant wavelength theory for single and multi-layer buckle folds first presented by Biot (1961) and Ramberg (1961, 1963) on viscous materials is one of the most remarkable outcomes. Single-layer buckle folds form when an isolated, stiff layer embedded in a less stiff matrix is subjected to layer-parallel shortening. Biot's (1961) theory predicts that, if the stiff layer is given small sinusoidal perturbations with different wavelengths, one such perturbation will grow faster than the others. The wavelength of this perturbation is known as the dominant wavelength. The dominant wavelength (λ_d) is calculated as:

$$\frac{\lambda_d}{h} = 2\pi \left(\frac{\mu_f}{6\mu_m} \right)^{1/3} \quad (1)$$

where h is the layer thickness, μ_m is the matrix viscosity, and μ_f is the viscosity of the folded layer.

In Biot's (1961) equation, the dominant wavelength is only related to the layer thickness and the competence contrast between the layer and the matrix. The competence contrast is a measurement of material strength defined by elastic modulus ratio of the layer and matrix. Sherwin and Chapple (1968) modify the dominant wavelength. They also consider uniform shortening and thickening of the folded layer. This wavelength also known as preferred wavelength (λ_p) is calculated as:

$$\frac{\lambda_p}{h(T)} = 2\pi \left(\frac{\mu_f}{6\mu_m} \frac{T+1}{2T^2} \right)^{1/3} \quad (2)$$

where $T=S_1/S_2$, S_1 is the principal tension perpendicular to the folded layer, and S_2 is the principal compression parallel to the folded layer.

This modification is important, particularly when the viscosity contrast between the layer and the matrix is small (less than 10:1). Biot (1965) notes that, because infinitesimal deformation is assumed, this theory can only be applied to the early stage of

the folding process. Chapple (1968) suggests that the theory is valid as long as the limb dip is below 20° .

Cobbold (1975) also proposes that initial perturbations play an important role in the evolution of folding. He suggests that the final wavelength and fold shapes are determined by the initial perturbation if the amplitude of initial perturbations is finite. His paraffin wax experiments (Cobbold, 1975) and finite element modelling (Cobbold, 1977) validate this suggestion. Both Williams et al. (1978) and Abbassi and Mancktelow (1990, 1992) later verify that the initial perturbation gradually amplifies into the final fold wavelength. Mühlhaus (1993) confirms this finding. Zhang et al. (1996) used a finite-difference code (FLAC) to point out the importance of the initial perturbation geometry on the geometry of a finite-amplitude fold. Mancktelow (1999) finds that, if an initial wavelength is either much smaller or much larger than the dominant wavelength, the introduced waveform for periodic perturbations grows into folds.

The early analyses completed by both Biot (1959, 1961) and Ramberg (1959, 1960, 1961) are based on thin-plate analysis. This analysis assumes that the state of stress in the buckled layer is only applicable to folds with a wavelength that is much longer than the layer's thickness. It ignores the layer-parallel shear stress and takes into account only the folded layer's normal stress. In thin-plate analysis, the normal stress in the layer can be calculated as the sum of a uniform stress and fiber stress (Fig. 1.1). However, Fletcher (1977) develops the thick plate analysis without the restrictive assumption about stress. It presents more accurate predictions for the growth of low viscosity contrast and low amplitude folds.

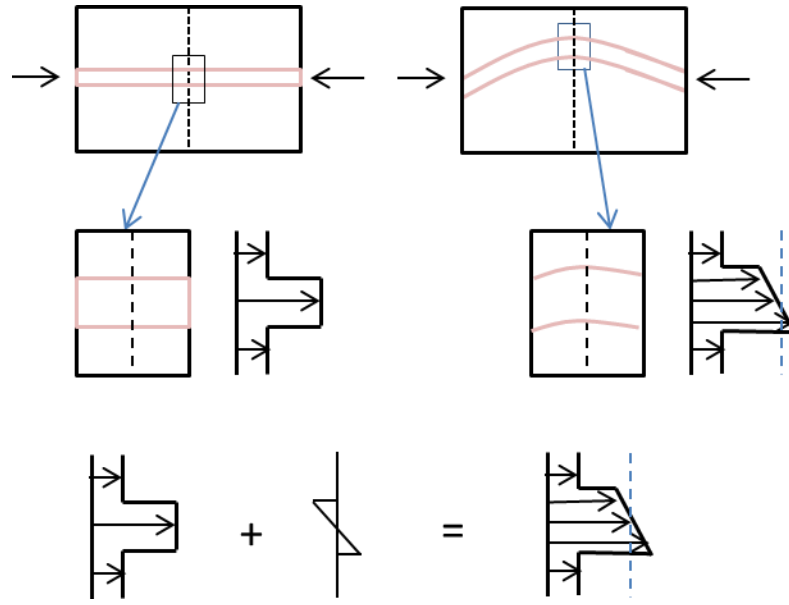


Fig. 1.1. The normal stress in the thin-plate analysis (Schmalholz & Podladchikov, 2000).

1.2.2. Rheology. The temperature and pressure present during the folding process control the rheological behaviors of the folding layer and the matrix. Elastic, visco-elastic, and viscous behaviors are the most common rheologies studied during buckle folding. Both the matrix and the folding layer are likely to exhibit a viscous behavior at a great depth when the temperature and pressure are high. In contrast, the strata present a more elastic behavior when the depth, pressure, and temperature decrease. The folding layer may exhibit a more elastic behavior than the matrix at a certain depth. Comparatively, the matrix layer may exhibit a more viscous behavior than the folding layer (Jeng and Huang, 2008). The possible rheology combinations that can occur between the folding layer and the matrix are illustrated in Fig. 1.2.

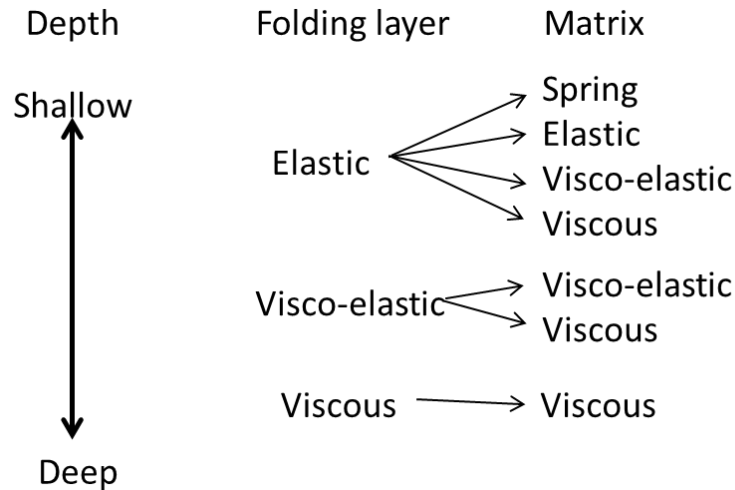


Fig. 1.2. Rheology combinations created with both existing and proposed solutions (Jeng and Huang, 2008).

A rock's rheological behavior plays an important role in the selection of an appropriate dominant wavelength. Biot (1961) and Ramberg (1961) presents a thin-plate dominant wavelength equation for a Newtonian viscous layer and matrix (Equation 1). It suggests that the dominant wavelength for this rheology is determined only by the layer thickness and the viscosity ratio of the folding layer and the matrix. The folding process may be controlled by a rock's elastic behavior under certain conditions. Currie et al. (1962) present the dominant wavelength expression for an elastic layer embedded in an elastic matrix. It depends only on elasticity ratio and the layer's thickness. Elastic rheology cannot, however, express the dominant wavelength appropriately if the rocks represent permanent deformation. Both Biot (1961) and Turcotte and Schubert (1982) present the dominant wavelength for an elastic layer embedded in a viscous matrix. It is independent of the matrix viscosity but depends on the elasticity of the folding layer and the applied load. It is calculated as:

$$\frac{\lambda_d}{h} = \pi \left(\frac{E_f}{P(1-\nu_f^2)} \right)^{1/2} \quad (3)$$

where E_f is the folded layer's elasticity, P is the layer-parallel stress in the competent layer, and ν_f is the folded layer's Poisson's ratio.

Shmalholz and Podladchikov (1999) introduce the parameter R for visco-elastic folding. If $R > 1$, folding is dominated by elastic deformation; if $R < 1$, folding is dominated by viscous deformation.

$$R = \frac{\lambda_{dv}}{\lambda_{de}} \quad (4)$$

where λ_{dv} is the dominant wavelength given by equation (1), and λ_{de} is the dominant wavelength given by equation (3).

1.2.3. Fractures Related to Folds. Fractures associated with folds are crucial to geological science research and to the petroleum industry. Fractures affect the permeability and fluid flow pathways of reservoirs. New fractures and reopening of pre-existing fractures can be initiated at any stage of folding. Geologists investigate fractures on folds in an attempt to identify a physical interpretation, e.g., fracture generation. They also focus on developing valid methods to predict the location, spatial density, and orientations of fractures underground.

1.2.3.1 General considerations. Early studies (Cloos, 1948; Price, 1966; Stearns, 1968) propose a variety of methods to describe the fractures in folds based on the relationship between fracture orientations and the state of stress. They are known as symmetric relationships between the stress field and the folded layer. Griggs and Handin (1960) suggest that extension fractures are generated perpendicular to the minimum principle stress (σ_3). Shear fractures form both parallel to σ_2 and oblique to maximum principle stress (σ_1). Price (1966) confirms this (Fig. 1.3). Moreover, if pressures are restricted enough, conjugate sets of shear fractures may occur whereas, in most cases, fractures develop in only one direction, at a modest confining pressure. Stearns (1968) improves Griggs and Handin's (1960) conclusions, suggesting that 11 fracture orientations are present in 4 fracture sets. Stearns (1968) also indicates that the fracture patterns both below and above the neutral surface are affected by the exchange of principal stress orientations (Fig. 1.4). In this model, all 11 fracture orientations can grow within the same bed. It contradicts, however, lab observations made by Griggs and

Handin (1966), Jaeger and Cook (1979) and Twiss and Moores (1992) where, common, only one fracture orientation is present within one sample.

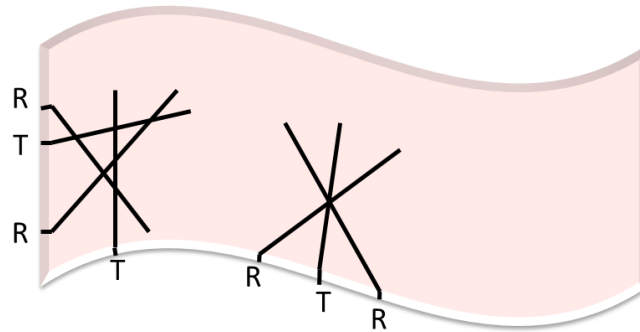


Fig. 1.3. Minor fracture trends (Price, 1966). Here, T is the extension fracture, and R is the shear fracture.

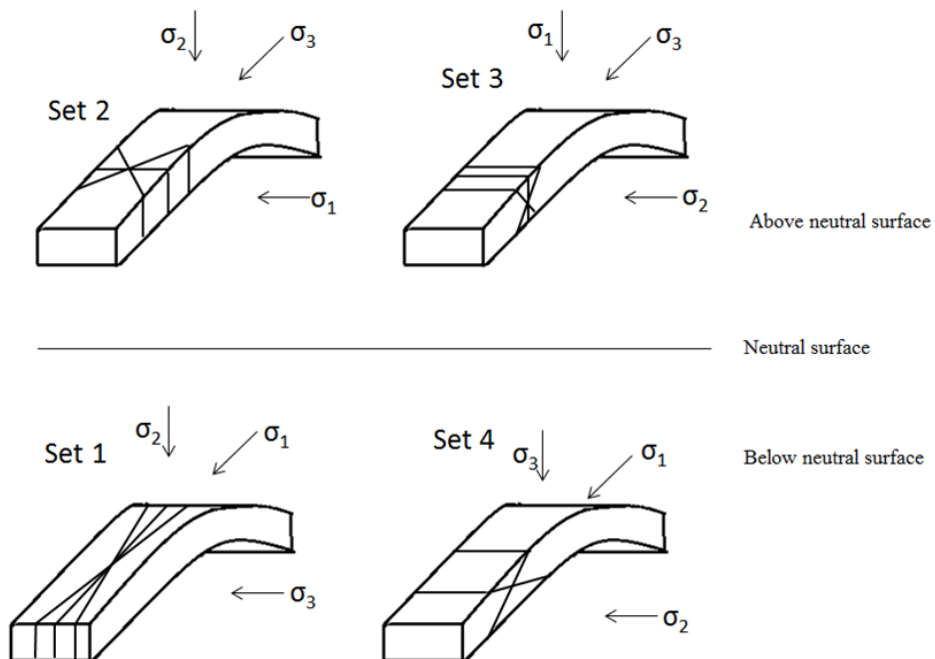


Fig. 1.4. Stearns' (1968) model of multiple fractures forming symmetrically to the fold axis. State of stress and neutral surface are considered.

Several studies, however, have questioned the validity of such symmetric relationships. These studies analyze the specific evidence for fractures, the spatial distribution of fractures, and the formation sequence to study fracture patterns associated with folds. Hancock (1985) establishes a classification based on both sedimentary layering and the geometry of fold hinges. Reches (1976) notes that several joint sets that formed either pre-folding or at the onset of the folding process do not satisfy symmetric relationships. Similarly, Dunne (1986) indicates that fracture sets reactivating during the anticline formation in West Virginia do not follow the symmetric fracture-fold relationship. Price and Cosgrove (1990) suggest that, if the fracture patterns do not obey symmetric relationships, the fractures may not form during the folding process. It is either because that there are no fractures before folding or because that the fracturing process during folding is not affected by former fractures.

As an alternative, fold curvature analysis can be used to analyze fractures associated with folds. Curvature is the orientation change in a unit's surface distance (Twiss & Moores, 2007). It can be calculated as the reciprocal of the curvature radius for cylindrical fold geometry (Lisle, 1994). Stearns and Friedman (1972) study the orientation and distribution of fractures in non-cylindrical folds. Ericsson et al. (1988) investigates the relationship between fracture density and fold curvature. Fischer and Wilkerson (2000) use simple curvature analysis models to illustrate the fracture evolution in an evolving fold's surface. They suggest that curvature techniques cannot sufficiently illustrate fracture characteristics.

1.2.3.2 Extension fractures. Most extension fractures are either vertical or dip steeply, commonly occurring normal to the bedding and cutting the fold axis at 90° (Price & Cosgrove, 1990). Layer-parallel tensile stress at the fold crest commonly generates tensile failure (Ramsay, 1967). Syntectonic extension fractures are commonly filled by sparry calcite. Filled extension fractures on the outer arc commonly occur perpendicular to bedding while fractures subparallel to the bedding begin as extension fractures on the limbs of the same fold. These tensile fractures on the fold limb are later developed into shear fractures such as thrust faults (Groshong, 1975). Groshong (1975) also suggests that the extension fractures slowly grow longer and wider during the folding process; they do not form rapidly at one time. Lemiszki et al. (1994) suggest that

the initiation of hinge-parallel tensile failure on buckle folds depends on the fold's depth, fluid pressure, and strain rate. Reber et al. (2010) present a numerical simulation to illustrate that the orientation of σ_3 is parallel to the fold axis at a low fold amplitude; it rotates to be perpendicular to the fold axis at a high fold amplitude. The fracture's direction of fractures is determined by the orientation of σ_3 (Reber et al., 2010). Reif et al. (2011) present that joints and tensile fractures are often identified in the upper folded formation while compressional structures occur within the inner part of the anticlines. Reif et al. (2011) also indicate that extension fractures are generated by layer parallel stretching that occurs within the formation's upper layers. A number of researchers (Hubbert & Rubey, 1959; Watts, 1987) also consider the influence of pore pressure on tensile failure. This influence is exhibited in terms of effective stress (the difference between total stress and pore pressure). Extension fractures are generated when the minimum effective stress either reaches or exceeds the rock's tensile strength (Watts, 1987). Lemiszki et al. (1994) suggest that higher pore pressure is required to generate tensile failure as the depth increases.

1.2.4. Influence of Erosion/ Exhumation on Stress and Fractures. The erosion process will remove materials from the Earth's surface, and thus the vertical compressive stress is reduced. The rock strength is reduced when the rock is fractured by the change of state of stress. This change then increases the erosion rate (Molnar, 2005).

Turcotte and Schubert (2002) introduce an elastic erosional unloading model under uni-axial strain conditions: i.e., the geological structure is confined laterally; and only allows for a vertical component of strain. If the initial state of stress before the erosional unloading process is lithostatic, the horizontal stress during erosion can be expressed as

$$\sigma_h = \sigma_v - \Delta\sigma_v = \rho gh - \frac{v}{1-v} \rho gh = \frac{1-2v}{1-v} \rho gh \quad (5)$$

Liu (2013) applies an erosional unloading step in his finite element analysis of buckle folding. He confirmed that such a process will affect the state of stress and lead to tensile failure in the folded layer. A folding layer's effective minimum stress is decreased by erosion to tensile magnitudes in high permeability models. Tensile stress will be

initiated at the top of the fold crest when it is eroded to some certain depth. That stress, however, are compressive before the erosion process due to buckling. Tensile failure is generated on the fold limb prior to the initiation of tensile failure on the fold crest. The overpressure drops much faster than the total horizontal stress at the beginning of erosional unloading process in low permeability models. The effective minimum stress increases and maintains compression. The overpressure decreases to an equivalent hydrostatic decrease, and the minimum effective stress begins to decrease.

1.3. RESEARCH OBJECTIVES

Liu (2013) finds that tensile fractures at the top of the fold crest that are associated to single-layer buckle folds form under the specific conditions of low overburden, and/or high layer viscosity, and/or low permeability. Moreover, tensile fractures that are initiated in the limb of buckle folds can be explained by the erosional unloading of high permeability rocks. Liu (2012) concludes that the erosional unloading procedure amplifies the remnant strain in the fold layer. However, he only takes into account high amplitude folds (50% shortening) which are only applicable to rare natural cases. Folds with 30% of shortening or less (and associated lower amplitude) are much more common. Thus, low amplitude folds are investigated in this study. Furthermore, the importance of the erosional load step on the widespread development of tensile stresses throughout the fold limb poses the following questions, considering the initiation of tensile failure in buckle folds:

- Does the erosional unloading of buckle folds at different deformation stages result in a similar tensile stress evolution and, hence, similar fracture orientations?
- Does the erosional unloading process result in tensile stresses for low amplitude buckle folds?
- At which deformation stage does tensile failure occur the earliest?
- Is tensile failure the dominant type of failure during erosional unloading or/and is shear failure also promoted?

Two-dimensional plane strain Finite Element Analysis (FEA) is used to investigate the influence of the erosional unloading step on both the evolution of the state

of stress in buckle folds and the associated failure types. A classic Maxwell visco-elastic rheology for both the folding layer and the matrix, including pore pressure, will be applied to include the influence of pore pressure during buckling. The study procedures and objectives are listed as followed:

(1) Setup 2D finite element models based on the dominant wavelength theory to simulate low amplitude single-layer buckle folding under realistic in situ stress and pore pressure.

(2) Apply erosional unloading after different deformation stages of low amplitude folding to predict both where and when tensile failure will occur first.

(3) Perform sensitivity analyses on different input parameters, such as viscosity, shortening ratio, and overburden pressure, to analyze their effects on the state of stress during the folding process and the erosional unloading process.

2. BASIC THEORY

2.1. ROCK MECHANICS

2.1.1. Traction Vector and Stress Tensor. The plane outward unit normal vector defines the orientation of a plane. Likewise the internal force exerted by the rock acting on a plane is expressed by a traction vector (T). The resultant force can be represented by force vector F . The traction vector (T) is defined as the internal force vector divided by the surface area (A):

$$T = \frac{F}{A} \quad (6)$$

The force varies from point-to-point within a rock body. Thus, the area should be shrunk down to a point and indicated as a small area (dA). The traction vector at that point can often be expressed as

$$T = \lim_{dA \rightarrow 0} \frac{dF}{dA} \quad (7)$$

However, in this definition, T is a function of two vectors: the point position vector and the plane unit normal vector. Cauchy (1823) introduces the concept of stress to simplify this problem. He suggests that all traction vectors at a point can be described by a state of stress.

In a cartesian coordinate system a cubic control volume where the normal vectors on the faces of the cube are parallel to the coordinate axes is introduced (Fig. 2.1.). Traction acting on three mutually perpendicular planes of the cube can then be decomposed into one normal traction and two shear tractions, termed stresses (Fig. 2.1). The force equilibrium conditions applied to the cube result in Cauchy's second law:

$$T_i = \sigma_{ij}n_j \quad (8)$$

where T_i is the traction vector acting on the plane, σ_{ij} is the stress tensor (Eq. 9), and n_j is the normal vector of the plane where T_i acts on.

Cauchy's second law relates the tractions on any surface to the stresses on that surface. σ_{ij} is termed the stress tensor which contains nine stress components (three normal stresses and six shear stresses) that can be used to describe the state of stress within this cube.

$$\sigma = \begin{pmatrix} \sigma_{xx} & \sigma_{xy} & \sigma_{xz} \\ \sigma_{yx} & \sigma_{yy} & \sigma_{yz} \\ \sigma_{zx} & \sigma_{zy} & \sigma_{zz} \end{pmatrix} \quad (9)$$

The subscripts of each component can be defined as follows:

- the first subscript is the axis perpendicular to the surface
- the second subscript is the force direction.

For example, σ_{xy} is a shear stress that acts on the surface normal to the x-axis; it occurs in the y-direction.

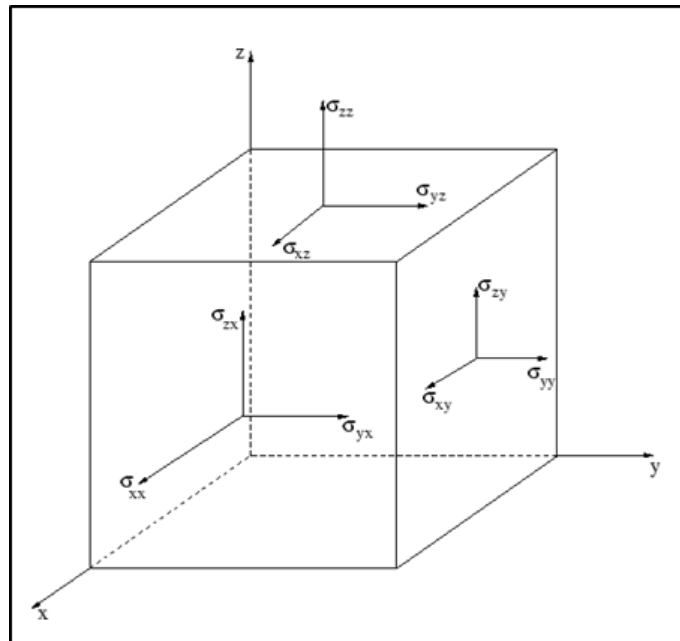


Fig. 2.1. The stress component acting on a cube surface in three dimensions coordinate.

2.1.2. Principal Stress. When the coordinate axes rotates to an orientation where all shear stresses will vanish and the stress state is only defined by normal stresses, these normal stresses which are perpendicular to each other are principal stresses. The stress tensor for a principal state of stress is

$$\sigma = \begin{pmatrix} \sigma_1 & 0 & 0 \\ 0 & \sigma_2 & 0 \\ 0 & 0 & \sigma_3 \end{pmatrix} \quad (10)$$

Studying the effective principal stress is much more important than studying the total stress in a porous and fluid-filled rock system. The total loading (σ) applied to the system will be taken by the fluid and the rock matrix. Thus, the strain, stress, and rock failures are controlled by the load that the rock matrix carries rather than the total load. This part of stress is known as the effective stress (σ') (Terzaghi, 1923). It is refined by Biot as

$$\sigma' = \sigma - \alpha P_p \quad (11)$$

where P_p is the pore pressure. The Biot effective stress coefficient (α) varies between zero to one referring and one; α is defined as

$$\alpha = 1 - \frac{K}{K_s} \quad (12)$$

where K is the rock's bulk modulus, and K_s is the solid grains bulk modulus. In both an unconsolidated rock and a weak rock, $\alpha=1$.

2.1.3. Rock Failure. Fractures and failure associated with buckling folding are somehow complicated since they may exist before folding process, occur during any stages of fold development, or be generated after fold formation. The existence of fractures and the occurrence of rock failure are crucial to the petroleum industry in such as drilling and production. Thus, the ability to accurately predict the conditions of rock failure and fracture occurrences is essential to this industry.

A rock's shape will be changed permanently if the rock is subjected to a large stress it cannot sustain. Under this condition, rock failure will occur. Predicting the occurrence of failure associated with low amplitude buckling folding and erosion process is the main goal of this research. Thus, the criteria used for failure assessment used in this study are introduced.

2.1.3.1 Tensile failure. Each rock type has a characteristic value of tensile strength (T_0) that characterizes the stress magnitude at which tensile failure occurs. Rocks are stable at a tensile stress smaller than T_0 , while tensile failure will occur when rocks are subjected to a tensile stress larger than T_0 . The tensile fracture envelope on a Mohr diagram reveals the boundary that exists between a rock's stable state and its unstable state (Fig. 2.2).

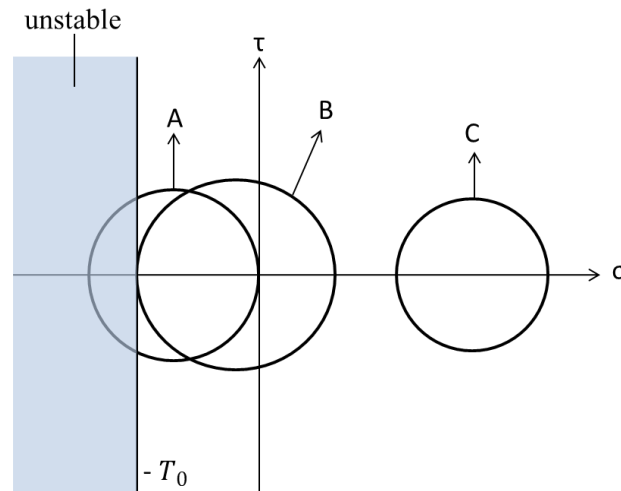


Fig. 2.2. Mohr diagram shows the tensile failure criterion. Circle A cross the tensile strength line so that it presents an unstable state. Circle B just touch that line and presents a critical state. Circle C stays away and on the right of that line so that it is stable state.

Tensile failure will occur in isotropic rocks, when the minimum effective stress reaches the tensile strength:

$$\sigma_3' = -T_0 \quad (13)$$

A tensile fracture's orientation (Fig. 2.3) can be described in one of two ways: a fracture plane angle (α_f), and a fracture angle (θ_f). The fracture plane angle is the angle between the maximum principle stress (σ_1) and the fracture plane. The fracture angle is the angle between σ_1 and the normal vector of the fracture plane. The tensile failure is perpendicular to σ_3 .

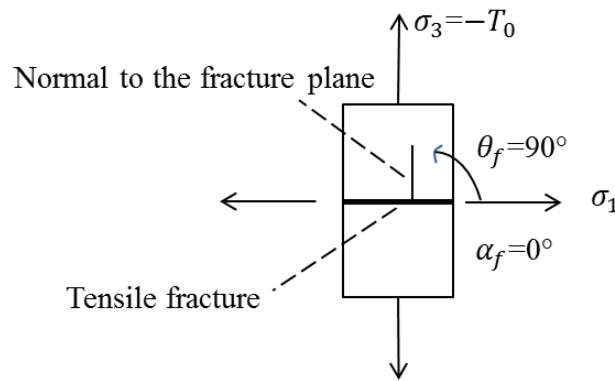


Fig. 2.3. Physical space of simple tensile failure case.

2.1.3.2 Shear failure. Brittle failure along shear fractures occurs when subjected to a moderate amount of confining pressure, and the shear stress exceeds the shear strength of the rock (Fig. 2.4). Fractures will develop on this plane and the rock, above and below the plane will move in two opposite directions. A frictional force is generated by the movement of these two planes and depending on the normal stress. Thus the critical shear stress for shear failure is related to the normal stress on the plane:

$$\tau_{max} = f(\sigma) \quad (14)$$

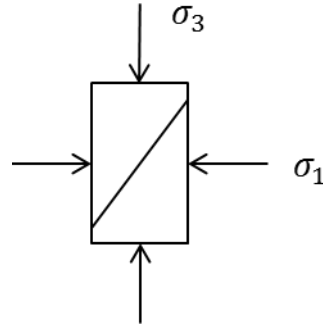


Fig. 2.4. Simple sketch of shear failure.

2.1.3.3 Coulomb criterion for shear failure. Determining the state of stress when shear failure occurs is more complex than determining when uniaxial tensile failure occurs. The Coulomb criterion provides a simple way to investigate the initiation of shear fractures.

Maximum shear stress is a function of normal stress. Coulomb assumes a linear function of normal stress for $f(\sigma)$:

$$|\tau| = f(\sigma) = S_0 + \sigma_n \tan \varphi \quad (15)$$

where S_0 is the internal cohesive strength of the material, φ is the internal friction angle, and σ_n is the normal stress. The sign of τ affects only the movement direction of the plane; it has no effect on fracture initiation. Thus, the absolute value of τ is applied in this criterion.

Eq. 15 defines a straight line in a Mohr circle diagram. The Mohr-Coulomb criterion is introduced in Fig. 2.5. Here, line AF represents the failure line that intercepts the τ -axis at S_0 . The slope is μ . The internal friction angle is φ , and $\mu = \tan \varphi$. Thus, μ is the constant known as the coefficient of internal friction. The information in Fig. 2.5 confirms that shear failure will occur when $\tau \geq S_0 + \mu\sigma$.

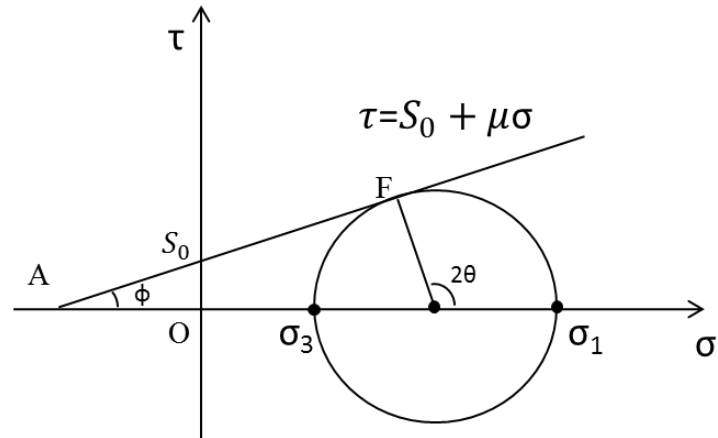


Fig. 2.5. Mohr-Coulomb criterion diagram for shear failure. The state of stress of point F presents the stress state of shear failure of the plane. The angle of failure plane can be estimated using Mohr-Coulomb diagram.

$$180^\circ - \phi - 90^\circ = 180^\circ - 2\theta \quad (16)$$

$$\theta = 45^\circ + \frac{\phi}{2} \quad (0^\circ \leq \phi \leq 90^\circ) \quad (17)$$

Angle θ is the counterclockwise rotation from the maximum principal stress (σ_1) to the plane normal direction (Fig. 2.6). The two planes in Fig. 2.6 are conjugate planes. The range for θ is between 45° and 90° because the possible range for ϕ is between 0° and 90° .

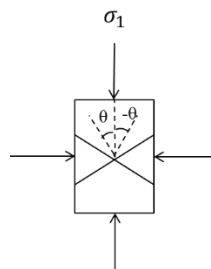


Fig. 2.6. The conjugate directions of shear failure.

2.1.3.4 Coulomb Griffith-Coulomb failure criterion. Coulomb failure

Criterion has some limitations and it does not apply to all failure situations (e.g., when the Mohr circle touches the failure envelope in the tensile region of the failure diagram.). A more reasonable failure criterion, the combined Griffith-Coulomb failure criterion, is introduced. The linear Coulomb criterion (Eq. 15) and the Griffith criterion (Eq. 18) are combined to construct the failure envelop (Fig. 2.7).

$$\tau^2 = 4\sigma T + 4T^2 \quad (18)$$

where τ is the shear stress, σ is the normal stress, and T is the rock's tensile strength.

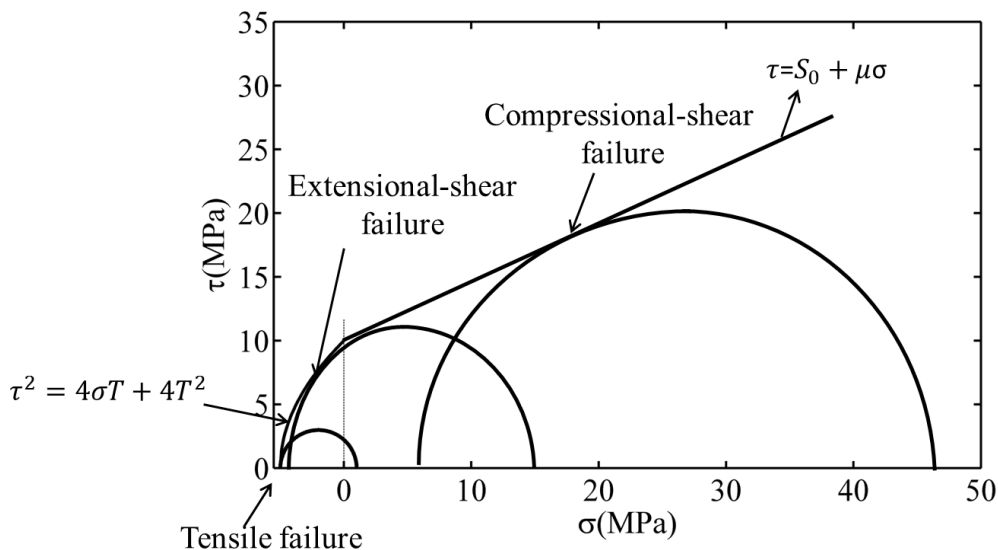


Fig. 2.7. The combined Griffith-Coulomb failure criterion diagram.

In Griffith-Coulomb failure criterion, compressional shear failure ($\sigma > 0$) is described by Coulomb criterion (Eq. 15); Griffith criterion (Eq. 18) accounts for extensional-shear failure ($\sigma < 0$). According to Sibson (2003), tensile failure is initiated

when $(\sigma_1 - \sigma_3) < 4T$; extensional shear failure is initiated when $4T < (\sigma_1 - \sigma_3) < 5.66T$; and compressional shear failure will occur requires $(\sigma_1 - \sigma_3) > 5.66T$.

2.2. FOLDING THEORY

2.2.1. Distribution of Stresses in Buckle Folds. Both the orientation and the magnitude of principal stress in the folding layer are related to rock failure. The state of stress varies in time and space while the folds are developing. The state of stress of a viscous layer embedded in a less viscous matrix during buckling was studied by Dieterich & Carter (1969), using finite element analysis in aspect of different shortening ratio and viscosity contrast, respectively. Liu (2013) also studies the stress history of buckle folds using viscous rheology.

Different buckling stages have different states of stress (Fig. 2.8). The maximum principal stress (σ_1) is parallel to the folding layer and has a uniform, large magnitude along the fold at a low buckling ratio. The layer's maximum principal stress rotates so that it is inclined to the layer with an increased angle as the development processes. The magnitude of σ_1 decreases during this time. The maximum principal stress at the inner part of the fold crest is parallel to the layer's boundaries during the buckling process. The maximum principal stress in the outer part of the fold crest is normal to the layer boundaries. The maximum compressive principal stress in the convex of the fold will initially decrease to zero. Tensile stress will occur during this time.

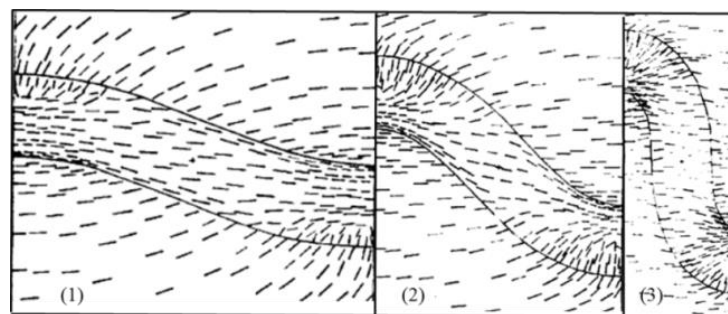


Fig. 2.8. The effect of shortening ratio on the orientation of maximum principal stress. (1) 20% shortening. (2) 40% shortening (3) 100% shortening (after Dieterich & Cater, 1969).

The effective principal stress evolution in the fold limb and at the fold crest during buckling is investigated by Liu (2013). The effective principal stresses in the fold limbs are independent of the element location (Fig. 2.9). The minimum effective stress (σ_3') in the fold limbs increases during the entire buckling process (Fig. 2.9B). The maximum effective stress (σ_1') in the fold limbs increases until 18% shortening and then decreases. After 40% shortening, σ_1' increases again (Fig. 2.9C). The effective principal stresses development at the fold crest depends on element locations (Fig. 2.10). σ_3' at the top of the fold crest begins to decrease after 30% shortening and increases again at 40% shortening, while σ_3' of the inner part of the fold crest increases throughout the buckling process (Fig. 2.10B). The timing when σ_1' at the fold crest reaches the maximum magnitude also depends on the element locations (Fig. 2.10C).

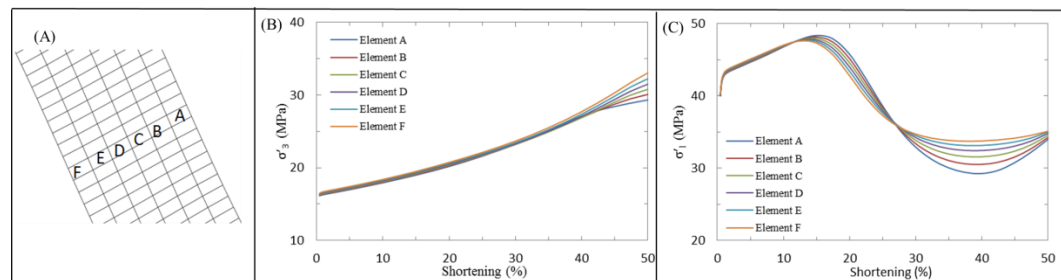


Fig. 2.9. The fold limb's stress evolution during buckling. (A) Locations of investigated elements in the fold limb; (B) σ_3' evolution; (C) σ_1' evolution (Fig. after Liu, 2013).

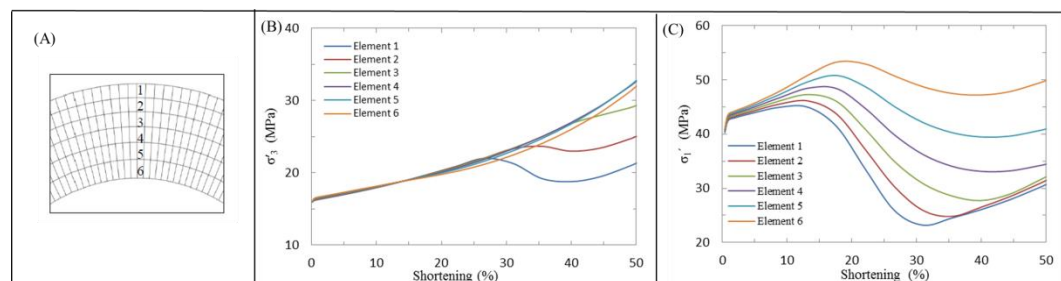


Fig. 2.10. The fold crest's stress evolution during buckling. (A) Locations of investigated elements in the fold crest; (B) σ_3' evolution; (C) σ_1' evolution. (Fig. after Liu, 2013).

Liu (2013) also points out that both fold layer viscosity and overburden pressure have an influence on the evolution of the principal stresses and tensile failure initiation. The viscosity ratio between the folded layer and the matrix will affect the fold shape. Furthermore, σ_3 will decrease after 30% shortening and tensile stress will be initiated for high viscosity folds. Tensile failure is more likely to be initiated for low overburden pressure folds.

3. MODELING METHOD

A continuous physical process is described by the governing partial differential equation (PDE) in which one dependent variable depends on more than one independent variable. Thus, reaching an analytical solution is difficult when the boundary conditions for a physical process are complex. Numerical modeling such as the finite element method provides an approximated solution for such cases. Dieterich and Carter (1969) first use this method to study geological deformations and stress history for folding.

3.1. FINITE ELEMENT METHOD IN ABAQUS™

3.1.1. Finite Element Analysis. The finite element analysis (FEA) offers an approximation method that can be used to solve PDEs. In the FE method, the continuous problem domain is divided into finite small segments, termed finite elements (Fig. 3.1). The inter-connected points of elements (red dots in Fig. 3.1) are nodes.

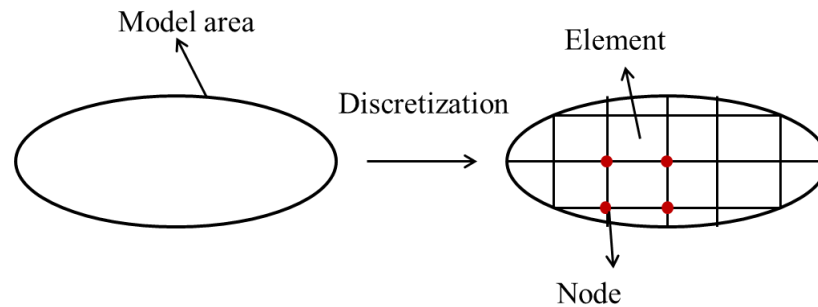


Fig. 3.1. Sketch of discretization in FE method. The cubes closed by black lines are elements. The red dots represent nodes.

The force-displacement relationship for each element is

$$q^e = K^e u^e + f^e \quad (19)$$

where q^e is the nodal force and K^e is the element stiffness matrix. Thus $K^e u^e$ is the force induced by displacements on the nodes, and f^e represents the nodal forces required to balance any load acting on the element.

Applying the condition of force equilibrium at all the nodes, the contributions of all elements can be assembled in the general equation of the finite element method:

$$\vec{K}\vec{u} + \vec{f} = 0 \quad (20)$$

where K is the global stiffness matrix.

In order to find an approximate solution at any point of the modeled domain, shape functions (N_a) are introduced to give an approximating displacement of each node for an element. As a result, both the state of stress and the strain within each element can be uniquely defined. Different elements have different shape functions. The displacement can be presented as

$$\vec{u} = \sum_a \vec{N}_a \tilde{u}_a^e \quad (21)$$

where \tilde{u}_a^e is the node's approximate displacement.

The state of stress for any point can be then solved by inserting approximations and boundary conditions into the assembled global matrix K .

3.1.2. Equations System to be Solved by ABAQUSTM. In this research, numerical models have a viscoelastic rheology and effective principal stress is analyzed. To obtain the state of stress and pore pressure, 7 unknowns (i.e., stress tensor components σ_{xx} , σ_{zz} and σ_{xz} ; the pore pressure P_p ; the material velocities in x and z directions v_x , and v_z , the material density ρ) need to be solved by ABAQUS. For Maxwell viscoelastic rheology where strains are additive (Schmalholz et al., 2001), the following 7 governing equations are solved by ABAQUS to obtain a unique solution for these 7 unknowns (i.e., Ockendon, 1995; Turcotte and Schubert, 2002; Jaeger et.al, 2007).

Based on conservation of momentum, the stress equilibrium equations are (Jaeger et.al, 2007):

$$\frac{\partial(\sigma_{xx}-\alpha P_p)}{\partial x} + \frac{\partial\sigma_{xz}}{\partial z} = 0 \quad (22)$$

$$\frac{\partial(\sigma_{zz}-\alpha P_p)}{\partial y} + \frac{\partial\sigma_{xz}}{\partial x} + \rho g = 0 \quad (23)$$

where σ_{xx} , σ_{zz} and σ_{xz} are the stress tensor component, α is Biot coefficient, ρ is the material density, and P_p is pore pressure.

The total strain rate for Maxwell viscoelastic rheology is given as (Ockendon, 1995; Turcotte and Schubert,2002):

$$\dot{\epsilon}_{xx} = \dot{\epsilon}_{xx}^e + \dot{\epsilon}_{xx}^f = \frac{1}{3K} \dot{\sigma}_{xx}^{iso} - \frac{\alpha}{3K} \dot{P}_p + \frac{1}{2G} \dot{\sigma}_{xx}^{dev} + \frac{\sigma_{xx}^{dev}}{2\mu} \quad (24)$$

$$\dot{\epsilon}_{zz} = \dot{\epsilon}_{zz}^e + \dot{\epsilon}_{zz}^f = \frac{1}{3K} \dot{\sigma}_{zz}^{iso} - \frac{\alpha}{3K} \dot{P}_p + \frac{1}{2G} \dot{\sigma}_{zz}^{dev} + \frac{\sigma_{zz}^{dev}}{2\mu} \quad (25)$$

$$\dot{\epsilon}_{xz} = \dot{\epsilon}_{xz}^e + \dot{\epsilon}_{xz}^f = \frac{1}{2G} \dot{\sigma}_{xz}^{dev} + \frac{\sigma_{xz}^{dev}}{2\mu} \quad (26)$$

where $\dot{\epsilon}_{ij}^n$ is the strain rate in which the superscript “e” represents the linear elastic contribution and “f” represents the linear viscous contribution; K is the bulk modulus; G is the shear modulus; μ is shear viscosity; and the superscripts “iso” and “dev” represent the isotropic part and deviatoric part of the stress tensor, respectively.

The conservation of mass for compressible rocks is given as:

$$\frac{\partial\rho}{\partial t} + \nabla \cdot (\rho \vec{v}) = \frac{\partial\rho}{\partial t} + \rho \left(\frac{\partial v_x}{\partial x} + \frac{\partial v_z}{\partial z} \right) = 0 \quad (27)$$

where v_x and v_z are the material velocities in x and y directions, respectively.

The conservation of mass for fluid mass is given as:

$$\frac{Kk_x}{\mu_f} \frac{\partial^2 P_p}{\partial x^2} + \frac{Kk_z}{\mu_f} \frac{\partial^2 P_p}{\partial z^2} - \frac{\partial P_p}{\partial t} + \dot{\sigma}^{iso} = 0 \quad (28)$$

where k_x and k_z are the permeabilities in the x and z directions, respectively.

3.1.3. Using ABAQUS to Model Folding. Biot (1961) suggests that the initial perturbation is an essential condition for the generation of buckling folds. Liu (2013) proved that the final fold shape and resultant strain in a fold is extensively affected by the initial perturbation.

A dominant wavelength is determined and used for all numerical models. This study focused on viscoelastic rheology. It is necessary to decide whether elastic properties or viscous properties control the dominant wavelength. Schmalholz and Podladchikov (1999) present an approach that can be used to select an appropriate dominant wavelength. They suggest that, if $\lambda_{dv}/\lambda_{de} > 1$, the dominant wavelength is primarily controlled by elastic properties. If $\lambda_{dv}/\lambda_{de} < 1$, the dominant wavelength is dependent on the viscous properties.

$$\frac{\lambda_{dv}}{\lambda_{de}} = \sqrt[3]{\frac{\mu_f}{6\mu_m} \sqrt{\frac{P_0}{G}}} \quad (29)$$

where $P_0 = 4\mu_f \cdot \dot{\epsilon}$ is the layer parallel stress, and G is the rock's shear modulus. Based on P_0 for the competence contrast (chapter 3.2) of 50, $\lambda_{dv}/\lambda_{de}$ is 0.117. Thus, viscous properties are used to calculate the model's dominant wavelength. λ_d can be calculated as (Biot & Ramberg, 1961):

$$\frac{\lambda_d}{h} = 2\pi \left(\frac{\mu_f}{6\mu_m} \right)^{1/3} \quad (30)$$

The dominant wavelength for these models employed in this study is 382.2m.

3.2. MATERIAL PROPERTIES

Proper material properties are crucial to the FE analysis of any geological research. Poisson's ratio, viscosity, porosity, permeability, density, and Young's modulus

each need to be defined as material property parameters when buckling is simulated within visco-elastic rheology.

Poisson's ratio is one of the five elastic constants of a rock; it is defined as lateral strain over longitudinal strain and is between 0 and 0.5. The Poisson's ratio used in this study is set to be 0.25, a typical value for sedimentary rock, for both matrix layer and folding layer.

The viscosities of the matrix layer and the folding layer are listed in Table 3.1. The competence contrast (R) for viscosity is 50.

$$R = \frac{\mu_{fold\ layer}}{\mu_{matrix}} = 50 \quad (31)$$

Porosity is reduced as the burial depth increases for most sedimentary rocks. This reduction for rocks whose burial depth is down to 2500m-3000m is mainly caused by mechanical compaction (Ramm, 1992). However, quartz cementation, which is beyond the extent of this research, takes more control of this trend for deeper rocks. The overburden thickness in this study varied from 500m to 3000m. Thus, porosity is primarily reduced by mechanical compaction. Medina and Rupp's (2011) relationship between porosity and depth is applied here to calculate porosity:

$$\Phi(d) = 16.39 \times e^{-0.00039d} \quad (32)$$

where d is the depth (m), and Φ is the porosity (%).

"Permeability" is used to describe a rock's ability to allow fluid to flow through rock pores such that changes in porosity will produce changes in permeability. Medina and Rupp (2011) suggest the following permeability-porosity relationship:

$$k = 7.583 \times 10^{-17} \times e^{0.283\Phi} \quad (33)$$

where k is a rock's permeability (m^2), and Φ is a rock's porosity (%).

Dry density (ρ_d) is the density of a unit volume rock without any fluid in it, which is applied in this study. Specific gravity (G_s) is the ratio of unit volume rock mass to the mass of same volume water. It is used in this study to derive the dry density:

$$\rho_d = G_s \rho_w \times (1 - \Phi) \quad (34)$$

where ρ_w is the water's density (kg/m^3), Φ is the rock's porosity (%), and G_s is 2.75 (Turcotte & Schubert, 2002).

Young's modulus, also known as the elastic modulus, can be calculated as (Fjar et al., 2008):

$$E = 2V_s^2(1 + \nu)\rho_d \quad (35)$$

where E is Young's modulus (Pa), V_s is the seismic S-wave velocity (m/s), ν is Poisson's ratio, and ρ_d is the rock's dry density (kg/m^3). The S-wave velocity of typical sandstone is 2400m/s.

Table 3.1. Model's material properties of both the folding layer and the matrix

Properties	Folding layer	Matrix
Specific gravity	2.75	2.75
Viscosity (Pa·s)	10^{21}	2×10^{19}
Poisson's ratio	0.25	0.25
Permeability (m^2)	$7.583 \times 10^{-17} \times e^{0.283\Phi}$	$7.583 \times 10^{-17} \times e^{0.283\Phi}$
Young's modulus (GPa)	$39.6 \times (1 - 0.1639e^{-0.00039z})$	$3.96 \times (1 - 0.1639e^{-0.00039z})$
Strain rate (s^{-1})	10^{-14}	10^{-14}
Erosion rate (mm/y)	1	1

3.3. MODEL GEOMETRY AND BOUNDARY CONDITIONS

The numerical model geometry of this research included two parts: a matrix and an embedded competent layer (see Fig. 3.2). The model is 1911m long, the matrix below the embedded competent layer is 1000m, and the overburden above this layer varied between 500m and 3000m. The embedded competent layer is 30m thick with periodic, sinusoidal, small perturbations of the dominant wavelength described previously.

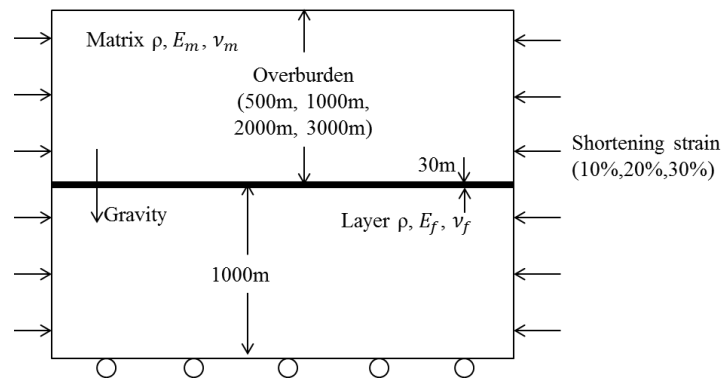


Fig. 3.2. Model sketch and boundary conditions of the numerical models used.

The entire system is subjected to lateral shortening. The shortening strain is between 10% and 30%, with an increment of 10% (see Table 3.2). The strain rate is 10^{-14}s^{-1} (Watt, 1987). The bottom of the model is fixed in the y -direction. The top is a free surface that had zero pore pressure throughout the buckling process.

Table 3.2 Overburden and shortening combinations for basic models

Overburden (m)	500			1000			2000			3000		
Shortening (%)	10	20	30	10	20	30	10	20	30	10	20	30

3.4. SIMULATION PROCESS

3.4.1. Pre-stressing. Rocks that are present in nature are always in equilibrium with all applied forces and load (Twiss and Moore, 2007). In numerical models without pre-stressing, gravity is applied to a rock volume suddenly and an undesirable vertical displacement occurs. Thus, a proper initial state of stress must be considered for a folding system within a numerical model. Only gravity is applied in the pre-stressing step to obtain a state of stress that is in gravitational equilibrium.

Preparing such called “pre-stressed” numerical models is the first step of the simulation (Fig. 3.3). Only gravity and the following boundary conditions without shortening are applied. Gravity is applied to all elements, and the initial pore pressure is assumed to be hydrostatic. All boundaries are restricted except the top. The movements of left and right nodes are restricted in x-direction and can only move in y-direction. The bottom nodes are constrained in y-direction. The top is free surface with zero pore pressure.

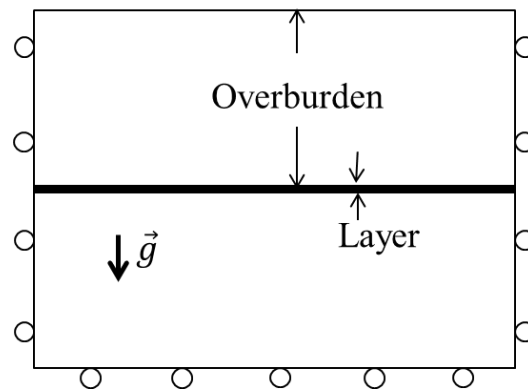


Fig. 3.3. Gravitational pre-stressing model sketch. Only gravity is applied and model sides are constrained (rollers).

As a result, a realistic initial state of stress and the vertical elastic compaction induced by gravity are obtained. Four overburden thicknesses are simulated in this study:

500m, 1000m, 2000m, and 3000m. With the rock parameters listed in Table 3.1, the unrealistic vertical elastic compactions for the four overburden conditions in the pre-stressing process are 5.18m, 10.42m, 20.66m, and 36.7m, respectively. The undesirable vertical displacements are eliminated before the folding process so that both the realistic state of stress and the correct vertical displacement could be simulated.

3.4.2. Buckling. In the second step, gravity and layer-parallel shortening is applied to generate buckle folds and simulate the realistic stress history of folding process after pre-stressing (Fig. 3.4). Gravity is applied for all elements, and layer-parallel shortening is applied as boundary conditions.

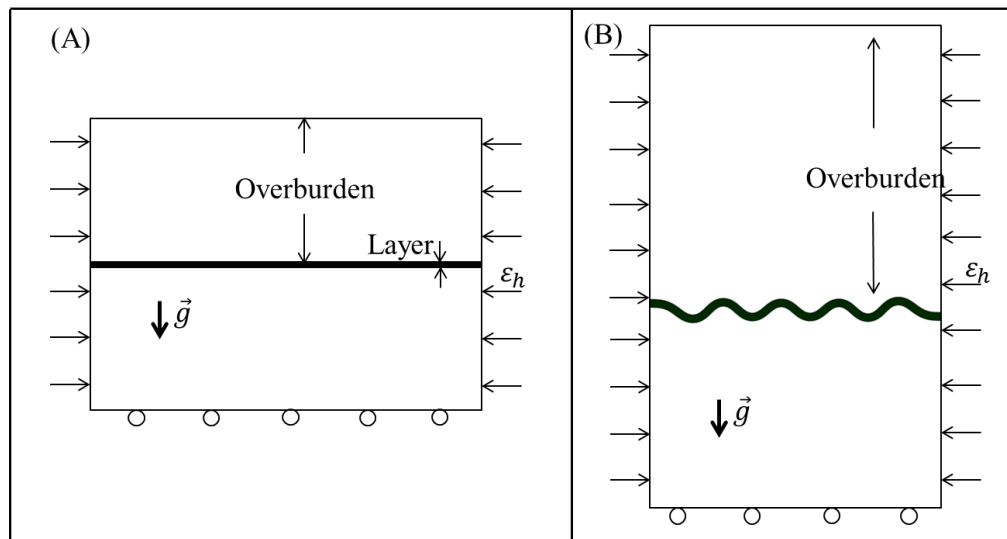


Fig. 3.4. Buckling model sketch. (A) A constant horizontal strain added to the pre-stressed model; (B) Buckle fold is generated after certain amount of shortening.

3.4.3. Erosional Unloading. After the buckle fold is generated, the erosional unloading step is applied to the numerical models (Fig. 3.5). The erosion process will remove materials from the Earth's surface. However, it is impossible to remove elements continuously in ABAQUS. The erosional unloading process is simulated by reducing the

gravitational acceleration magnitude of the overburden elements linearly so that the weight of overburden is reduced continuously.

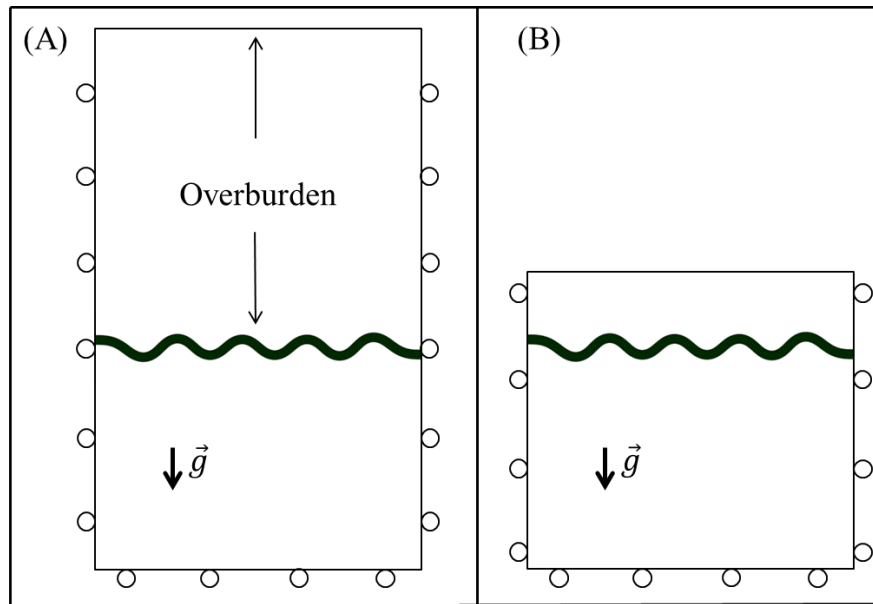


Fig. 3.5. Model sketches for erosional unloading process. (A) At the beginning of erosion, only vertical displacements are enabled. (B) Certain amount of overburden weight is reduced after a certain period of geological time.

4. RESULTS

4.1. INTRODUCTION

In this study, a number of numerical models are simulated to study the initiation of tensile failure in single-layer buckle folds, particularly during the erosional unloading process which occurs post-folding. As an indicator for the initiation of tensile failure, the evolution of the minimum principal stress (σ_3') is considered. In order not to make an assumption regarding the tensile strength of the rock, tensile failure will be initiated when the condition of $\sigma_3' = 0$ is met. The effects of erosion rate and rheology on erosion process are considered.

It is revealed from Ramsay's (1967) study that the top of the fold crest is the most likely position for tensile failure to occur in low amplitude buckling fold. Reif et al. (2011) show in their study of the Zagros fold-and-thrust belt that joints and tension gashes in NW-SE striking structures are commonly identified in the upper folded formation. Thus, the top of the crest is the point of most interest in this study for tensile failure to occur. Liu (2012) concludes that the erosional unloading process will amplify the remnant strain in the fold body. Thus, tensile stress may be generated on the fold limb during buckling and erosional unloading process. Considering that the stress development of the fold limb is independent of the element location (Liu, 2013), the middle element of the limb and the top of the fold crest are the selected interest points of this study.

In order to investigate the minimum amplitude for tensile stress being initiated, a variety of relevant processes and properties are studied and presented in the following sections:

- 4.1.1 investigates when σ_3' switches orientation during the buckling process;
- 4.2 compares the viscoelastic erosion rheology and elastic rheology, and the elastic erosion rheology is applied in this study;
- 4.3; illustrates that there is no influence of erosion rate on the evolution of the stresses during elastic erosional unloading process;
- 4.4 investigates the influence of the amount of shortening on the reduction rate of stress during erosion process;

- 4.5 presents the initiation of tensile stress on both the fold crest and the fold limb for different overburden thicknesses models with the same amount of shortening (30%);
- 4.6 investigates which is the lowest folds amplitude to generate tensile stress during erosion process.

4.1.1. Evolution of Stress during Buckling. Because the condition of $\sigma_3' = 0$ is of interest, it is important to analyze which stress component is the minimum effective stress during buckling. Fig. 4.1 presents the evolution of horizontal stress (S_{11}) and vertical stress (S_{22}) for the top of the fold crest with 1000m overburden thickness throughout 30% shortening. The stress development for different overburden thickness models is similar with each other. The horizontal stress increases initially when horizontal layer shortening occurs, and decreases when buckling is initiated. The horizontal stress decreases rapidly between 10% and 20% shortening. The vertical stress increases slightly throughout the entire buckling process, because the overburden thickness increases continuously during the buckling process as the model thickens. It is clear that the vertical stress is the minimum effective stress until 16% shortening. After that, the horizontal stress decreases to be less than the vertical stress, and the horizontal stress is the minimum effective stress till the end of buckling. The time when the minimum effective stress switches from vertical stress to horizontal stress is independent of overburden thickness (see Appendix).

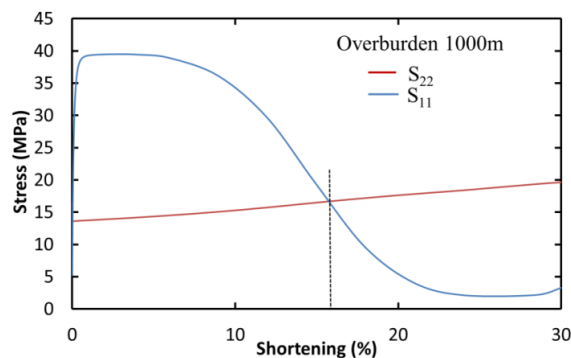


Fig. 4.1. Stress evolution on the top of the fold crest with 1000m overburden thickness throughout 30% shortening process.

The evolution of S_{11} and vertical S_{22} for the fold limb with 1000m overburden thickness throughout 30% shortening is presented in Fig. 4.2. The trends of the stress development for different overburden thickness models are similar with each other (see Appendix). But it is different from that of the fold crest. S_{22} is always smaller than S_{11} throughout 30% shortening. However, S_1 and S_2 in the fold limb are no longer the horizontal principal stress and vertical principal stress any more. The orientations of the principal stresses on the limb are presented in Fig. 4.3.

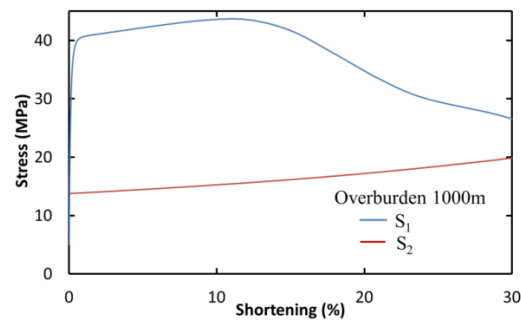


Fig. 4.2. Stress evolution on the fold limb with overburden thickness 1000m throughout 30% shortening.

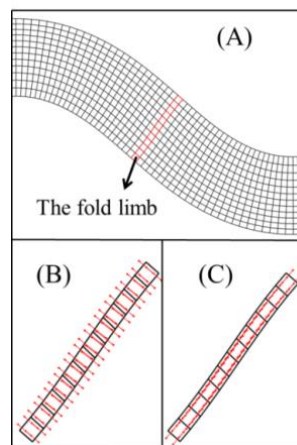


Fig. 4.3. Stress orientation in the fold limb. (A) The location of the fold limb that is investigated in this study; (B) The orientation of S_1 in the fold limb (the red line); (C) The orientation of S_2 in the fold limb (the red line).

4.2. RHEOLOGY INFLUENCE ON EROSION

The rheology controls the state of stress during both buckling process and the erosional unloading process. Since the buckling process is simulated as a visco-elastic deformation process, the erosion process is both simulated for visco-elastic and elastic rheology. After elastic erosion, where uni-axial strain boundary condition are applied, the minimum effective stress can be calculated by the following equation:

$$\sigma_{3e}' = \sigma_3' - \frac{\nu}{1-\nu} \rho gh \quad (36)$$

where σ_{3e}' is the minimum effective stress during the erosion, σ_3' is the minimum effective stress at the end of buckling, ν is Poisson's ratio, and ρ is the rock density.

The evolution of minimum effective stress under the visco-elastic erosion process is compared to that of elastic erosion. The state of stress in both the crest and the limb for the visco-elastic erosion process are investigated.

4.2.1. Minimum Effective Stress Evolution. The evolution of the minimum effective stress for both elastic erosion models and visco-elastic models are presented in Fig. 4.4A and 4.4B for the top of the fold crest, respectively. Tensile stress has been reached at 18% shortening for 500m overburden model. Thus, the discussion is based on the other three overburden thicknesses (1000m, 2000m, and 3000m). For the visco-elastic models, all the overburdens are eroded, while the erosion process is stopped when tensile stress occurs for the elastic erosion models. The observations are summarized as follows:

- (1) The most interesting finding is that σ_3' for visco-elastic erosion models has an immediate increase about 15MPa at the end of buckling (the beginning of the erosion process), and decreases as the erosion process goes on (see Fig. 4.6A). But it decreases immediately from the beginning of erosion process for elastic erosion models (see Fig. 4.6B).
- (2) σ_3' on the fold crest declines linearly throughout both the visco-elastic erosion process and elastic erosion process for any overburden thickness showed in Fig. 4.6. The σ_3' decline rates for each overburden thickness of each erosion rheology are similar, which is -1.9×10^{-5} MPa/y for visco-elastic erosion and -1.58×10^{-5} MPa/y for elastic erosion.

- (3) For elastic erosion models, tensile stress can be generated on the fold crest for each overburden thickness during the erosion process. However, tensile stress cannot be developed for the large overburden thickness models (2000m and 3000m) which undergo visco-elastic erosion, even though all the overburdens are eroded.

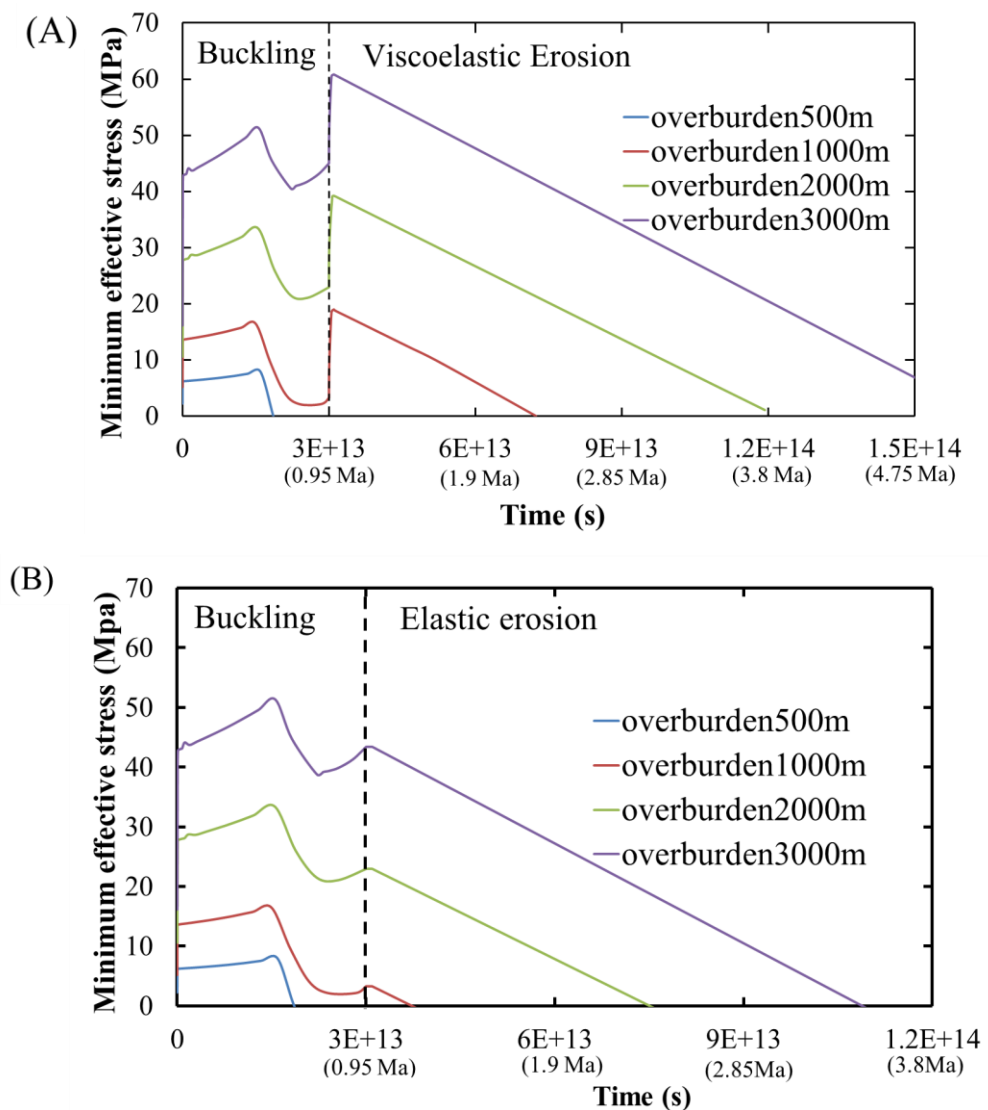


Fig. 4.4. The evolution of σ_3' on fold crest top throughout the entire process, including buckling and viscoelastic erosion. (A) Visco-elastic erosion; (B) Elastic erosion.

Fig.4.5 presents the evolution of the fold limb's minimum effective stress for both elastic erosion models and visco-elastic models. There is no tensile stress generated during buckling process for each overburden thickness models. The observations are similar to that found on the fold crest:

(1) σ_3' for visco-elastic erosion models also increases immediately at the end of buckling (the beginning of erosion process) and decreases as the erosion process goes on (see Fig. 4.5A), while it decreases immediately from the beginning of the erosion process for elastic erosion models (see Fig. 4.5B).

(2) σ_3' on the fold limb decreases linearly throughout both the visco-elastic erosion process and elastic erosion process for any overburden thickness shown in Fig. 4.5. The σ_3' decrease rates for both visco-elastic erosion and elastic erosion are the same as those of fold crest, respectively.

(3) For elastic erosion models, tensile stress can be generated on the fold limb for each overburden thickness during erosion process. However, tensile stress can only be developed for the small overburden thickness models (500m) which undergo visco-elastic erosion, even though all the overburden is eroded.

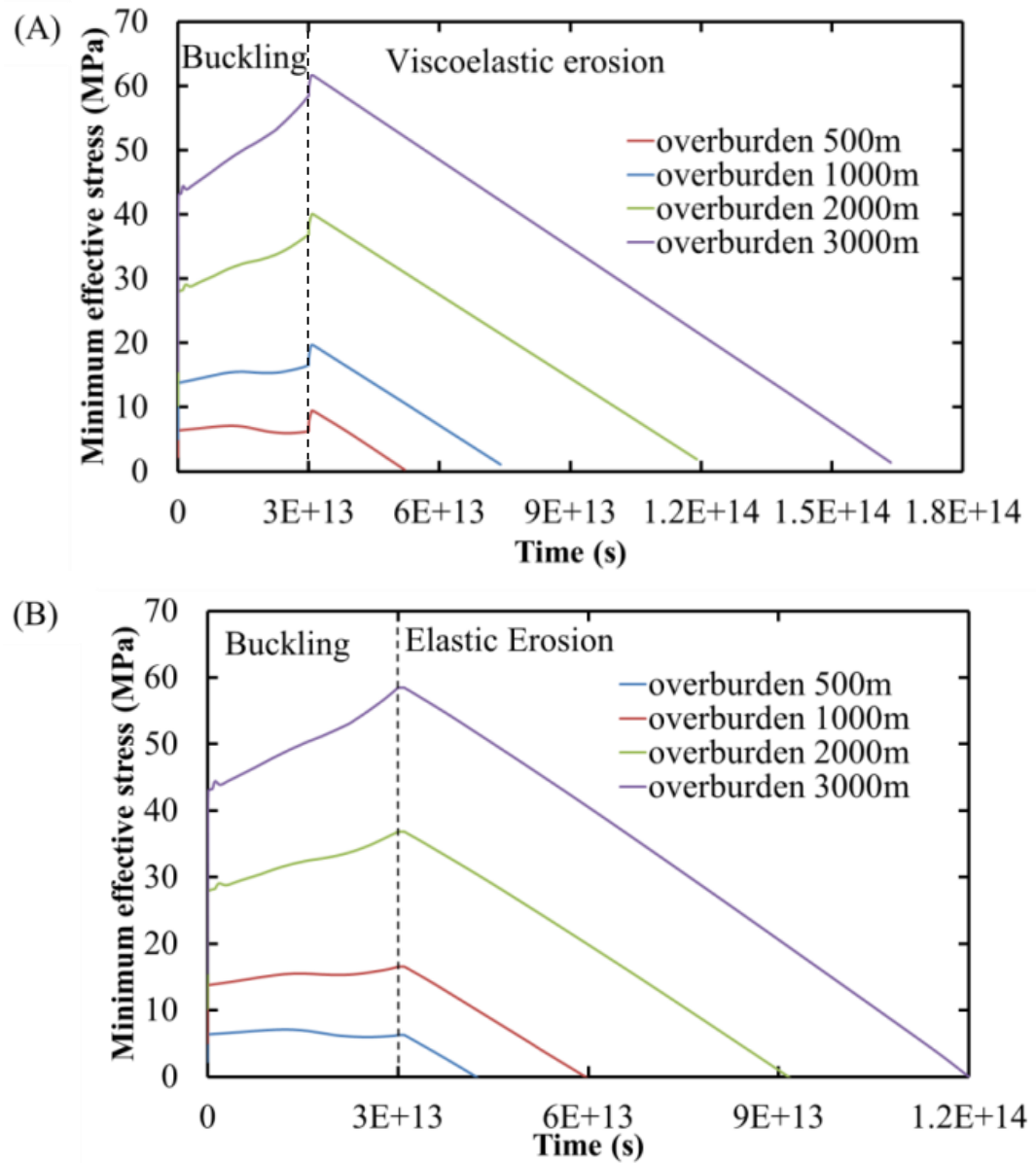


Fig. 4.5. The evolution of σ_3' on the fold limb throughout the entire process, including buckling and viscoelastic erosion. (A) Visco-elastic erosion; (B) Elastic erosion.

4.2.2. Principal Stress Evolution for Visco-elastic Erosion Rheology.

Both Fig. 4.4 and 4.5 illustrate that the σ_3' of both the fold crest and the fold limb increase immediately at the beginning of viscoelastic erosion process. Thus, it is necessary to investigate the evolution of effective principal stresses throughout the entire

process for visco-elastic erosion process. The evolution is presented in Fig. 4.6 for the fold crest and in Fig. 4.7 for the fold limb.

The most interesting finding is that the minimum effective stress increases immediately at the beginning of viscoelastic erosion to equilibrate with the maximum effective stress (see Figs. 4.6 and 4.7). This occurs because the horizontal deformation is terminated and the uni-axial strain boundary condition is applied. Once horizontal compression is ceased the viscoelastic creep rheology seeks stress equilibrium and the two effective principal stresses are the same throughout the viscoelastic erosion process for all the visco-elastic erosion models. The reason is that the viscous property controls the deformation of the rock. The rock deforms like a viscous fluid so that the stresses in all directions tend to be the same magnitude, and there is no differential stress throughout the viscoelastic erosion process. Thus, no Mohr circle can be drawn under this condition and no shear failure will occur.

Tensile stress is hard to be generated in the rock with fluid-like property during the viscoelastic erosion. Moreover, because of the viscous property of the rock, plasticity should be considered. Thus, only elastic erosion rheology is considered for the erosion/exhumation process

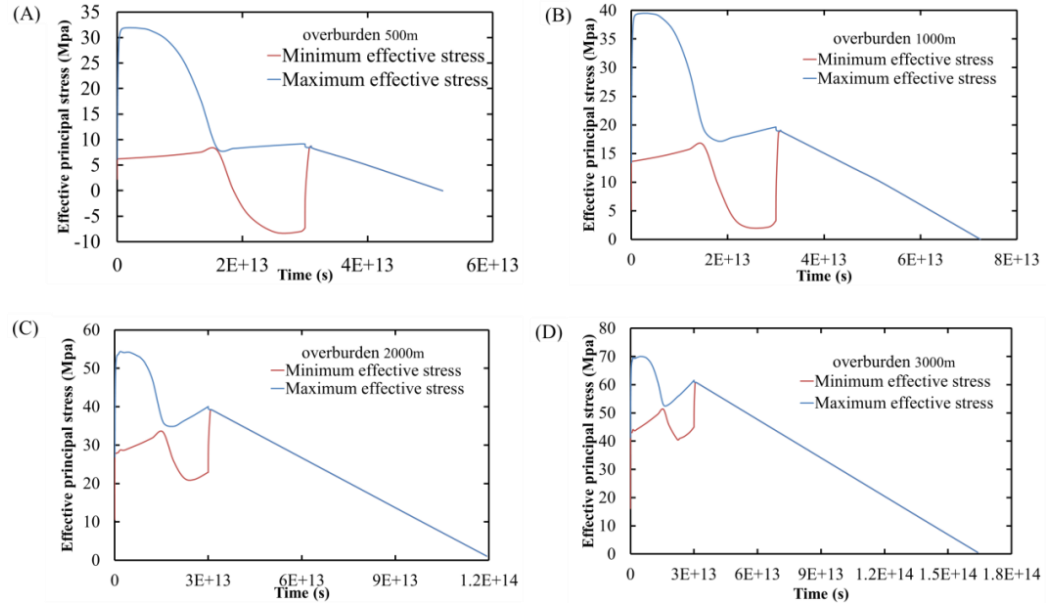


Fig. 4.6. Fold crest effective principal stress evolution throughout 30% shortening and viscoelastic erosion. (A) Overburden 500m; (B) Overburden 1000m; (C) Overburden 2000m; (D) Overburden 3000m.

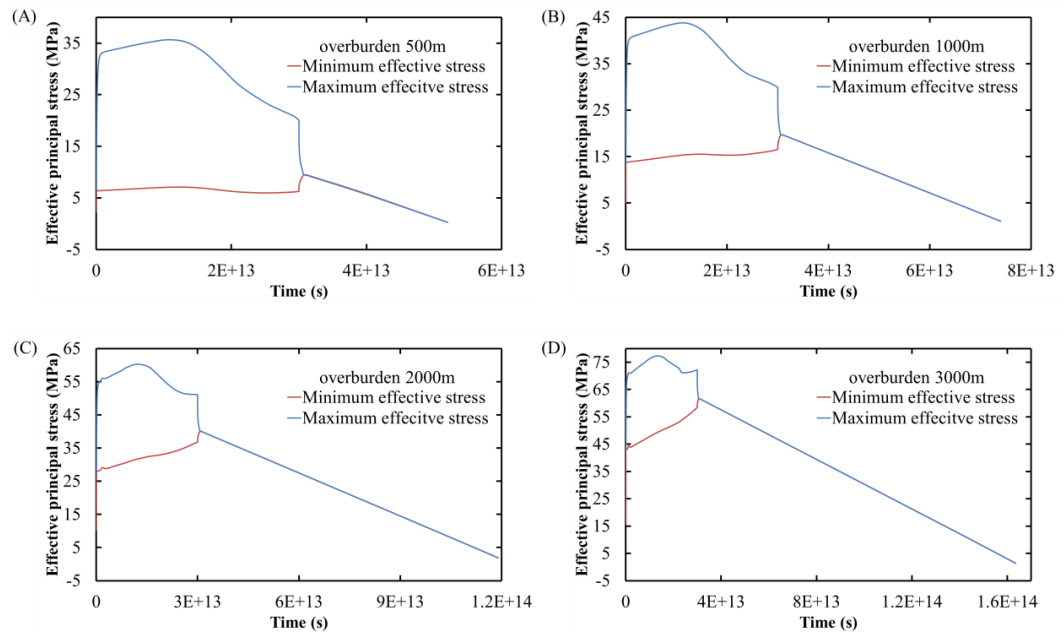


Fig. 4.7. Fold limb effective principal stress evolution throughout 30% shortening and viscoelastic erosion. (A) Overburden 500m; (B) Overburden 1000m; (C) Overburden 2000m; (D) Overburden 3000m.

4.3. INFLUENCE OF EROSION RATE

Erosion process will reduce the magnitude of vertical stress, and has impact on the horizontal stress as well (Molnar, et. al. 2007). Initially it is tested if the erosion rate will affect the state of stress during the erosional unloading process, before analyzing the effect of erosion process on the state of stress.

Two erosion rates are simulated for this section: 1) 1 mm/y; 2) 0.1 mm/y. The material properties, as shown in Table 3.1, the 1000 meter original overburden and 30% shortening remain constant. The stresses of the top element of the fold crest and of the middle of the limb are analyzed.

Fig. 4.8 shows the stress evolution of the top element of the fold crest's. In Fig. 4.8A, it is apparent that the trends of the effective minimum stress (σ_3') evolution for these two erosion rates are equivalent. Fig. 4.8B also shows the same outcomes for the differential stress (σ_d) evolution for these two erosion rates. The same conclusions for the middle element of the limb can be drawn from Fig. 4.9A and Fig. 4.9B.

It can be concluded that there is no influence of the erosion rate on the state of stress during the erosion process, based on the observations that the same stress evolution trend and the same state of stress can be reached under different erosion rates. Thus, it is reasonable to test only one erosion rate for the numerical models in this research, and the 1mm/y erosion rate is chosen (Twiss and Moores, 2007).

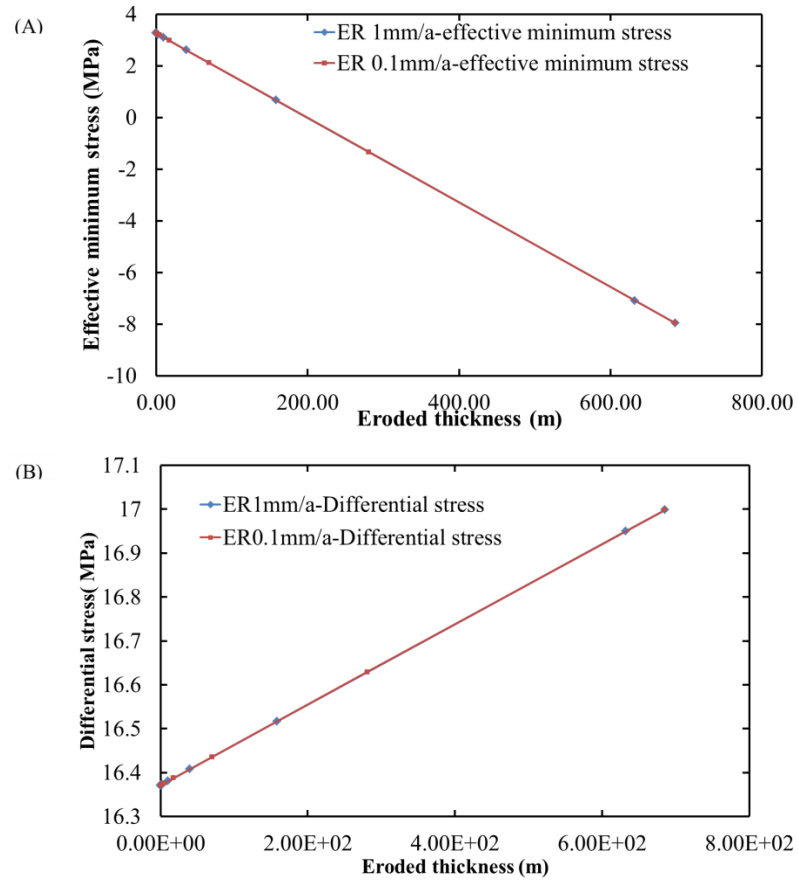


Fig. 4.8. Stress evolutions of the fold crest during erosional unloading process under different erosion rates. (A) Effective minimum stress (σ_3') of the top element of the fold's crest under different erosion rates for the same model. (B) Differential stress's (σ_d) of the top element of the fold's crest.

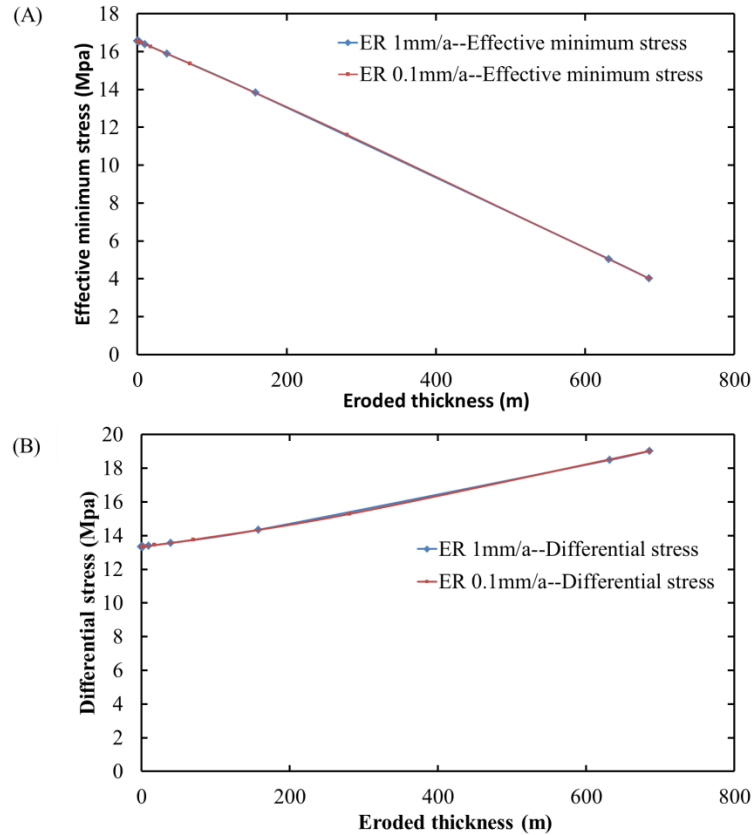


Fig. 4.9. Stress evolutions of limb during erosional unloading process under different erosion rates. (A) Effective minimum stress (σ_3') of the middle element of the fold's limb under different erosion rates for the same model. (B) Differential stress's (σ_d) of the middle element of the fold's limb.

4.4. INFLUENCE OF SHORTENING ON THE STATE OF STRESS DURING ELASTIC EROSION

4.4.1. Influence on the Stress Reduction Rate. The weight of the overburden decreases significantly during the erosional unloading process; this process will reduce the magnitude of the vertical stress, and has impact on the horizontal stress as well (Molnar et al., 2007). The basic models with 1000m initial overburden undergoing three different amounts of shortening are simulated to investigate the influence of shortening on the reduction rate of both horizontal stress and vertical stress during the erosion process. The eroded overburden thickness is 700m. Other material properties are listed in Table 3.1.

Fig. 4.10 presents the stress evolution of the fold crest during elastic erosion process. The rate of horizontal stress reduction on the fold crest during erosion process highly depends on the amount of shortening (see Fig. 4.10A). The larger the amount of shortening is, the higher the reduction rate of the horizontal stress will be. The reduction rates are -0.0059MPa/m , -0.0127MPa/m , and -0.0164MPa/m for 10% shortening, 20% shortening, and 30% shortening, respectively (Fig. 4.10A). However, in the uni-axial strain case, the reduction rate of σ_3 is -0.33 (Eq. 5). This is because the horizontal stress and strain are the results of the applied shortening in buckle folds. The more strain is included, the more amplified are the horizontal buckling strains in the fold. In contrast, the vertical stress only depends on the weight of the overburden. Thus, the reduction rates of vertical stress for different amount of shortening are the same during the erosion process (see Fig. 4.10B).

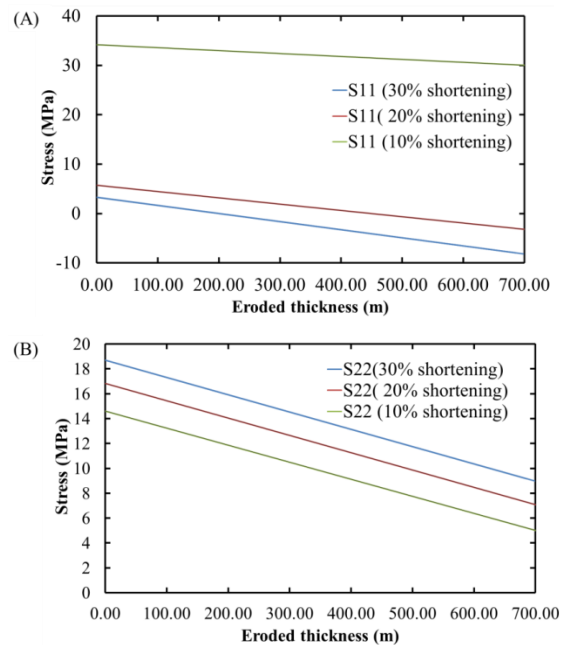


Fig. 4.10. Reduction rates of the fold crest's horizontal stress and vertical stress for different amount of shortening models (1000m overburden thickness) during elastic erosion process. (A) Horizontal stress evolutions for 30%, 20%, and 10% shortening during erosion process. The reduction rate increases as shortening increases. (B) Vertical stress evolutions for these three shortening during erosion process. The reduction rates are almost the same.

For the fold limb, the principal stresses do not coincide with the vertical and horizontal stresses anymore (see Fig. 4.3). Thus, minimum effective stress and maximum effective stress are considered here for the fold limb. The stress evolutions are presented in Fig. 4.11. It illustrates that both the reduction rates of the σ_3' and the σ_1' increases as the amount of shortening increases.

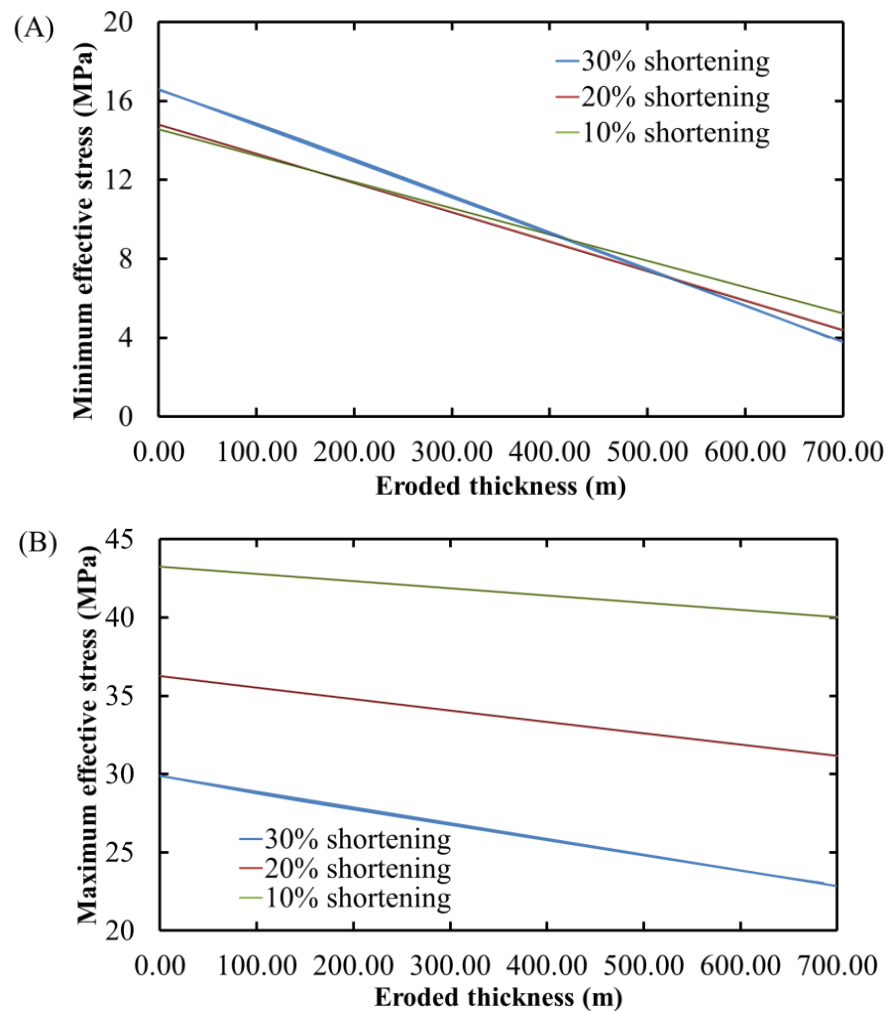


Fig. 4.11. Reduction rates of the fold limb's minimum effective stress and maximum effective stress for different amount of shortening models (1000m overburden thickness) during elastic erosion process. (A) Minimum effective stress evolutions for 30%, 20%, and 10% shortening during erosion process. The reduction rate increases as shortening increases. (B) Maximum effective stress evolution for these three shortening during erosion process. The reduction rate also increases as shortening increases.

4.4.2. Influence on the Orientation of the Tensile Stress in Erosion Process.

In order to study the orientation evolution of σ_3' during the post-folding erosion/exhumation process, two models of 1000m and 3000m initial overburden thickness are investigated. Erosion/Exhumation rate of 1mm/yr is applied and the erosion process is modeled as an elastic process. Fig. 4.12 and Fig. 4.13 present the orientation of σ_3' at the time when tensile stress is initiated for 1000m overburden and 3000m overburden models, respectively. The observations are summarized as follows:

- (1) For the 1000m overburden models, σ_3' is always horizontal when tensile stress is initiated for 30%, 40% and 50% shortening models (Fig. 4.12).
- (2) For the 3000m overburden models, σ_3' is horizontal when tensile stress is initiated for 30% and 40% shortening models (Fig. 4.13A and Fig. 4.13B). However, for 50% shortening model, it switches to be vertical when tensile stress is initiated (Fig. 4.13C).

The erosion process only affects the orientation of σ_3' in large overburden thickness and high amplitude fold. The simulations in this study are for low amplitude folds so that the orientation of σ_3' will not be affected by the erosion process.

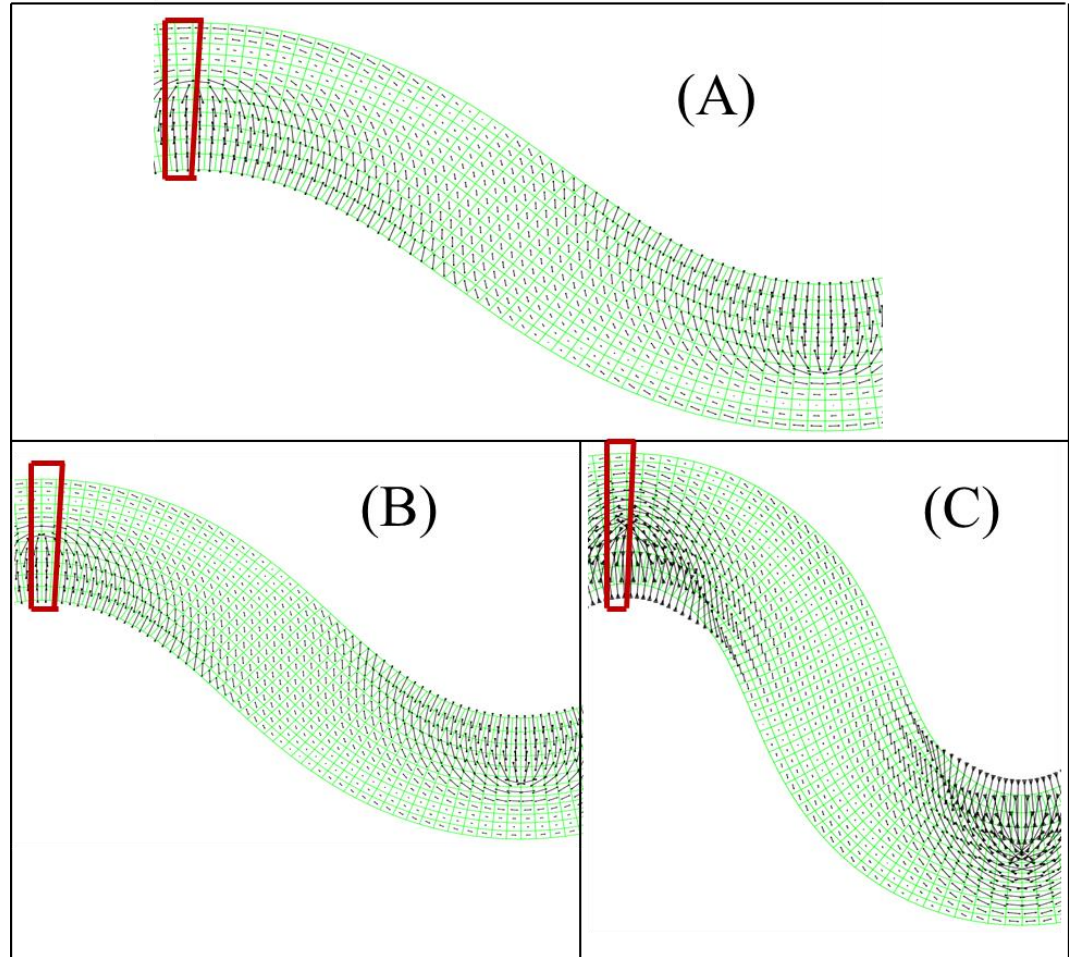


Fig. 4.12. The orientation of σ_3' at the time when tensile stress is initiated for 1000m overburden models. (A) Eroded after 30% shortening; (B) Eroded after 40% shortening; (C) Eroded after 50% shortening.

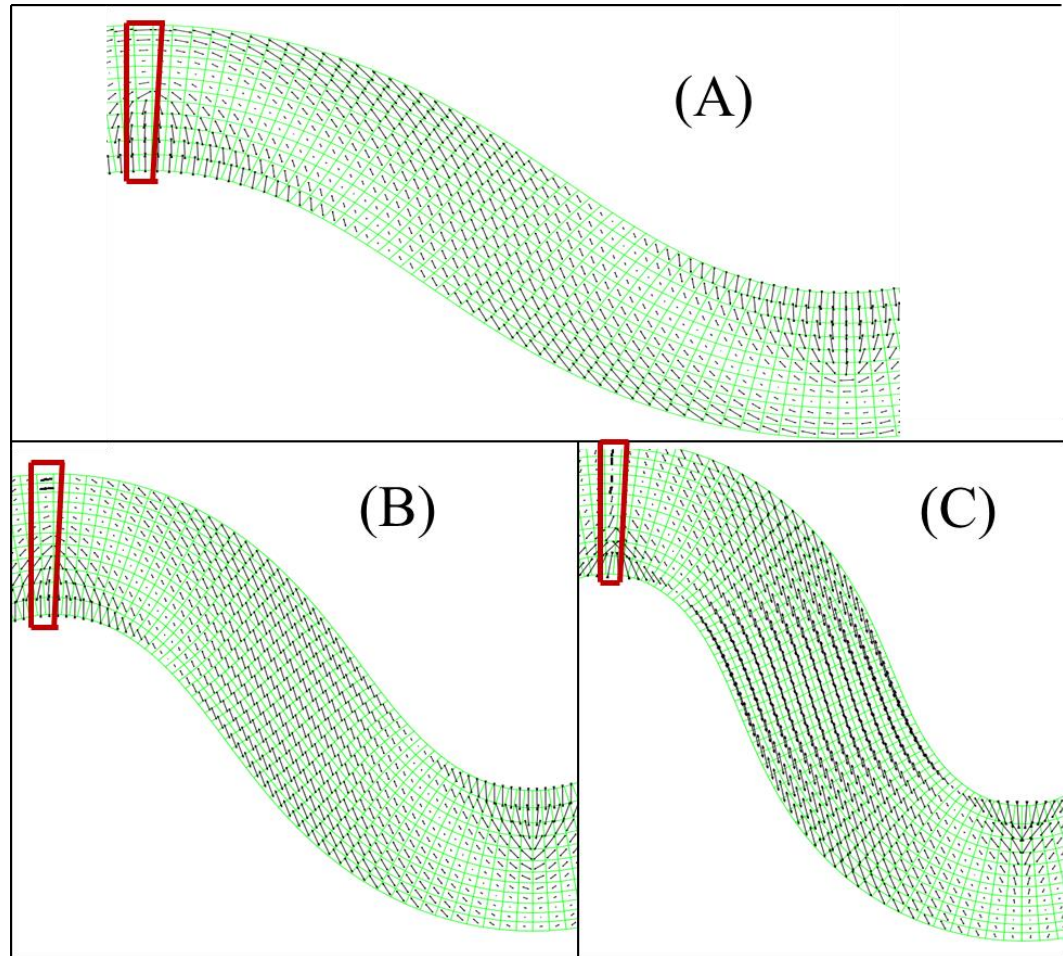


Fig. 4.13. The orientation of σ_3' at the time when tensile stress is initiated for 3000m overburden models. (A) Eroded after 30% shortening; (B) Eroded after 40% shortening; (C) Eroded after 50% shortening.

4.5. DIFFERENT OVERBURDEN THICKNESS FOR BASIC MODELS

4.5.1. Influence of Overburden Thickness. The influence of overburden thickness during buckling process is tested by Liu (2013). Liu conclude that tensile stress is likely to occur on the top of fold crest for low overburden loads during the buckling process. The minimum effective stress (σ_3') increases significantly in both fold crest and fold limb when overburden increases.

In this study, numerical models with different overburden thicknesses are simulated to investigate the influence of overburden stress on the elastic erosional unloading process after the low amplitude buckle fold developed. Four overburden

thicknesses are tested in this research: (1) 3000m; (2) 2000m; (3) 1000m; and (4) 500m. The amount of shortening is 30% which is the basic amount of shortening in this study. The remaining material properties are listed in Table 3.1.

The final overburden thicknesses after buckling for each initial overburden thickness are presented in Table 4.1. The development of σ_3' and σ_1' for the top element of the fold crest throughout the erosional unloading process are presented in Fig. 4.14. Both of these two stresses decrease linearly during this process. Tensile stress on the fold crest will be generated by this unloading process. Fig. 4.15 presents the stress evolution in the fold limb during erosion. The trend is the same as that for the top element of the fold crest shown in Fig. 4.14. Tensile stress can be developed in the limb when enough overburden thickness is eroded (Fig. 4.15A). However, the eroded overburden thickness for tensile stress being generated in the limb will be larger than that for the crest rock failure to be initiated. In this study, unloading process will be terminated when tensile stress reaches -10MPa in the crest to avoid the occurrence of unrealistic state of stress.

In summary, the overburden thickness has no effect on the stress evolution during the erosional unloading process, because the stress decreases at the same rate for each overburden thickness (See Fig. 4.14 and Fig. 4.15).

Table 4.1 The final overburden thickness at the end of buckling corresponding to each initial overburden thickness after 30% shortening

Initial overburden thickness (m)	Final overburden thickness (m)
500	655
1000	1367
2000	2785
3000	4213

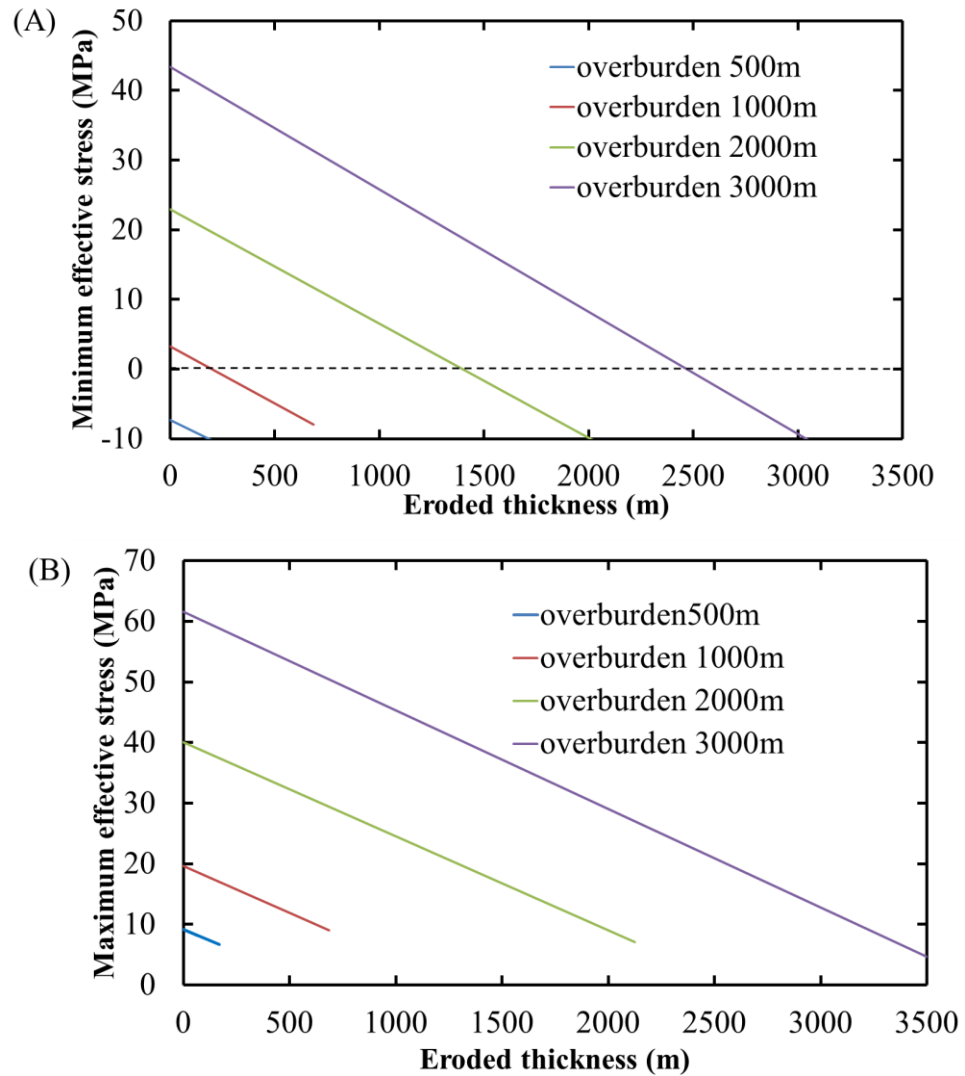


Fig. 4.14. Stress development of the fold crest during erosion under different initial overburden thickness. (A) σ_3' evolution of the top element of the fold crest; (B) σ_1' evolution of the top element of the fold crest.

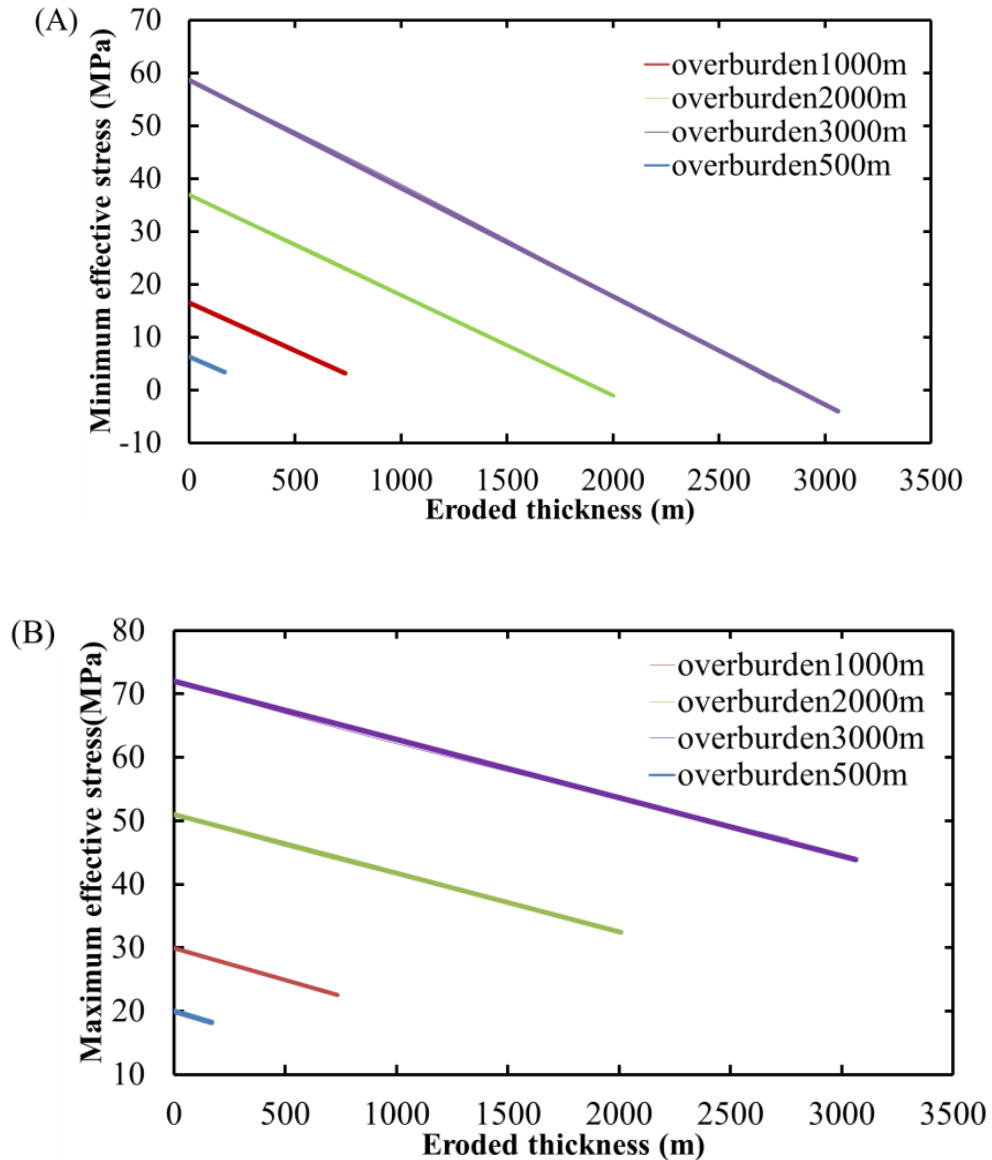


Fig. 4.15. Stress development of the fold limb during erosional unloading process under different initial overburden thickness. (A) σ_3' evolution of the middle element of the fold limb; (B) σ_1' evolution of the middle element of the fold limb.

4.5.2. Tensile Stress on the Crest during Erosion. The evolution of the stress during the erosional unloading process is independent of the overburden thickness. However, the influence of overburden thickness on the buckling process can still result in different times when tensile stress occurs during the erosion process. Four different overburden erosional models based on 30% shortening with basic material properties

listed in Table 3.1 are simulated to investigate the timing of the occurrence of tensile stress. The development of σ_3' in both buckling and erosion process and the initiation of tensile stress in the top element of fold crest are presented in Fig. 4.16. The occurrences of tensile stress are marked by red pentacles in Fig. 4.16. For the lowest depth case (500m), tensile stress develops during the buckling process (about 18.6% shortening) and is further amplified. For larger depths cases, there is no tensile stress generated during buckling process, but it will be generated during the erosional unloading process after 30% buckling. Thus, the timing of tensile stress initiation depends on the overburden thickness. The larger the overburden thickness is, the later the tensile stress will be generated.

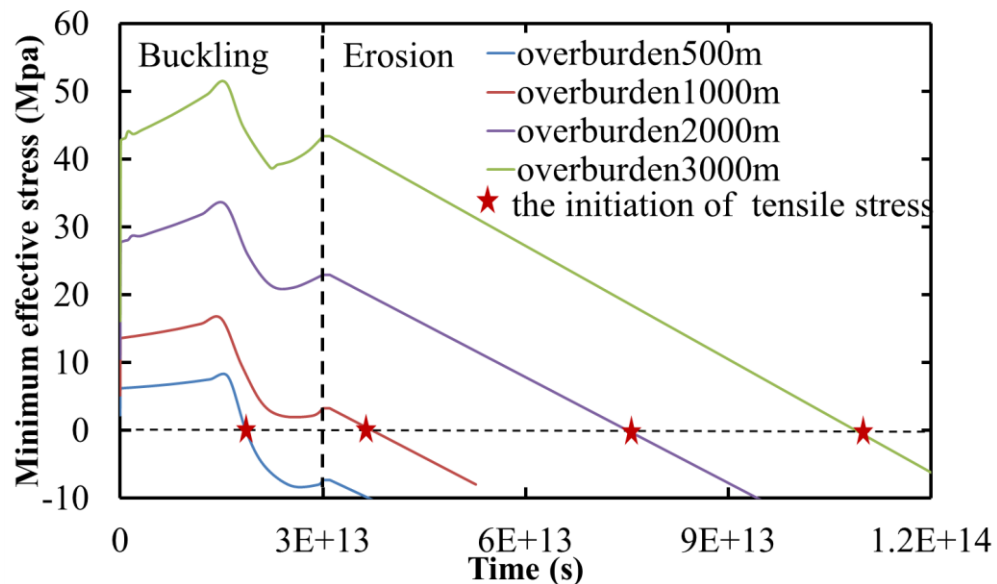


Fig.4.16. The evolution of the fold crest's minimum effective stress throughout both 30% buckling and the following erosion process.

All cases in this model set generate tensile stress and tensile failure on the top of the fold crest. The Mohr circles illustrating the state of stress for the marked points in Fig. 4.16 are presented in Fig. 4.17. The Mohr circle gets larger as the initial overburden

thickness increases. It suggests that the maximum effective stress will get larger as initial overburden thickness increases when the tensile failure is initiated.

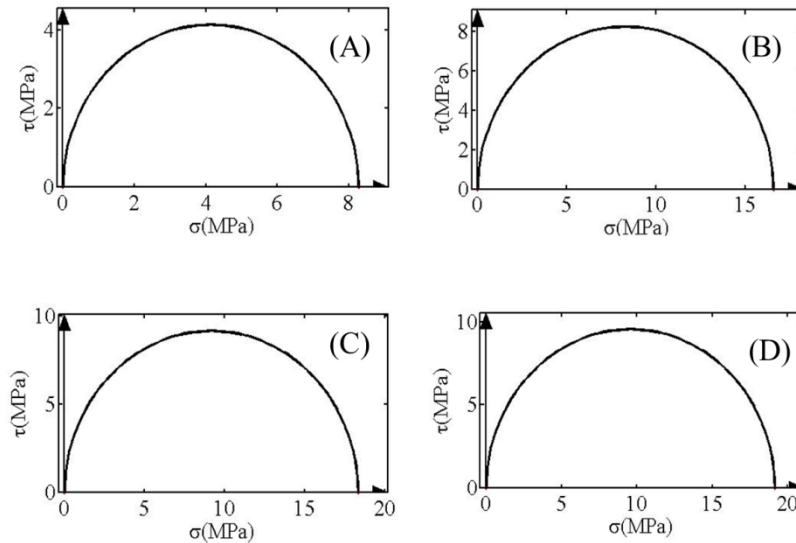


Fig. 4.17. Mohr circles of state of stress for tensile stress on the top of the fold crest for each overburden thickness. (A) Initial overburden 500m; (B) Initial overburden 1000m; (C) Initial overburden 2000m; (D) Initial overburden 3000m.

Fig. 4.18 shows how much overburden rock is eroded when tensile stress is initiated for initial overburden thickness larger than 1000m. For simplicity, it is assumed that the rock is a weak rock and tensile failure is initiated when σ_3' reaches at 0. The results are shown in Table 4.2. The ratio of eroded overburden thickness to the total thickness after buckling gets larger as the initial overburden thickness increases. It suggests that even during the erosional unloading process, tensile stress is more difficult to be initiated for folds with larger overburden thickness. The 500m overburden case is not included in this plot because tensile stress has already been initiated during 30% shortening process (at about 18.6% shortening).

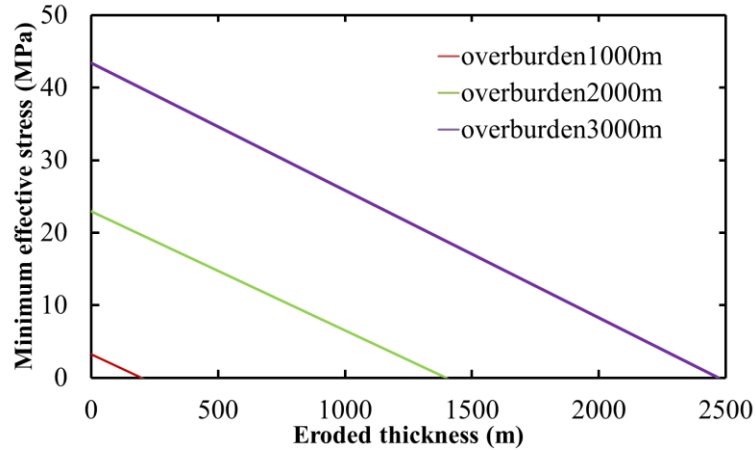


Fig. 4.18. Evolution of σ_3' for larger overburden depth (>1000m) till the tensile stress is initiated during erosion process.

Table 4.2. The eroded overburden thickness and ratio for each initial overburden when tensile stress is initiated at the top of the fold crest

Initial overburden thickness (m)	overburden thickness after buckling(m)	Eroded overburden thickness (m)	Eroded ratio (%)
1000	1367	200	14.6
2000	2785	1400	50.3
3000	4213	2465	58.5

4.5.3. Tensile Stress on the Fold Limb during Erosion. The stress development on the fold limb is independent of the element location (Liu, 2013), the middle element of the limb is investigated to illustrate the magnitude evolution of σ_3' . The contour plots for the spatial distribution of σ_3' are investigated for all elements across the fold limb. Fig. 4.19 presents the development of σ_3' throughout the 30% shortening and erosional unloading process. The observations are summarized as follows:

(1) The minimum effective stress in the limb during the buckling process does not change much for folds featuring a low overburden thickness (<1000m). However, σ_3' of the fold limb increases obviously throughout buckling for folds with large overburden thickness.

(2) There is no failure and therefore no fractures generated on the fold limb during the buckling process.

(3) Tensile stress is reached and tensile failure is likely to be generated during the erosion process.

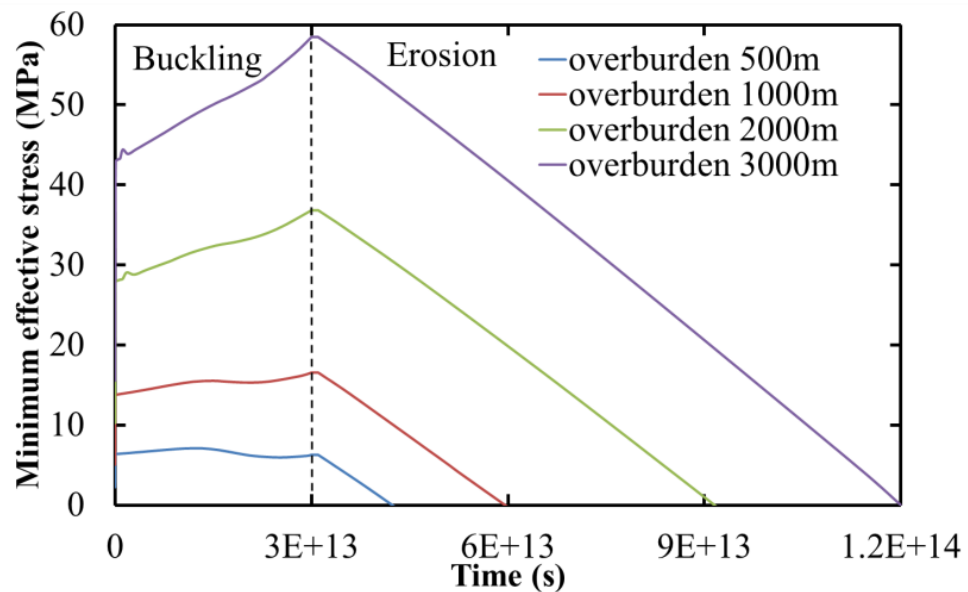


Fig. 4.19. The evolution of the fold limb's minimum effective stress throughout both 30% buckling and the following erosion process.

The time when tensile stresses are obtained on the fold limb can be read from Fig. 4.19. The assumption here is still that the rock is a weak rock and tensile failure is initiated when $\sigma_3' = 0$. Based on the erosion time and the erosion rate, the eroded overburden thickness can be calculated. The results are shown in Table 4.3. The eroded ratio in the table, which is the ratio of the eroded thickness to the overburden thickness

after buckling, increases with the increase of initial overburden. It suggests that it is also more difficult to generate tensile stress on the fold limb for fold with larger overburden thickness. A comparison of Table 4.2 and Table 4.3 shows that the eroded overburden thickness when tensile stress is generated on the fold crest is less than that of the fold limb. Thus, it suggests that it is easier to initiate tensile failure on the fold crest than on the fold limb.

Table 4.3 The eroded overburden thickness and ratio for each initial overburden when tensile failure is initiated on the fold limb

Initial overburden thickness (m)	Overburden thickness after buckling(m)	Eroded overburden thickness (m)	Eroded ratio (%)
500	655	354.5	54.1
1000	1367	906.7	66.3
2000	2785	1871.5	67.2
3000	4213	2867.2	68.1

All cases in this model set generate tensile stress and tensile failure on the fold limb. The Mohr circles illustrating the state of stress for the intersection point of σ_3' and x-axis in Fig. 4.19, which is the time when tensile failure is initiated, are presented in Fig. 4.20. The Mohr circle gets larger as the initial overburden thickness increases. It suggests that the maximum effective stress will get larger as initial overburden thickness increases when the tensile failure is initiated in the fold limb. Comparing Fig. 4.20 and Fig. 4.17, the maximum effective stress at the time when the tensile failure is initiated gets larger as overburden thickness increases. Thus, it also can be concluded that it is easier to initiate tensile failure on the fold crest than on the fold limb.

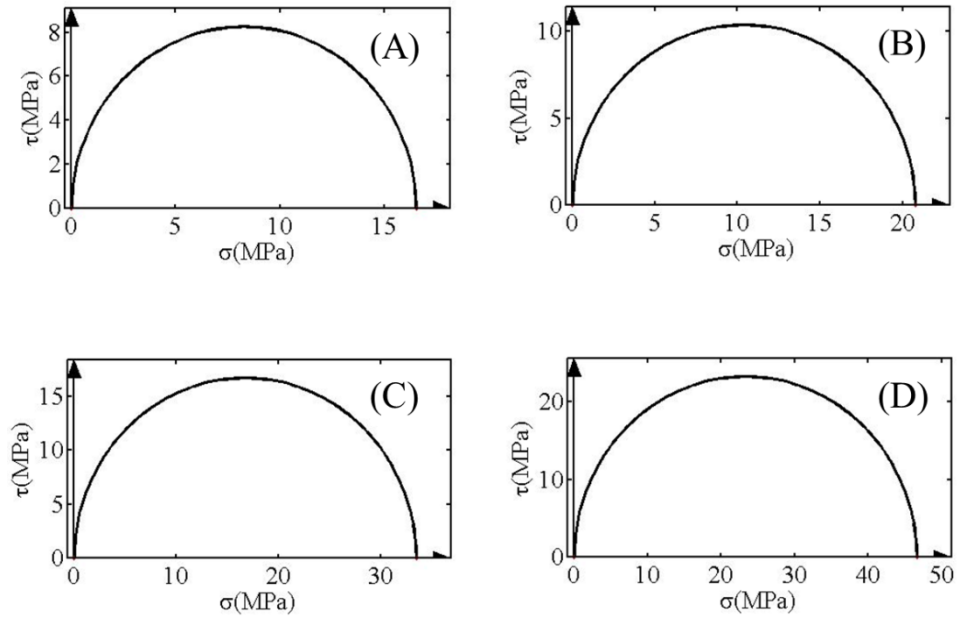


Fig. 4.20. Mohr circles of state of stress for fractures on the middle of fold limb for each overburden thickness. (A) Initial overburden 500m; (B) Initial overburden 1000m; (C) Initial overburden 2000m; (D) Initial overburden 3000m.

The contour plots for the spatial distribution of σ_3' are investigated for all elements across the fold limb (Fig. 4.21). Positive stress magnitude in Fig. 4.21 present the locations where the tensile stress is generated (i.e., it needs to be recalled that ABAQUS™ utilizes the engineering sign convention for stresses, which are tensile stress is negative and compressive stress is positive). The black lines in Fig. 4.21 illustrate the orientations of σ_3' . The extension fractures are generated perpendicular to σ_3' (Griggs and Handin, 1960). Thus, the contour plots in Fig. 4.21 illustrate that tensile fracture switch from vertical in the fold crest to horizontal in the fold limb.

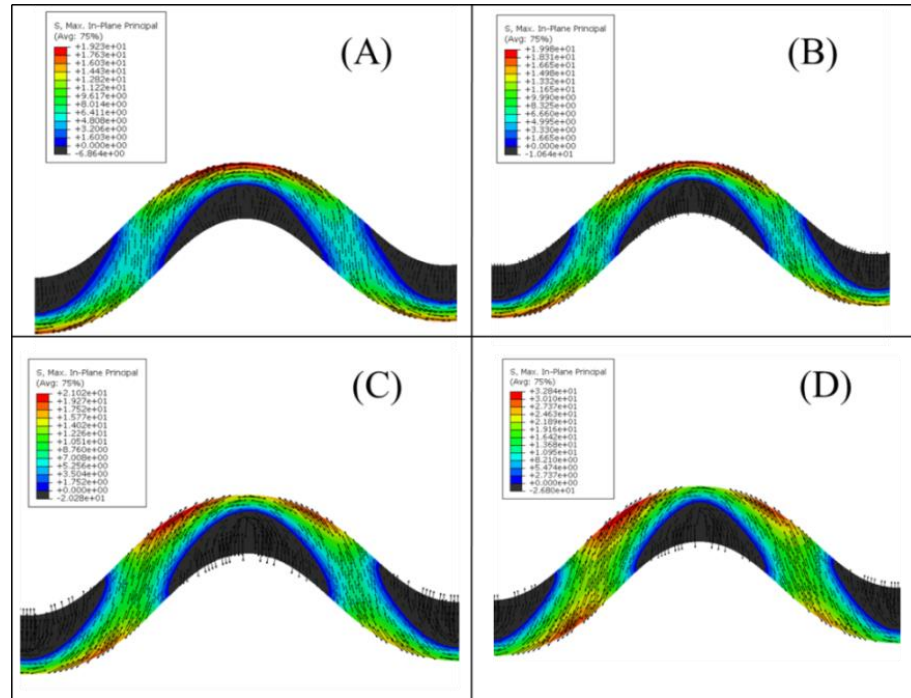


Fig. 4.21. The contour plots for the spatial distribution (the colorful parts) and orientation of σ_3' (the black lines). (A) 500m initial overburden; (B) 1000m initial overburden; (C) 2000m initial overburden; (D) 3000m initial overburden.

4.6. MINIMUM FOLD AMPLITUDE FOR TENSILE STRESS BEING INITIATED

4.6.1. Introduction. Liu (2013) concluded that tensile failure will be generated on the fold crest for high amplitude fold (50% shortening). The erosional unloading process amplified the remnant strain in the fold layer so that the tensile failure can be initiated in the fold limb (Liu, 2013). However, such high amplitude folds are rarely observed on larger scales relevant for hydrocarbon bearing structures. Therefore, the lowest amplitude for buckle fold to initiate tensile failure at the top of the fold crest during erosional unloading process becomes of interest, as such low amplitude folds are much more abundant in hydrocarbon provinces. Shell discovered several such commercial reservoirs, i.e., the Kebabangan field in the South China Sea (Ingram, 2004).

The results presented in section 4.4.2 in this study show that the erosion process only affects the orientation of σ_3' in high amplitude fold with large overburden thickness, i.e., 50% shortening with 3000m overburden thickness. Tensile stress and

tensile failure can be easily generated on the top of fold crest for the basic low amplitude buckle fold models (30% shortening) by erosional unloading process. More numerical models are simulated to find out the minimum fold amplitude and minimum amount of shortening for tensile failure being initiated on the top of fold crest during the erosion process. The minimum amplitude is assumed to be the amplitude when there is no tensile failure generated ($\sigma_3' > 0$) during the buckling process, but it is initiated ($\sigma_3' = 0$) during the erosional unloading process.

4.6.2. Procedure to Obtain the Minimum Amplitude. As shown in Fig. 4.22, the development of the fold amplitude is independent on the overburden thickness but only depends on the amount of shortening. Fig. 4.22 illustrates that the fold amplification period starts at 10% shortening. The minimum magnitude of σ_3' during buckling is reached at about 24% (Fig. 4.23). Based on Fig. 4.1 and Fig. 4.23, the minimum effective stress switches from the vertical stress to the horizontal stress at about 16% shortening for folds with all of these four overburden thicknesses. Thus, this period becomes an indicator to explain tensile fractures parallel to the fold axis which are the fractures of main interest. The minimum amount of shortening for tensile stress being generated during the erosion process is hence between 16% and 24%. However, tensile stress is generated at 18.6% shortening for the 500m overburden thickness model. Thus, for the fold with 500m overburden, the minimum amount of shortening is between 16% and 18.6%. The goal of this section is to obtain the minimum amount of shortening to generate tensile failure for each of the studied overburden thicknesses.

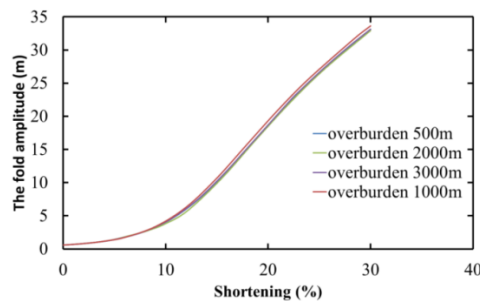


Fig. 4.22. The fold amplitude evolution during buckling process for each overburden thickness.

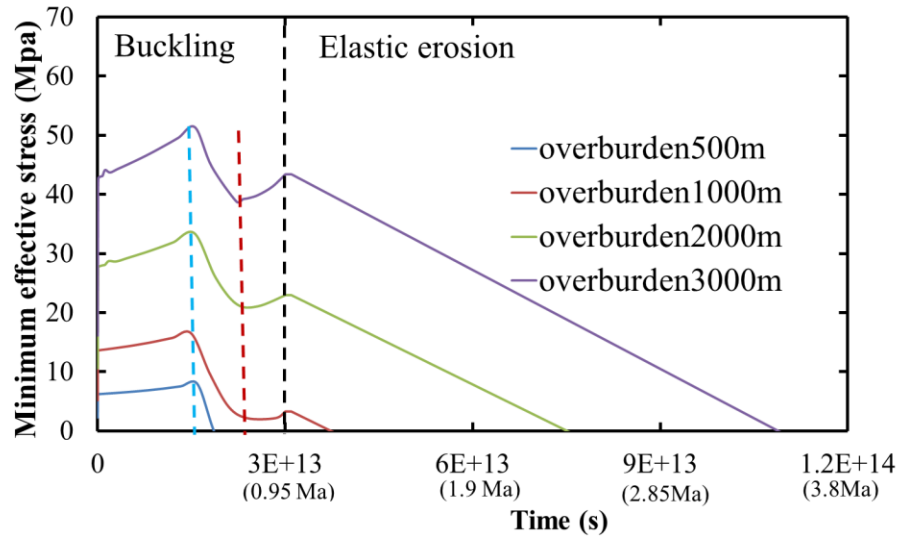


Fig. 4.23. The evolution of minimum effective stress on the fold crest for different overburden thickness. The time before the blue line is the buckling horizontal shortening period. The time between the blue line and black line is the buckling fold amplification period.

The following procedure is followed to find the minimum amplitudes:

Since the range of the minimum amount of shortening for the fold with 500m overburden is the narrowest, i.e. between 16% and 18.6%, the minimum amount of shortening for 500m is determined the first.

As pointed out in chapter 4.6.2, the larger the overburden thickness, the later the tensile stress will be generated. Hence, the minimum amount of shortening to generate tensile stresses for the 500m overburden model is used as the starting point to find the minimum amount of shortening for the 1000m overburden model. The same approach is applied to the 2000m and 3000m overburden models.

The evolutions of σ_3' for each case are presented in Fig. 4.24. The results of the minimum amount of shortening and the resulting fold amplitudes are listed in Table 4.4.

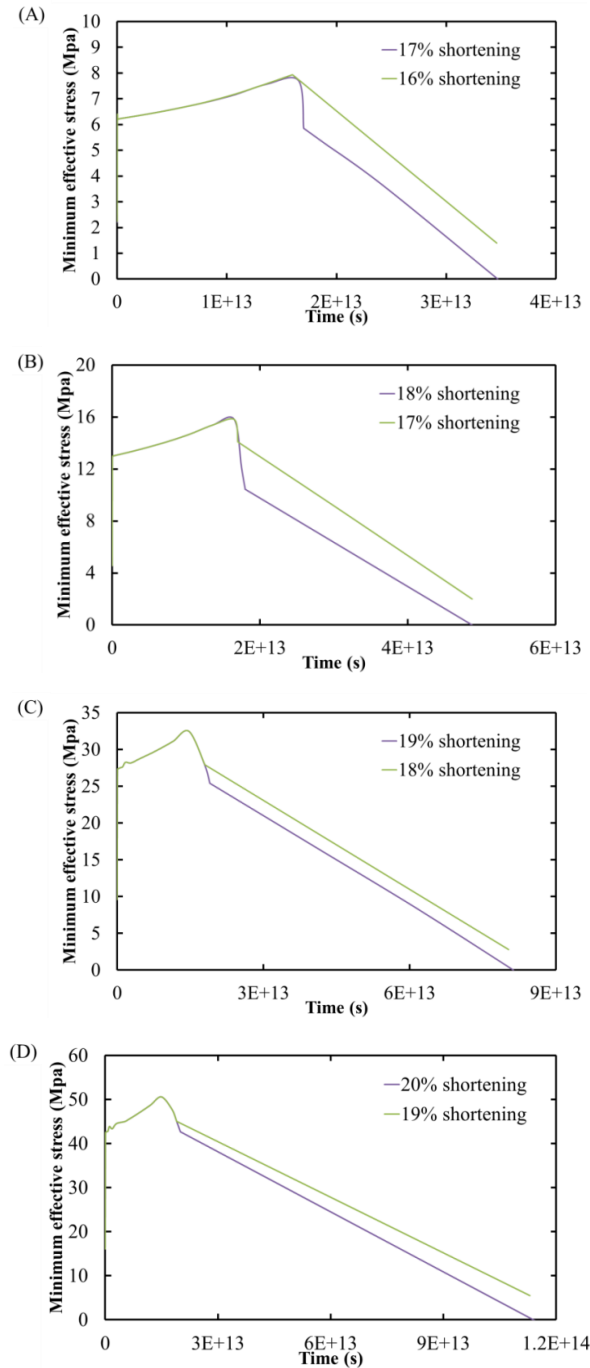


Fig. 4.24. The σ_3' evolution of trial amount of shortening and the target amount of shortening for each overburden thickness model. (A) For 500m overburden model, tensile stress cannot be generated at the end of the erosion process which starts after 16% shortening, but it is initiated during the erosion process which starts after 17% shortening; (B) For 1000m overburden model, tensile stress is initiated during the erosion process which starts after 18% shortening; (C) For 2000m overburden model, tensile stress is initiated during the erosion process which starts after 19% shortening; (D) For 3000m overburden model, tensile stress is initiated during the erosion process which starts after 20% shortening.

Table 4.4. The minimum amount of shortening for tensile stress being initiated

Initial overburden thickness (m)	The minimum amount of shortening (%)	The final fold amplitude (m)	Amplitude/Wavelength ratio (%)
500	17	13.53	3.54
1000	18	15.86	4.15
2000	19	16.72	4.37
3000	20	18.71	4.90

4.6.3. Evolution of σ_3' Orientation. The extension fractures are generated perpendicular to σ_3' (Griggs and Handin, 1960). Thus it is necessary to investigate the orientation of σ_3' at the time when tensile stress is generated. Figs. 4.25 to 4.28 present the orientation of σ_3' at the beginning of the erosion process and at the end of erosion process for each overburden thickness. The effect of erosion on the orientation of σ_3' depends on the overburden thickness and locations. The observations are summarized as follows:

- (1) σ_3' is perpendicular to the fold crest except for the outermost part of the crest where it is horizontal. However, σ_3' is inclined in the fold limb.
- (2) The orientation of σ_3' around the fold crest tends to be inclined towards the fold axis during the erosion process.
- (3) For the folds with smaller overburden thickness (500m and 1000m), the orientation of σ_3' on the fold limb does not change very much throughout the erosion process (Fig. 4.25 and 4.26). However, for the folds with overburden thickness of 2000m and 3000m, the angle between σ_3' and the fold limb gets larger during the erosion process (Figs. 4.27A and 4.28A).

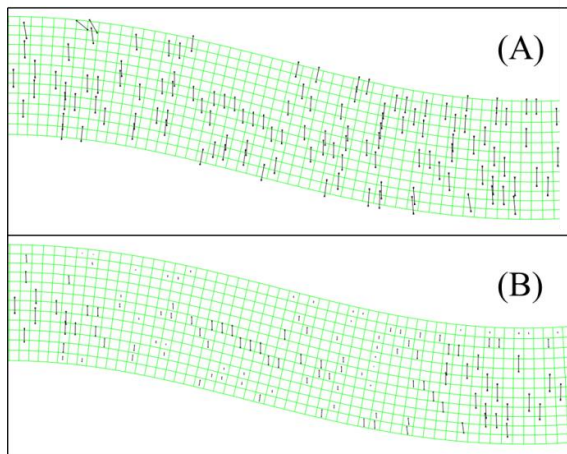


Fig. 4.25. The orientation of σ_3' for 500m initial overburden thickness (the black lines).
 (A) σ_3' orientation at the end of 17% shortening (at the beginning of erosion process);
 (B) σ_3' orientation at the end of erosion process.

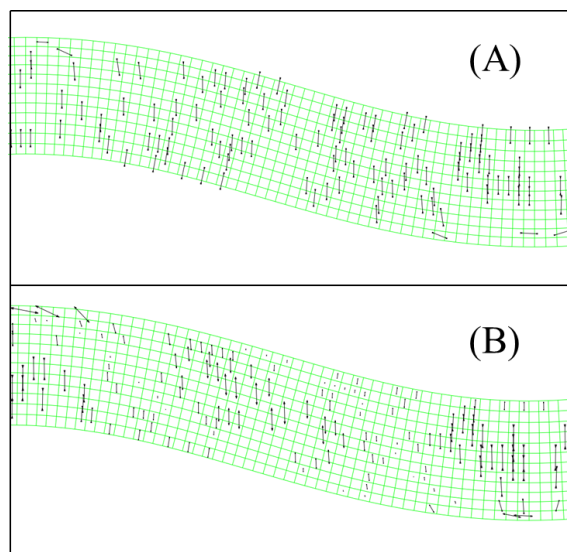


Fig. 4.26. The orientation of σ_3' for 1000m initial overburden thickness (the black lines).
 (A) σ_3' orientation at the end of 18% shortening (at the beginning of erosion process);
 (B) σ_3' orientation at the end of erosion process.

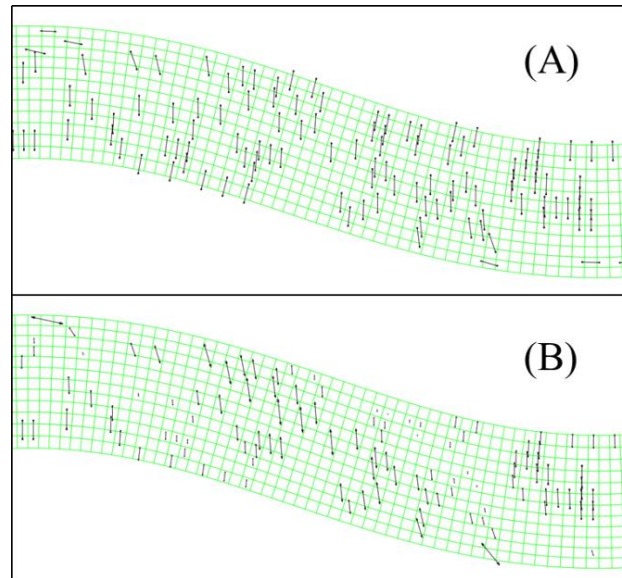


Fig. 4.27. The orientation of σ_3' for 2000m initial overburden thickness (the black lines).
 (A) σ_3' orientation at the end of 19% shortening (at the beginning of erosion process);
 (B) σ_3' orientation at the end of erosion process.

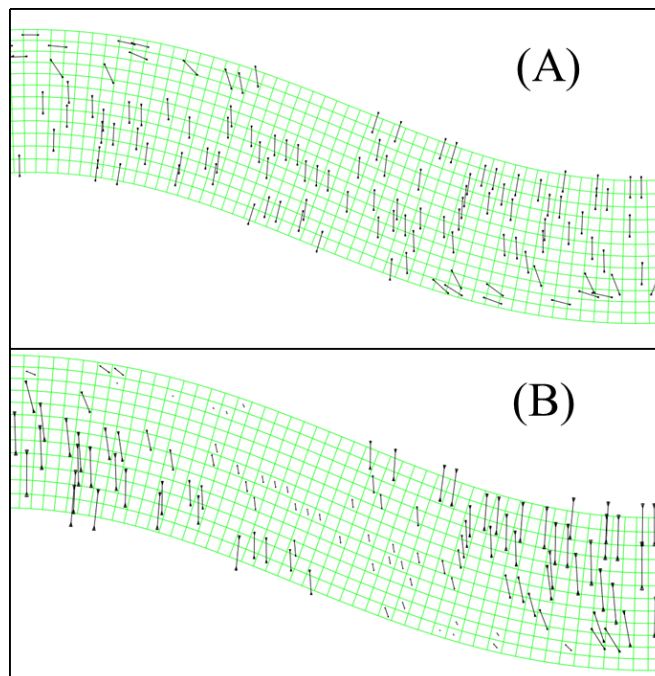


Fig. 4.28. The orientation of σ_3' for 3000m initial overburden thickness (the black lines).
 (A) σ_3' orientation at the end of 20% shortening (at the beginning of erosion process);
 (B) σ_3' orientation at the end of erosion process.

4.6.4. Evolution of Stress Magnitude and Tensile Failure Initiation. The minimum amplitude for likely initiation of tensile failure on the top of fold crest is found when tensile stress is generated at the end of erosion. Fig. 4.29 shows these minimum amplitudes for each overburden thickness. The minimum amplitude increases with depth because the increase of overburden pressure will make it more difficult to obtain tensile stress. Fig. 4.30 presents the final fold amplitude compared with the wavelength.

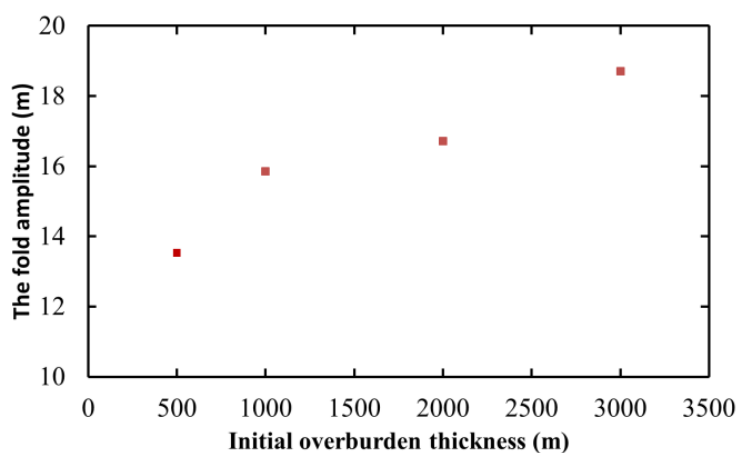


Fig. 4.29. The minimum amplitude for tensile failure being initiated at the end of erosion process for each overburden thickness in this research.

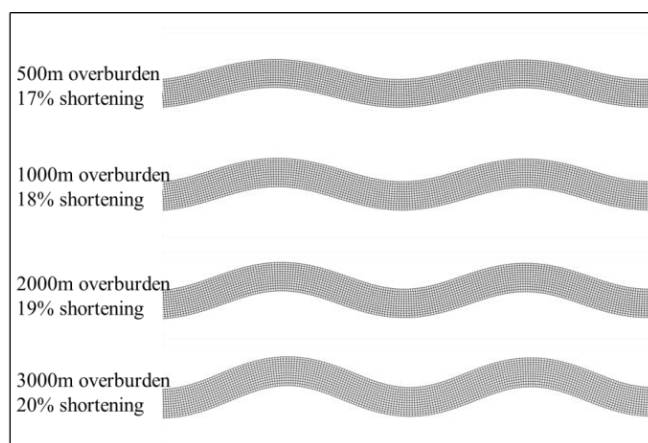


Fig. 4.30. The final fold amplitude and wavelength for each overburden thickness models.

The evolution of σ_3' for both buckling and erosion process for the fold crest is presented in Fig. 4.31. Tensile stress and tensile failure are initiated at the end of the erosional unloading process (Fig. 4.31A). Comparing to the 30% shortening models (Fig. 4.31B), tensile stress and tensile failure are initiated much later in these minimum amplitude folds.

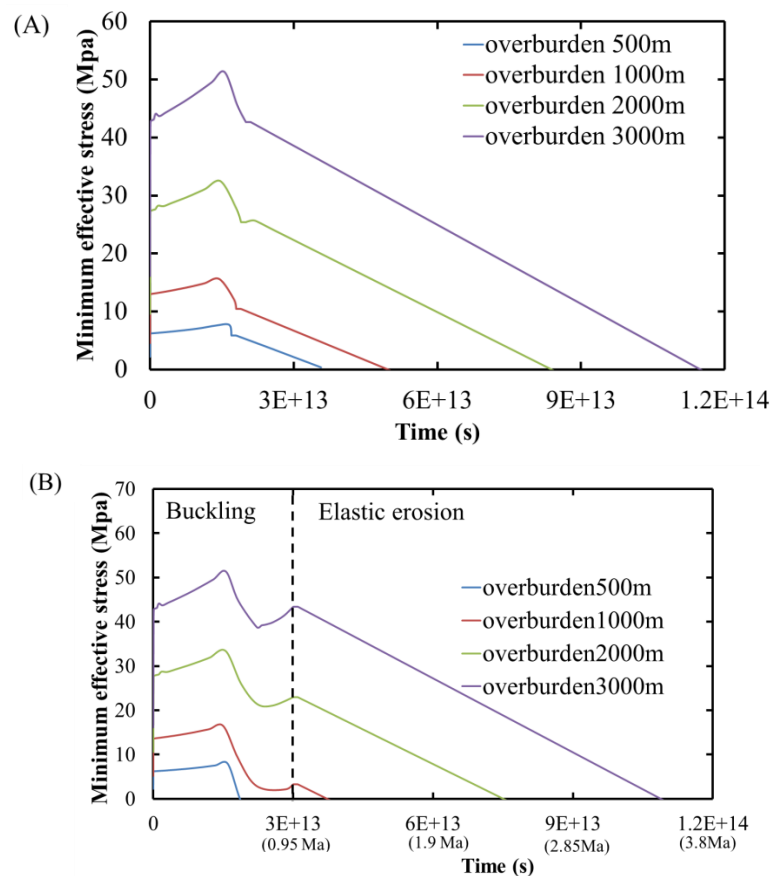


Fig. 4.31. Evolution of the σ_3' in the fold crest throughout the entire buckling and erosional unloading process. (A) σ_3' evolution for the minimum amount of shortening for each overburden thickness; (B) σ_3' evolution for 30% shortening

The stress evolution and tensile failure on the fold limb are also investigated in these minimum amplitude models. Fig. 4.32 presents the evolution of σ_3' and σ_1' in the

fold limb. The development of both effective stresses during the buckling process is different to that at the fold crest. However, this study is focused on the erosion process. The discussion of stress evolution during the buckling process is ignored here. Fig. 4.32(A) shows that tensile stress and tensile failure are also generated at the end of the erosion process. σ_1' magnitudes shown in Fig. 4.32(B) are large, thus the differential stress will be relatively large compared to σ_3' such that it is likely that shear failure may be generated on the fold limb earlier than tensile failure. This will be discussed in the following discussion chapter later.

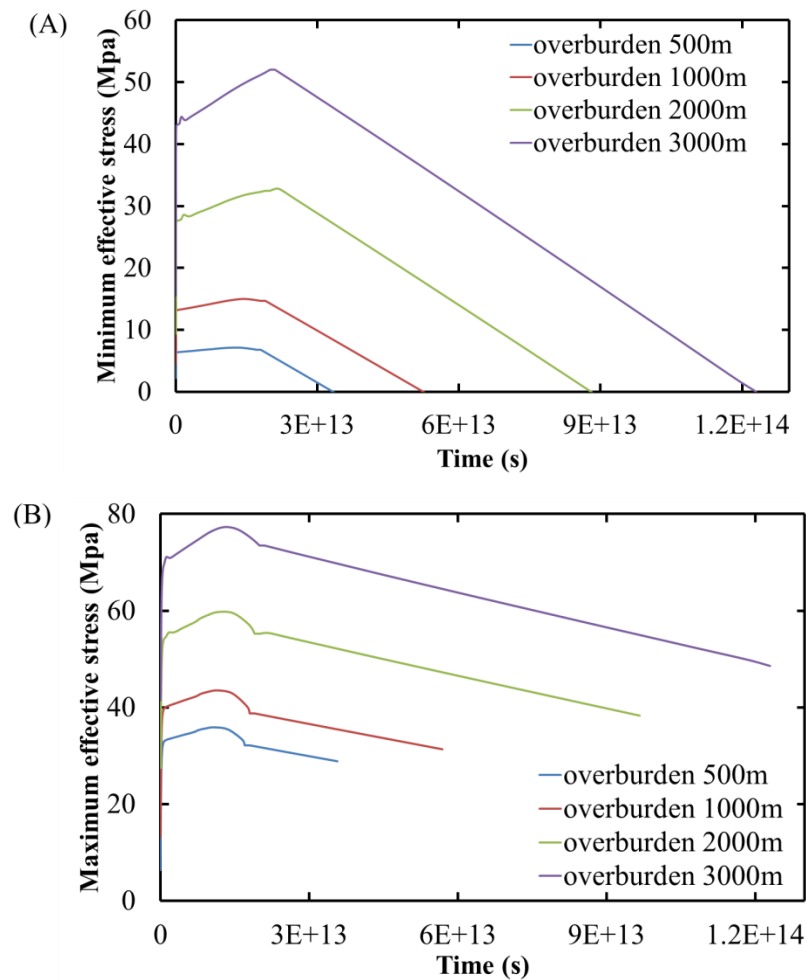


Fig. 4.32. The fold limb's stress evolution throughout the whole buckling and erosion process. (A) The evolution of σ_3' ; (B) The evolution of σ_1' .

5. DISCUSSION

This study utilizes 2D plain strain Finite Element Analysis (FEA) to investigate the influence of the erosional unloading step on the evolution of the state of stress in buckle folds and the associated tensile failure. The erosional unloading process amplifies the remnant strain in the fold layer (Liu, 2012) and its influence on the initiation of tensile and shear fractures is discussed here.

5.1. RHEOLOGY

The simulations in this study include two steps: the buckling process and the erosional unloading process. The rheological behavior of the rocks during buckling is crucial to the selection of the dominant wavelength (i.g., Biot, 1961; Ramberg, 1961; Currie et al., 1962). In this study, the rock during buckling has visco-elastic rheology. During the erosional unloading process, the rheological behavior influences the state of stress in the folded layer. As shown in chapter 4.2, both visco-elastic erosion and elastic erosion were simulated. At the beginning of the visco-elastic erosional unloading process, σ_3' shows a 15MPa increase immediately to equilibrate with σ_1' (Figs. 4.8 and 4.9). This is due to the uni-axial strain boundary condition during the erosional unloading process. This equilibration process results in zero differential stress which is not characteristic for crustal rock. Thus, only elastic erosion rheology is considered for the analyses of the erosion/exhumation process.

5.2. OVERBURDEN INFLUENCE

Lemiszki et al. (1994) conclude that as overburden thickness increases, it gets harder to generate tensile failure during buckling. For larger overburden thickness models, a larger fluid pressure is required to initiate fractures. The minimum ratio of the pore pressure to the vertical pressure, $\lambda=0.73$, is required for a fold with 3000m overburden (Lemiszki et al., 1994). Liu (2013) points out that the minimum permeability to generate tensile fractures on the fold limb is 10^{-19} m^2 for a fold with 1000m overburden. The results in this study are coincident with these published results. Fig. 4.16 presents that tensile stress can only be generated for 500m overburden models with 30%

shortening under normal pore pressure conditions. This is because the buckling induced tensional stress is overcome by the compressional vertical stress (Lemiszki et al., 1994).

During the erosional unloading process, the overburden thickness will influence the timing when tensile fractures will be initiated (Table 4.2 and 4.3). The ratio of eroded overburden thickness to the total thickness after buckling gets larger as the initial overburden thickness increases for both the fold crest and the fold limb. This can be explained by the elastic erosion process under uni-axial strain condition. σ_3' is σ_h' and is larger at the end of 30% shortening with larger overburden thickness. Based on equation (5) which shows the relationship between the eroded overburden thickness and σ_3' during the elastic erosional unloading process, the eroded thickness required for the larger overburden thickness model is larger than that of the lower overburden thickness model.

The orientations of σ_3 and subsequent likely locations of tensile fractures are independent of the overburden thickness (Fig. 4.21). For low amplitude folds, the tensile fractures initiated during the elastic erosional unloading process are perpendicular to the bedding in the outer portion of the fold crest, while it rotates to be parallel to the bedding in the fold limb (Table 5.1 and 5.2).

5.3. TENSILE FAILURE INITIATION FOR LOW AMPLITUDE FOLDS

Liu (2013) concludes that tensile failure is likely to be generated on the fold crest for high amplitude fold (50% shortening) during the buckling process. Tensile stress is not generated for low amplitude folds (30% shortening) with large overburden thickness and high permeability during the buckling process (Fig. 4.16). However, as stated by Liu (2013), the erosional unloading process amplifies the remnant strain in the fold layer. This study shows that tensile stress can be initiated in both the fold crest and the fold limb for low amplitude folds (30% shortening and less) during the elastic erosional unloading process (Fig. 4. 16). The minimum amount of shortening and the lowest fold amplitude to generate tensile stress during the erosional unloading process are investigated. The results are shown in Table 4.4. The lowest fold amplitude increases as the overburden thickness increases. This is due to the fact that larger buckling induced tensional strain is required for the fold with a larger overburden thickness to overcome the compressional vertical strain.

The orientation and magnitude of the principal effective stresses varies with the element location in the buckle folds. Thus, depending on the rock strength, shear failure may be initiated prior to tensile failure in buckle folds. Mohr circles are plotted for the fold crest and the fold limb, respectively, for both strong rocks and the weak rocks. To simplify the analysis and reduce the need to make assumptions regarding the rocks' tensile strength, likely tensile failure will be evaluated at $T_0=0\text{MPa}$, and two magnitudes for the shear strength (i.e., cohesion) are selected in this study to simulate strong rock ($S_0=12\text{ MPa}$) and weak rock ($S_0=6\text{ MPa}$) based on the experimental data (Bieniawski, 1984; Pollard and Fletcher, 2005; Fossen, 2010). Within the fold limb, tensile failure is more likely to occur for strong rocks, whereas shear failure is more likely to occur for weaker rocks (Table 5.1 and 5.2). Tables 5.1 and 5.2 present the state of stress using Mohr circles, spatial extent of tensile stresses, likely fracture orientation and locations, and their relation to commonly observed fractures for strong rocks and weak rocks respectively, for the various buckle folds investigated. The contour plots in Table 5.1 and 5.2 present the orientation of σ_3' and likely fractures in the fold after the erosional unloading process. The grey areas indicate tensile stress; black regions in contour plots indicate compressional stress. The short red lines represent the orientation of σ_3' . The yellow lines indicate the orientations of the likely shear fractures, and the blue lines are the orientations of the likely tensile fractures. The observations are summarized as followed for strong rocks (Table 5.1):

(1) The tensile stress magnitude ranges from 0MPa to -12MPa in the fold at the time when erosional unloading process is terminated. σ_3' is vertical in the fold limb but it is horizontal in the fold crest for low amplitude folds (i.e., 18% and 20% shortening). However, for high amplitude folds (i.e., 50% shortening), σ_3' is sub-vertical in both the fold limb and the fold crest.

(2) Tensile fracture can be initiated at the fold crest for strong rocks with 18% and 20% shortening (Table 5.1). Differential stress is low and tensile failure is very likely under this condition. Tensile fractures are oriented parallel to the fold axis and normal to bedding. This fracture pattern is confirmed by multiple studies (i.e., Ramsay, 1964; Reif et al., 2011, Price & Cosgrove, 1990). Tensile failure can be initiated in the fold limb for very strong rock as well (Table 5.1). Fractures

in the fold limb are oriented sub-parallel to the bedding. This state of stress, rather than generating these sub-parallel fractures, would more likely reactivate tensile failure parallel to bedding, i.e., result in beef structures (Cobbold, 2013). Shear failure can be initiated prior to the initiation of tensile stress in the fold limb for weaker rocks (Table 5.1). This fracture pattern is also confirmed by many studies (i.e., Groshong, 1975; Price & Cosgrove, 1990; Lemiszki et al., 1994).

(3) Tensile fractures can be initiated at the fold crest for strong rock with 30% and 40% shortening (Table 5.1). Fractures are parallel to the fold axis and normal to bedding. Tensile fractures at the fold crest are either generated by the erosional unloading process or they may represent reactivated tensile joint sets. Moreover, tensile failure can be initiated in the fold limb for strong rock as well. Fractures are parallel to the bedding (Table 5.1). However, the tensile fracture in the fold limb may evolve into shear failure at certain erosional unloading stage when the shear stress appropriate for a thrust fault causes a significant amplification of the fractures. These fractures are commonly observed (i.e., Ramsay, 1964; Groshong, 1975; Reif et al., 2011, Price & Cosgrove, 1990).

(4) Tensile stress can be initiated in the outer hinge area of the fold with 50% shortening. Differential stress is low and tensile failure is very likely under this condition. Tensile fractures are oriented sub-parallel to the fold axis. Tensile failure can be initiated in the fold limb as well. The orientation of tensile fractures is perpendicular to the bedding. The extent of tensile stress magnitude promotes these tensile fractures across the entire limb. These fractures are commonly observed in folds (Price and Cosgrove, 1990). However, the tensile fracture in the fold limb may evolve into shear failure at certain erosional unloading stage when the shear stress appropriate for a thrust fault causes a significant amplification of the fractures. These features are commonly observed (i.e., Ramsay, 1964; Groshong, 1975; Reif et al., 2011, Price & Cosgrove, 1990).

Table 5.1. Fractures for Strong rocks

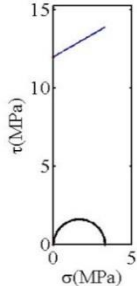
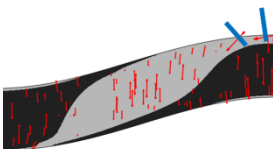
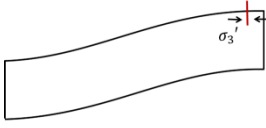
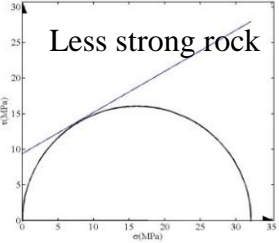
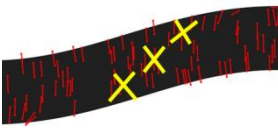
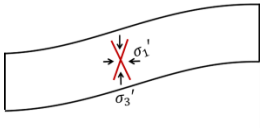
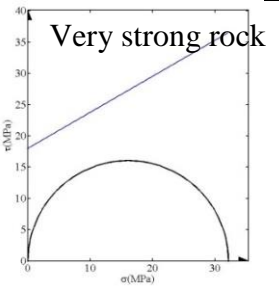
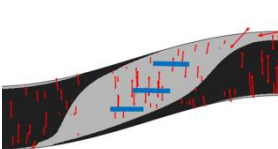
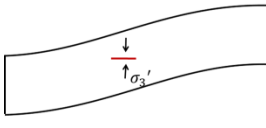
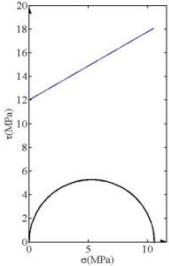
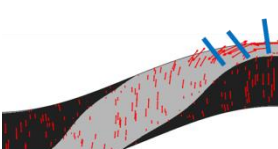
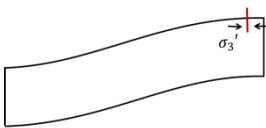
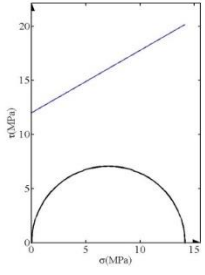
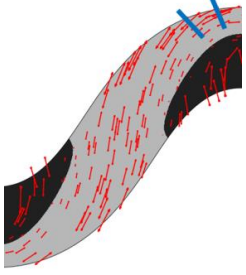
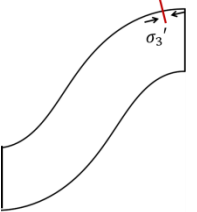
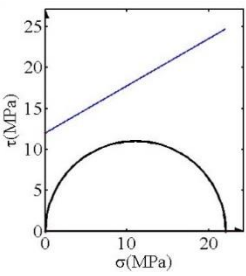
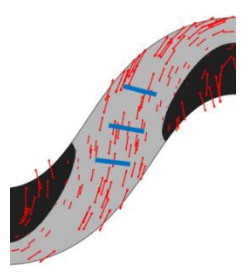
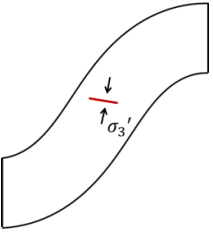
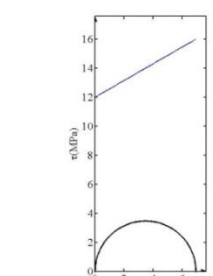
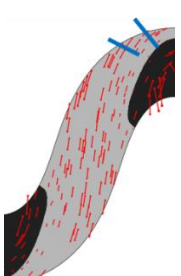
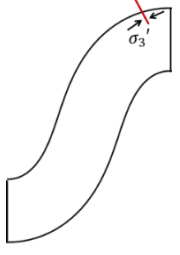
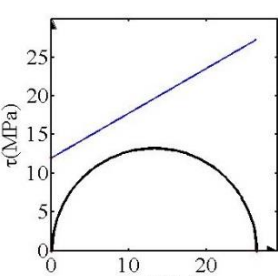
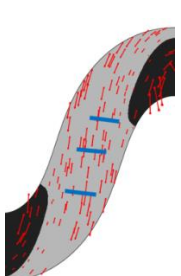
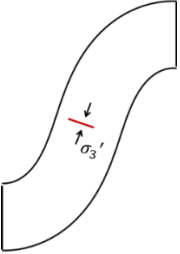
ϵ (%)	Fold part	Mohr circles	σ_3' orientation & likely fractures in this study (shear fractures in yellow; tensile fractures in blue)	Commonly observed fractures
	Fold crest			 Price & Cosgrove, 1990
18	Fold limb	 Less strong rock		 Price & Cosgrove, 1990
	Fold limb	 Very strong rock		 Groshong, 1975
20	Fold crest			 Price & Cosgrove, 1990

Table 5.1. Fractures for Strong rocks (cont.)

ϵ (%)	Fold part	Mohr circles	σ_3' orientation & likely fractures in this study (shear fractures in yellow; tensile fractures in blue)	Commonly observed fractures
20	Fold limb	<p>Less strong rock</p>		<p>Price & Cosgrove, 1990</p>
	Fold limb	<p>Very strong rock</p>		<p>Groshong, 1975</p>
30	Fold crest			<p>Price & Cosgrove, 1990</p>
	Fold limb			<p>Price & Cosgrove, 1990</p>

Table 5.1. Fractures for Strong rocks (cont.)

ϵ (%)	Fold part	Mohr circles	σ_3' orientation & likely fractures in this study (shear fractures in yellow; tensile fractures in blue)	Commonly observed fractures
40	Fold crest			 Price & Cosgrove, 1990
	Fold limb			 Price & Cosgrove, 1990
50	Fold crest			 Price & Cosgrove, 1990
	Fold limb			 Price & Cosgrove, 1990

The observations are summarized as followed for weak rocks (Table 5.2):

- (1) Tensile fracture can be initiated at the fold crest for weak rocks with 18% and 20% shortening (Table 5.2). Differential stress is low and tensile failure is very likely under this condition. Tensile fractures are oriented parallel to the fold axis and normal to bedding. This fracture pattern is confirmed by multiple studies (i.e., Ramsay, 1964; Reif et al., 2011, Price and Cosgrove, 1990). Shear failure can be initiated prior to the initiation of tensile stress in the fold limb for weak rocks (Table 5.2). This feature is also commonly observed (i.e., Groshong, 1975; Price & Cosgrove, 1990; Lemiszki et al., 1994).
- (2) The state of stress at the fold crest after erosional unloading of folds subjected to 30% or 40% shortening indicates that both tensile fractures or normal faults can be initiated in the fold crest with 30% and 40% shortening (Table 5.2). Tensile stress can be initiated at the fold crest before shear failure being initiated. As the erosional unloading process goes on, the tensile fracture may evolve into a normal fault.
- (3) Shear fractures can be initiated throughout the entire fold limb for weak rock with 30%, 40%, and 50% shortening (Table 5.2). These findings are in agreement with many studies (i.e., Ramsay, 1964; Reif et al., 2011, Price & Cosgrove, 1990).
- (4) Tensile stress can be initiated in the outer hinge area of the fold with 50% shortening. Differential stress is low and tensile failure is very likely under this condition. Tensile fractures are oriented sub-parallel to the fold axis.

Table 5.2. Fractures for weak rocks

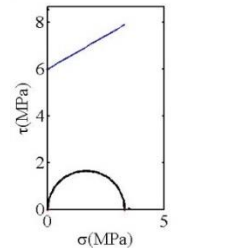
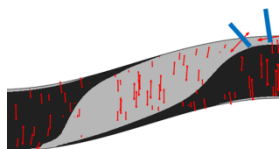
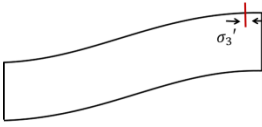
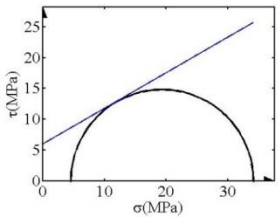
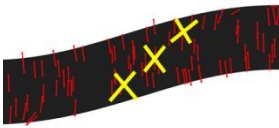
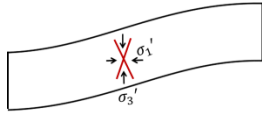
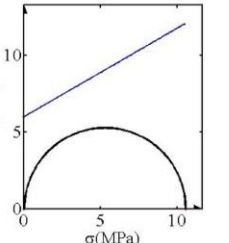
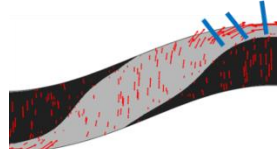
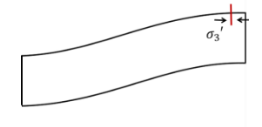
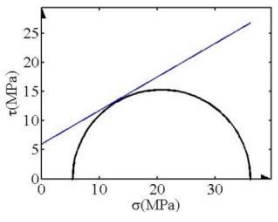

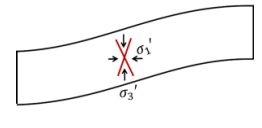
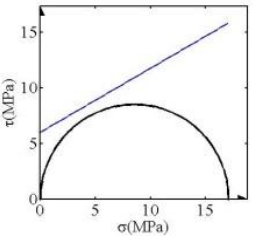
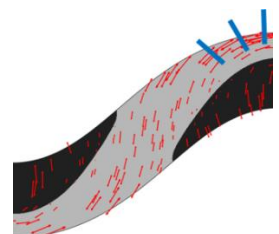

ϵ (%)	Fold part	Mohr circles	σ_3' orientation & likely fractures in this study (shear fractures in yellow; tensile fractures in blue)	Commonly observed fractures	
18	Fold crest				Price & Cosgrove, 1990
	Fold limb				Price & Cosgrove, 1990
20	Fold crest				Price & Cosgrove, 1990
	Fold limb				Price & Cosgrove, 1990
30	Fold crest				Price & Cosgrove, 1990

Table 5.2. Fractures for weak rocks (cont.)

ϵ (%)	Fold part	Mohr circles	σ_3' orientation & likely fractures in this study (shear fractures in yellow; tensile fractures in blue)	Commonly observed fractures	
30	Fold limb				Price & Cosgrove, 1990
40	Fold crest				Price & Cosgrove, 1990
	Fold limb				Price & Cosgrove, 1990
50	Fold crest				Price & Cosgrove, 1990
	Fold limb				Price & Cosgrove, 1990

5.4. VISCOSITY CONSIDERATION

Liu (2013) illustrated that the viscosity is a crucial parameter to fold shape and state of stress during the buckling process. In the sensitivity analysis of viscosity, the constant competence contrast is 50. The amount of shortening applied is 20% before the erosional unloading process beginning. The overburden thickness is 3000m. The remaining material parameters are assigned as listed in Table 3.1. It shows that an unrealistic state of stress will result from high viscosity folds by the buckling process (Fig. 5.1). The tensile stress on the crest of the highest viscosity fold (10^{22} Pa·s) develops so fast that it reaches 110 MPa at the end of 20% shortening, which is unrealistic in nature. Similarly, the tensile stress on the crest of fold with viscosity of 5×10^{21} Pa·s will reach 10 MPa at the end of buckling, and it will continue to decrease to reach unrealistic tensile stress during erosion process. As the folding layer's viscosity increases, the layer parallel stress will increase which will lead to the increase of $\lambda_{dv}/\lambda_{de}$ (Eq. 29). Thus, the rock behavior will tend to be more elastic. Thus, high viscosity folds are beyond the objective of this study, only folds with viscosity of 10^{21} Pa·s is investigated in this study.

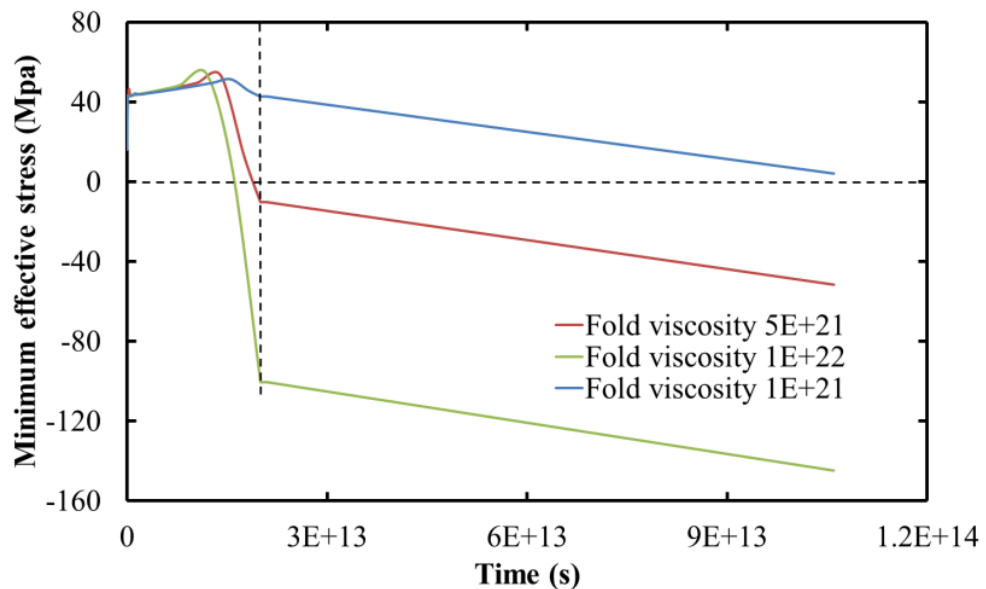


Fig. 5.1. The evolution of the fold crest's σ_3' throughout the entire process including both buckling process and the erosional unloading process.

5.5. LIMITATIONS

The elastic erosional unloading models employed in this study have some limitations:

- (1) No thermal stress is considered in the erosional unloading process. Twiss and Moores (2007) point out that the geothermal and temperature will change during the erosion process. However, it will take a very long time for thermal stress to be initiated in the erosional unloading process.
- (2) An appropriate tensile failure criterion and plastic strain are not considered in this study. Due to this neglect the tensile stress will continue to increase even though the rocks should fail when the tensile strength is reached. However, the erosional unloading process is terminated manually when tensile stress is generated on the fold crest top. This allows us to investigate the location, time, and orientation of the initiation of tensile stress.
- (3) Permeability is not considered in these simulations. Lemiszki et al. (1994) concluded that a larger fluid pressure is required to initiate fracture during buckling for larger overburden thickness models. Liu (2013) points out that overpressure can be generated in low permeability model during the buckling due to the layer parallel shortening. However, the behavior of ABAQUSTM with low permeability model during the erosional unloading remains to be clarified. Hence, only tensile stress in rocks with normal pore pressure are investigated in this study.

6. SUMMARY

6.1. CONCLUSION

This study utilizes 2D plain strain Finite Element Analysis (FEA) to investigate the influence of the elastic erosional unloading process, which is a post-folding process, on the evolution of the state of stress in low amplitude visco-elastic single-layer buckle folds and the associated failures. Sensitivity analyses are performed with different input parameters (e.g., shortening ratio, overburden pressure, and viscosity).

The conclusions summarized from this study are listed as followed:

- Both the horizontal stress and vertical stress decrease during erosional unloading process due to the decrease of the overburden pressure. The reduction rate of vertical stress is independent of shortening. However, the larger the amount of shortening the higher the reduction rate of the horizontal stress will be, because the horizontal stress and strain are resulted from the buckling process. For low amplitude folds, the erosional unloading process has no effect on σ_3' orientation.
- Changes in the state of stress within single layer buckle folds during elastic erosional unloading are independent of the overburden thickness. The stress decreases in the same rate for each overburden thickness model with the same amount of shortening. However, its influence on the buckling process can still result in initiation of tensile stress at different times during the erosional unloading process. The larger the overburden thickness, the later tensile stress will be initiated. Also, the model with larger overburden thickness will generate a larger differential stress at the time when tensile stress is initiated.
- Tensile stress and tensile failure can be easily generated on the top of the fold crest for the basic low amplitude buckle fold models (30% shortening) during the erosional unloading process. The minimum amplitude for tensile stress being initiated on the top of the fold crest gets larger as the overburden thickness increases.
- The minimum amount of shortening and the minimum fold amplitude for each overburden thickness are listed in Table 6.1.

Table 6.1. The minimum amount of shortening and minimum fold amplitude

Initial overburden thickness (m)	The minimum amount of shortening (%)	The final fold amplitude (m)
500	17	13.53
1000	18	15.86
2000	19	16.72
3000	20	18.71

- Fracture patterns (i.e., type, location, and orientation) depend on the rock strength, the location in the fold, and the amount of shortening. Tensile failure is more likely to occur for strong rocks, whereas shear failure is more likely to occur for weaker rocks. For stronger rocks, shear failure will be initiated in the fold limb for lower amplitude folds. In weak rocks, tensile failure can be initiated in the hinge zone, and the tensile fractures can evolve into normal faults.

6.2 OUTLOOK

The influence of rock permeability could be included in future studies. Overpressure will be generated in low permeability rock during buckling process, and the overpressure can affect the initiation of fractures during both the buckling process and the erosion/exhumation process.

This study is based on 2D numerical simulation which is a simplification of the natural cases. To some extent, 2D simulation can provide reasonable explanations and approximations to the rock mechanics problem. However, 3D models are needed in some cases to describe more accurate boundary conditions and material properties variations and realistic fold geometries.

To simulate the state of stress evolution during erosion/exhumation, thermal stress can be taken into account in the future study. The geothermal and temperature will

change in the erosion process, which will also affect the pore pressure evolution. Thus, including the thermal stress in erosion/exhumation is important.

APPENDIX A.

STRESS EVOLUTION AT THE FOLD CREST DURING 30% SHORTENING

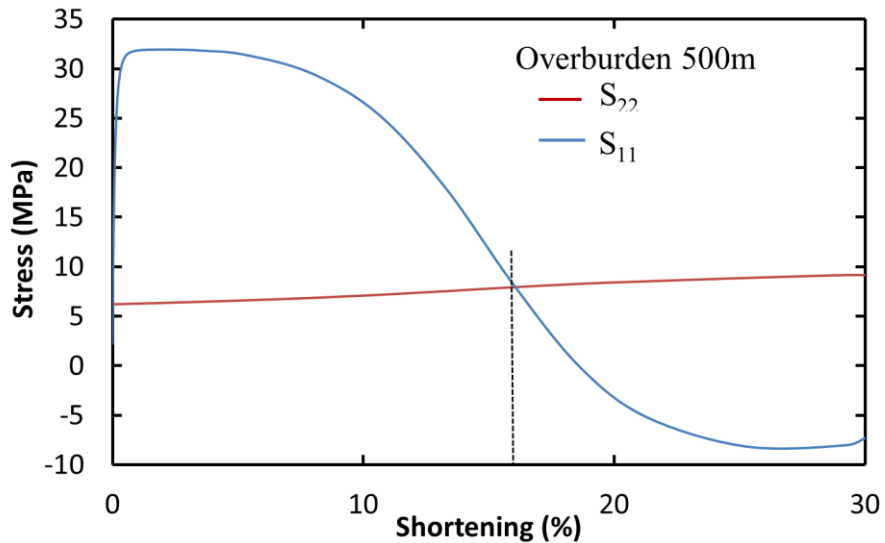


Fig. A.1. Stress evolution at the top of the fold crest with 500m overburden thickness throughout 30% shortening process

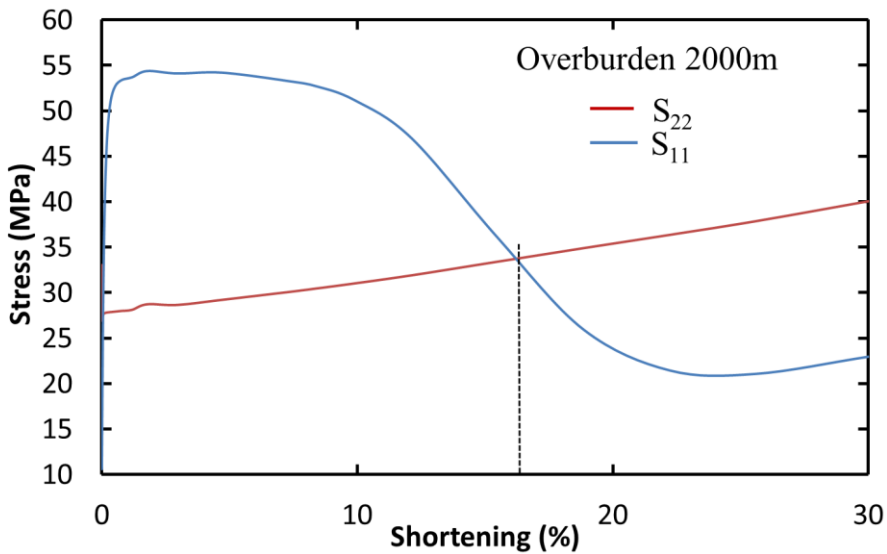


Fig. A.2. Stress evolution at the top of the fold crest with 2000m overburden thickness throughout 30% shortening process

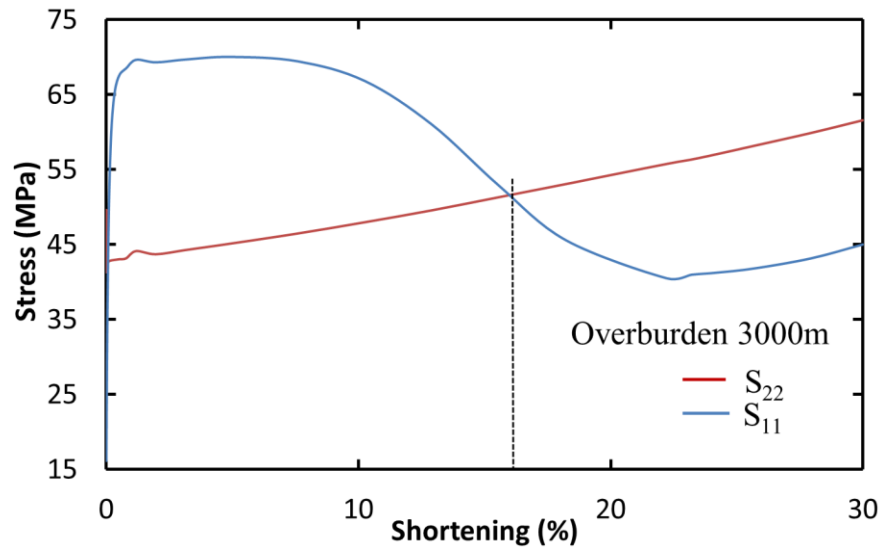


Fig. A.3. Stress evolution at the top of the fold crest with 3000m overburden thickness throughout 30% shortening process

APPENDIX B.

STRESS EVOLUTION ON THE FOLD LIMB DURING 30% SHORTENING

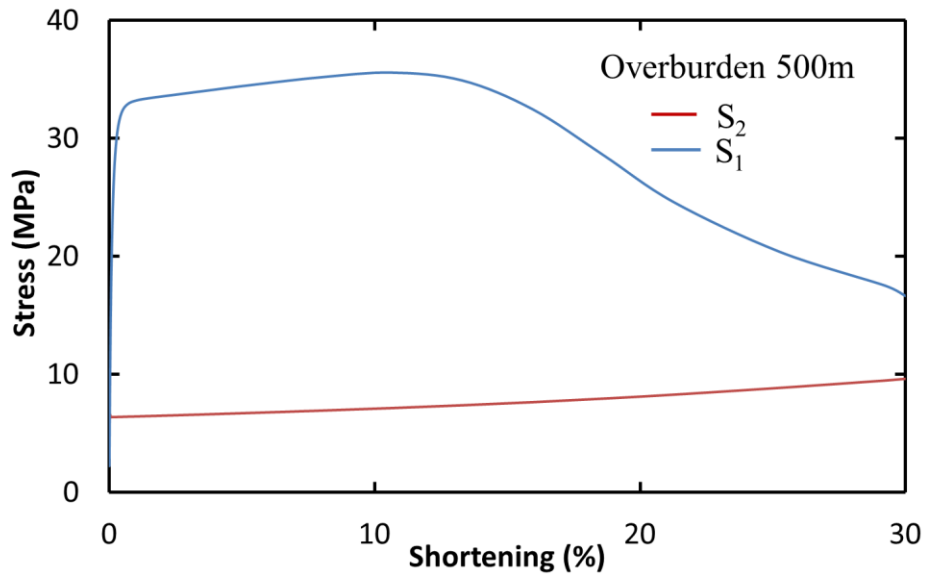


Fig. B.1. Stress evolution on fold limb with 500m overburden thickness throughout 30% shortening process

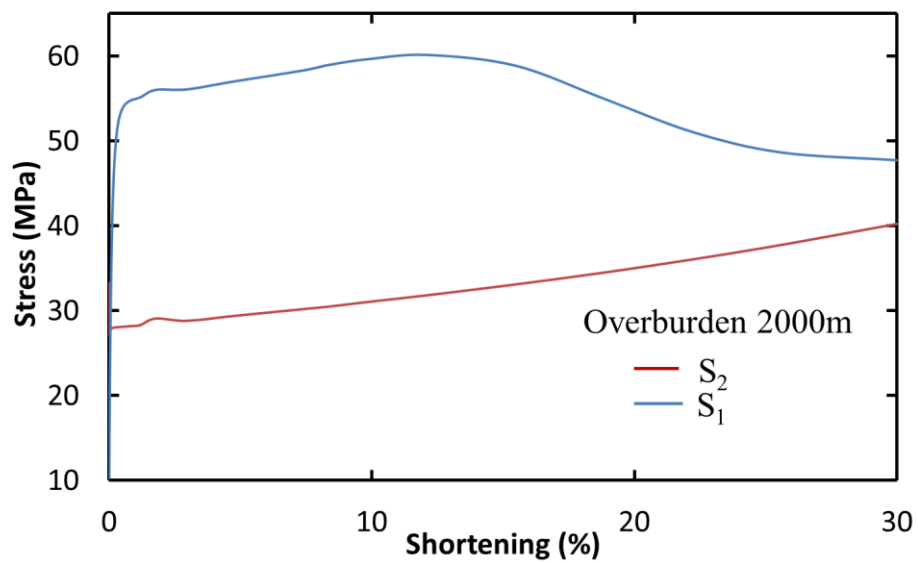


Fig. B.2. Stress evolution on fold limb with 2000m overburden thickness throughout 30% shortening process

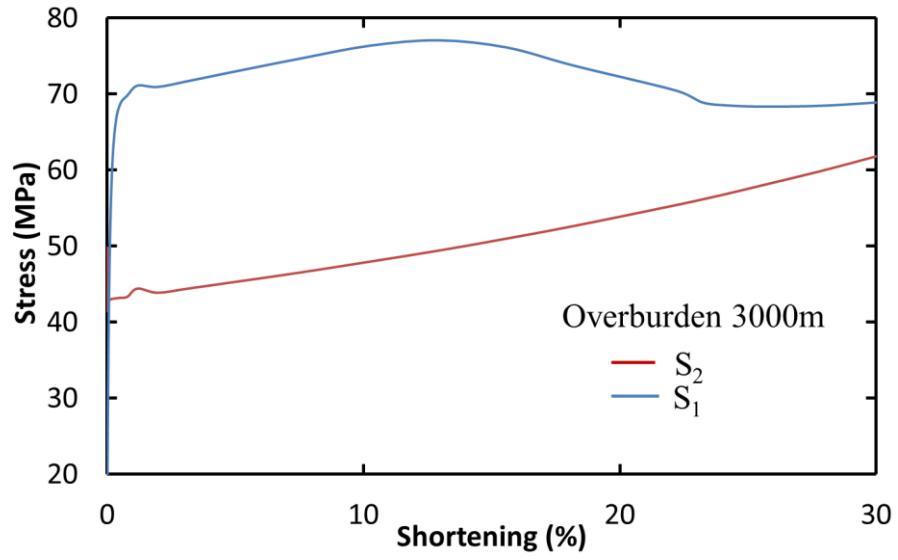


Fig. B.3. Stress evolution on fold limb with 3000m overburden thickness throughout 30% shortening process

BIBLIOGRAPHY

- Abbassi, M. R. and N. S. Mancktelow, (1990), The effect of initial perturbation shape and symmetry on fold development. *J. Struct. Geol.*, 12,273-282.
- Abbassi, M. R. and N. S. Mancktelow, (1992), Single layer buckle folding in non-linear materials-I. Experimental study of fold development from an isolated initial perturbation. *J. Struct. Geol.*, 14,85-104.
- Biot, M.A. (1959), On the instability of folding deformation of a layered viscoelastic medium in compression. *J. Appl. Mech.*, 26, 393-400.
- Biot, M. A. (1961), Theory of folding of stratified viscoelastic media and its implications in tectonics and orogenesis, *Geol. Soc. Am. Bull.*, 72, 1595-1620.
- Biot, M. A., H. Ode, and W. L. Roever, (1961), Experimental verification of the theory of folding of stratified viscoelastic media, *Geol. Soc. Am. Bull.*, 72, 1621-1632.
- Biot, M.A., 1965. *Mechanics of Incremental Deformations*. John Wiley and Sons, New York.
- Cloos, H., 1948, Gang und Gehwerk einer Falte: *Zeitschrift der Deutschen Geologischen Gesellschaft*, v. 100, p. 290–303.
- Cobbold, P.R., 1975. Fold propagation in single embedded layers. *Tectonophysics* 27, 333e351.
- Cobbold, P.R., 1977. The finite element analyses of fold propagation e problematic application. *Tectonophysics* 38, 339e353.
- Cobbold, P.R., A. Zanella, N. Rodrigues, and H. Loseth, 2013, Bedding-parallel fibrous veins (beef and cone-in-cone): Worldwide occurrence and possible significance in terms of fluid overpressure, hydrocarbon generation and mineralization, *Marine and Petroleum Geology* 43, 1-20.
- Currie, J.B., Patnode, H.W., Trump, R.P., 1962. Development of folds in sedimentary strata. *Geological Society of America Bulletin* 73, 655e674.
- Dieterich, J. H., and N. L. Carter, (1969), Stress-history of folding, *Am. J. Sci*, 267(2), 129-154.

- Dunne, W.M., 1986, Mesosstructural development in detached folds; an example from West Virginia: *Journal of Geology*, v. 94, p. 473–488.
- Fischer, M. P., and M. S. Wilkerson, (2000), Predicting the orientation of joints from fold shape: Results of pseudo–three-dimensional modeling and curvature analysis. *Geology*, 28(1), 15-18, doi: 10.1130/0091 7613(2000)028<0015:PTOOJF>2.3.CO; 2
- Fletcher, R.C. (1977), Folding of a single viscous layer: exact infinitesimal amplitude solution. *Tectonophysics*, 39, 593-606.
- Griggs, D.T., and Handin, J., 1960, Observations on fracture and an hypothesis of earthquakes, *Rock deformation: Boulder, Colorado, Geological Society of America Memoir 79*, p. 347–364.
- Groshong, R.H., (1975), Strain, fractures, and pressure solution in natural single-layer folds. *Geol. Soc. Am. Bull.*,v.86, p. 1363-1376.
- Hall, J., (1815), On the vertical position and convolutions of certain strata and their relation with granite. *Transactions Royal Society Edinburgh* 7, 79-108.
- Hancock, P.L., 1985, Brittle microtectonics; principles and practice: *Journal of Structural Geology*, v. 7, p. 437–457.
- Hubbert M K, and W. Rubey, (1959), Role of fluid pressure in mechanics of overthrust faulting I. Mechanics of fluid-filled porous solids and its application to overthrust faulting. *Geol. Soc. Am. Bull.*, 70(2): 115-166.
- Jaeger, J.C., and Cook, N.G., 1979, *Fundamentals of rock mechanics*: London, Chapman and Hall, 593 p.
- Jaeger, J. C., N. G. Cook, and R. W. Zimmerman (2007), *Fundamentals of Rock Mechanics*. Blackwell Publishing Ltd, Oxford, UK.
- Jeng, F.S., K.P. Huang, (2008), Buckling folds of a single layer embedded in matrix – Theoretical solution and characteristics. *Journal of Structural Geology* 30, 633-648.
- Keunen, P.H., and L. U. de Sitter, (1938), Experimental investigation into the mechanisms of folding. *Leidshe Geol. Mag.*, 10, 217-40.
- Lemiszki, P. J., J. D. Landes, AND R. D. Hatcher, (1994), Controls on hinge-parallel extension fracturing in single-layer tangential-longitudinal strain folds, *Journal of Geophysical Research: Solid Earth* (1978–2012), 99(B11), 22027-22041, doi: 10.1029/94JB01853.

- Lisle, R. J. (1994), Detection of zones of abnormal strains in structures using Gaussian curvature analysis, AAPG bulletin, 78(12).
- Liu, X., (2013), Tensile failure during structural development of single-layer buckle folds,
- Mancktelow, N.S. (1999), Finite-element modeling of single-layer folding in elasto-viscous materials: the effect of initial perturbation geometry, J. Struct. Geol., 21, 161-177, doi: 10.1016/S0191-8141(98)00102-3.
- Medina, C.R., J.A. Rupp, and D.A. Barnes. (2011), Effects of reduction in porosity and permeability with depth on storage capacity and injectivity in deep saline aquifers: A case study from the Mount Simon Sandstone aquifer, International Journal of Greenhouse Gas Control, 5,146-156, doi: 10.1016/j.ijggc.2010.03.001.
- Molnar P., R. S. Anderson, and S. P. Anderson, (2007), Tectonics, fracturing of rock, and erosion, Journal of geophysical research, v. 112, F03014, doi: 10.1029/2005JF000433.
- Mühlhaus, H. B. (1993), Evolution of elastic folds in plane strain, Modern Approaches to Plasticity .Elsevier, Amsterdam, 737-765.
- Price, N.J., and Cosgrove, J.W., 1990, Analysis of geological structures: Cambridge, Cambridge University Press, 502 p.
- Price, Neville J. (1966), Fault and joint development in brittle and semi-brittle rock, Vol. 1. Pergamon Press, Oxford, UK.
- Ramberg, H., 1959. Evolution of ptygmatic folding. Norsk Geologisk Tidsskrift 39, 99e155.
- Ramberg, H., 1961. Contact strain and folding instability of a multilayered body under compression. Geologische Rundschau 51, 405e439.
- Ramberg, H., 1963. Fluid dynamics of viscous buckling applicable to folding of layered rocks. Bulletin of the American Association of Petroleum Geologists 47, 484e505.
- Ramberg, H.(1960), Relationship between length of arc and thickness of ptygmatically folded veins, Am. J. Sci., 258, 36-46.
- Ramberg, H. (1964), Selective buckling of composite layers with contrasted rheological properties, a theory for simultaneous formation of several orders of folds, Tectonophysics, 1, 307-341.

- Ramm, M., 1992. Porosity–depth trends in reservoir sandstones: theoretical models related to Jurassic sandstones offshore Norway. *Marine Petrol. Geol.* 9, 553–567.
- Ramsay, J. G. (1967), *Folding and Fracturing of Rocks*. McGraw-Hill, New York.
- Reber, J. E., S. M. Schmalholz, and J. P. Burg, (2010), Stress orientation and fracturing during three-dimensional buckling: Numerical simulation and application to chocolate-tablet structures in folded turbidites, SW Portugal. *Tectonophysics*, 493(1), 187-195, doi: 10.1016/j.tecto.2010.07.016.
- Reif, D., K. Decker, B. Grasemann, and H. Peresson, (2011), Fracture patterns in the Zagros fold-and-thrust belt, Kurdistan Region of Iraq. *Tectonophysics* 576-577, 46-62.
- Reches, Z., 1976, Analysis of joints in two monoclines in Israel: *Geological Society of America Bulletin*, v. 87, p. 1654–1662.
- Schmalholz, S.M., Podladchikov, Y., 1999. Buckling versus folding: importance of viscoelasticity. *Geophysical Research Letters* 26, 2641e2644.
- Schmalholz, S.M., Podladchikov, Y.Y., 2000. Finite amplitude folding: transition from exponential to layer length controlled growth. *Earth and Planetary Science Letters* 181, 619e633.
- Sherwin, J.-A., Chapple, W.M., 1968. Wavelengths of single layer folds: a comparison between theory and observation. *American Journal of Science* 266, 167e179.
- Sibson, R. H., (2003), Brittle-failure controls on maximum sustainable overpressure in different tectonic regimes, *AAPG Bull.* , v.87, NO. 6, PP. 901-908.
- Stearns, D.W., 1968, Certain aspects of fractures in naturally deformed rocks, in Riecker, R.E., ed., *Rock mechanics seminar: Bedford, Terrestrial Sciences Laboratory*, p. 97–118.
- Stearns, D. W., and M. Friedman (1972), Reservoirs in fractured rock, *AAPG Memoir* 16, 82–100.
- Terzaghi, K. (1936), The shearing resistance of saturated soils and the angle between planes of shear, in *Proc. Int. Conf. Soil Mech. Found. Eng.*, Vol.1, Harvard University Press, Cambridge, MA, pp. 54–6.
- Turcotte, D. L., and G. Schubert, (2002), *Geodynamics*. Cambridge University Press, New York.

- Twiss, R.J. and E.M. Moores, (2007), *Structural Geology*, 2nd Edition, W.H. Freeman and Company, New York.
- Twiss, R.J., and Moores, E.M., 1992, *Structural geology*: New York, Freeman, 532 p.
- Williams, J. R., R. W. Lewis, and O. C. Zienkiewicz, (1978), A finite element analysis of the role of initial perturbations in the folding of a single viscous layer. *Tectonophysics* ,45, 187-200.
- Watts N L. (1987), Theoretical aspects of cap-rock and fault seals for single-and two-phase hydrocarbon columns. *Mar. Petrol Geol.*, 4(4): 274-307.
- Wang, H. F., (2000), *Theory of linear poroelasticity*, Princeton University Press, New Jersey.
- Zhang, Y., N.S. Hobbs, B.E. Ord, and H.B. Muhlhaus, (1996), Computer simulation of single-layer buckling, *J. Struct. Geol.*, 18, 645-655, doi: 10.1016/S0191-8141(96)80030-7.

VITA

Mengke Li was born in August 23, 1989 in China. She graduated from high school in 2008. She received her Bachelor's degree in Resources Exploration Engineer from China University of Petroleum (Eastern China) in 2012. In August 2012, she started her graduate study in Petroleum Engineering at Missouri University of Science and Technology. During her Master's study, she worked with Dr. Andreas Eckert as a graduate assistant. She earned her Master's degree in Petroleum Engineering from Missouri University of Science and Technology in December of 2014.

